Beam-Beam Interaction Studies at LHC

Master Thesis

Michaela Schaumann

RWTH Aachen University
Supervisor: Prof. Dr. Achim Stahl

CERN
European Organization for Nuclear Research
Supervisor: Dr. Reyes Alemany Fernandez

Abstract

The beam-beam force is one of the most important limiting factors in the performance of a collider, mainly in the delivered luminosity. Therefore, it is essential to measure the effects in LHC. Moreover, adequate understanding of LHC beam-beam interaction is of crucial importance in the design phases of the LHC luminosity upgrade. Due to the complexity of this topic the work presented in this thesis concentrates on the beam-beam tune shift and orbit effects.

The study of the Linear Coherent Beam-Beam Parameter at the LHC has been determined with head-on collisions with small number of bunches at injection energy (450 GeV). For high bunch intensities the beam-beam force is strong enough to expect orbit effects if the two beams do not collide head-on but with a crossing angle or with a given offset. As a consequence the closed orbit changes. The closed orbit of an unperturbed machine with respect to a machine where the beam-beam force becomes more and more important has been studied and the results are as well presented.

September 2011

CERN-THESIS-2011-138
26/09/2011

Contents

1 Theoretical Motivation **5**
- 1.1 Luminosity and the Geometry of a Particle Collider . . . 6
- 1.2 Fields and Forces . . . 8
  - 1.2.1 Beam-Beam Force . . . 8
  - 1.2.2 Linear Beam-Beam Tune Shift . . . 11
- 1.3 Resulting Effects . . . 15
  - 1.3.1 Incoherent Effects . . . 15
  - 1.3.2 Coherent Effects . . . 15
- 1.4 Long-Range Interactions . . . 16

2 The Large Hadron Collider **21**
- 2.1 Physics Motivation . . . 21
- 2.2 The Machine . . . 22
  - 2.2.1 Injection System . . . 22
  - 2.2.2 Magnets . . . 24
  - 2.2.3 Closed Orbit Correctors . . . 28
  - 2.2.4 Cryogenics and Superconductivity . . . 28
  - 2.2.5 Radio Frequency Cavities . . . 30
  - 2.2.6 Collimator System . . . 30
  - 2.2.7 Beam Dump . . . 30
- 2.3 Measurement Devices for Beam Dynamics . . . 31
  - 2.3.1 Fast Beam Current Transformer (FBCT) . . . 31
  - 2.3.2 Beam Position Monitor (BPM) . . . 33
  - 2.3.3 Wire Scanner . . . 35
  - 2.3.4 Beam Synchrotron Radiation Telescope (BSRT) . . . 37
  - 2.3.5 Schottky Pick-Up . . . 40
  - 2.3.6 Machine Luminosity Monitors (BRAN) . . . 44

3 Linear Coherent Beam-Beam Parameter **45**
- 3.1 Nominal and Current Operational Situation . . . 46
- 3.2 Experimental Conditions . . . 47
- 3.3 Analysis of MD Data from 30/06/2011 . . . 48
  - 3.3.1 Observations . . . 49
  - 3.3.2 Absolute Value of the Emittance . . . 51
  - 3.3.3 Linear Coherent Beam-Beam Parameter . . . 53
  - 3.3.4 Tune Shift from Tune Measurements . . . 56

3.3.5 Conclusion for Fill 1911 58
3.4 Analysis of Further Data 59
3.5 Conclusion 60

4 Orbit Effects **63**
4.1 Long-Range Beam-Beam Kick 64
4.2 Orbit Effects due to Bunch-by-Bunch Differences 71
4.2.1 Simulations 71
4.2.2 Beam Position Monitors 75
4.2.3 ATLAS Luminous Region Reconstruction 76
4.2.4 Luminosity Optimization 80

5 Conclusion **83**

6 Acknowledgement **85**

1 Theoretical Motivation

The performance of a particle collider is quantified by the energy available for the production of new physics events and by the luminosity. The required large center of mass energy can only be provided with colliding beams where little or no energy is lost in the motion of the center of mass system, like it would be the case for beam-on-target experiments. Therefore two counter rotating beams are injected into a circular accelerator or storage ring and are brought into collisions once accelerated to the maximum energy. The beams are now interacting with each other in two different ways:

1. High energy collisions between two particles.
2. Distortion of the beam by electromagnetic forces.

The first interaction is the aim of building a particle collider and therefore highly wanted. The outcome of these high energy collisions will be measured in the detectors.

On the other hand, the particles in the beam will be distorted by crossing the opposite beam, since one beam is a collection of charged particles and thus represents an electromagnetic potential for the other beam. Hence, a charged beam will exert forces on itself (space charge) and on the other beam (beam-beam effects). Unfortunately these two effects go together and cannot be separated. Typically 0.001% (or less) of the particles collide and 99.999% are distorted [1].

These interactions can be very strong and occur whenever the two beams share a common beam pipe. This can either be directly at the interaction points (IP), where the beams are brought into collisions on purpose, or in the interaction region (IR) to both sides of the IP, where the two beams are already sharing the same beam pipe in order to prepare for the collisions in the IP. All interactions happening not directly at the IP are parasitic encounters and undesirable.

The beam-beam force is one of the most important and limiting factors in the performance of a particle collider. Many beam parameters are affected, resulting in a wide spectrum of effects for the beam dynamics like, tune shift with the risk of crossing resonances, dynamic aperture reduction due to distortion of the phase space, orbit effects, etc.

From a theoretical point of view, the easiest way to study the beam-beam effects is to look at the changes the forces of one beam exert to the behaviour of a single test particle crossing this beam. The beam will act on that test particle like a strong non-linear electromagnetic lens. The test particle will be affected by the beam, but the effect the single particle has on the opposite beam can be neglected. Nevertheless, in a real particle collider a beam is rather colliding with an ensemble of particles than with a single one, therefore collective effects have to be taken into account. Now the one beam will disturb every single particle in the other beam as mentioned before, but due to the different positions the particles have with respect to the center of the beam they are crossing, they see a different particle distribution and therefore each particle is affected by a different force. On the other hand, these effects must be applied vice versa to the other beam. It acts as an electromagnetic lens to the first beam, as well as it exerts forces to the opposite beam in the same way but depending on its own particle distribution [2].

Moreover, as a result of the interaction the distribution in both beams can change, so that the force becomes time dependent. A self-consistent treatment is necessary in simulations of the beam-beam force, i.e. since the forces change dynamically, they have to be recalculated after each crossing.

To study beam-beam effects the force needs to be known. To predict a model, concepts of non-linear dynamics and multiple-particle dynamics must be applied. Analytical models and simulation techniques were well developed in the last 10 years and their predicting power is improving, but the LHC represents a new and unknown regime for what concerns beam-beam interactions. Present models do not have the predictive power needed for such an accelerator layout. Even if a general, qualitative understanding of beam-beam interactions is available, a quantitative and detailed study for the case of multiple bunch beams and multiple beam-beam interactions does not exist so far [3].

Also different beam parameters for both beams (which can also change dynamically due to the interaction) can have very detrimental effects on the beam. This results in a wide spectrum of effects for the beam dynamics. Due to the complexity of this topic not all effects can be discussed in detail in the scope of this thesis, the analysis here will concentrate on a few particular effects.

As said before, the beam-beam force is one of the most important limiting factors in the performance of a particle collider. They become especially important for high density beams, i.e. high intensity and/or small beam sizes to achieve high luminosities. Therefore, it is essential to measure the effects at LHC. Moreover, adequate understanding of LHC beam-beam interaction is of crucial importance in the design phases of the LHC luminosity upgrade.

1.1 Luminosity and the Geometry of a Particle Collider

Besides the beam energy the number of useful interactions (events) is as well a very important parameter, especially when rare events with a small production cross section are studied. The quantity that measures the ability of a particle accelerator to produce the required number of interactions is called luminosity and represents the proportionality factor between the number of produced events per unit of time, dR/dt, and the production cross-section of the considered reaction, σ_p:

$$\frac{dR}{dt} = L \times \sigma_p \tag{1.1}$$

The luminosity is calculated from the beam parameters and is given in units of $cm^{-2}s^{-1}$. In the specific case of a circular collider and when the particle density distribution can be approximated to a Gaussian, the luminosity of two beams colliding exactly head-on is given by:

$$L = \frac{N_1 N_2 f N_b}{2\pi \sqrt{\sigma_{x1}^2 + \sigma_{x2}^2}\sqrt{\sigma_{y1}^2 + \sigma_{y2}^2}} \tag{1.2}$$

where N_1 and N_2 are the two colliding bunch intensities, f is the revolution frequency of the bunches in the ring, N_b the number of bunches per beam, and σ_{x_i} and σ_{y_i} are the transversal beam-sizes in the horizontal and vertical direction, respectively. In the approximation of equal distributions for both beams $\sigma_{x1} = \sigma_{x2}$ and $\sigma_{y1} = \sigma_{y2}$, Equation 1.2 simplifies to

$$L = \frac{N_1 N_2 f N_b}{4\pi \sigma_x \sigma_y} \tag{1.3}$$

If the interaction is not exactly head-on the luminosity is reduced by a factor S, the so-called luminosity reduction factor. It represents the geometrical overlap of the two particle distributions, which can be equal to one, when the two distributions are perfectly overlapping, or smaller than one in case of collisions with a crossing angle, offsets, hourglass effect, non-Gaussian beam profile and/or non-zero dispersion at the collision point [4].

Since the luminosity is proportional to the number of bunches N_b, it is desirable to operate a collider with as many bunches as possible to get the highest luminosity. In a single ring collider such as LEP, the operation with k bunches leads to $2 \cdot k$ collision points. When k is a large number, most of them are unwanted and must be avoided to reduce the perturbation due to the beam-beam effects. On the other hand, the LHC uses two separated beam-pipes, since two equally charged proton beams counter rotate around the ring. Therefore, the two beams need to be brought together into a common vacuum chamber to make them collide at the interaction points. Figure 1.1 shows schematically the beams crossing in the horizontal plane at the IP with a given crossing angle achieved by an arrangement of separation and recombination magnets around the interaction region [2].

The beams travel in a shared beam-pipe for more than 120 m to adjust the bunches for the crossing and to separate them again into their own pipes afterwards. Under nominal conditions the distance between the bunches is only 25 ns, therefore they will meet in the whole region and not only in the foreseen interaction point. Out of the bunch spacing and the length of the interaction region it can easily be calculated

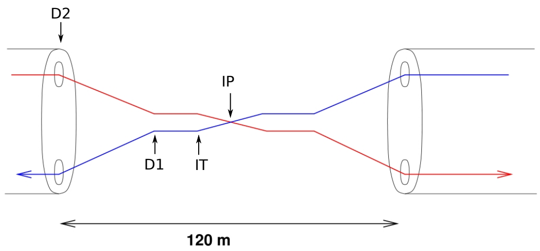

Figure 1.1: Cross over between inner and outer vacuum chamber in the LHC (schematic) [2]. IT = inner triplet magnets, D1 and D2 = separation-recombination dipoles.

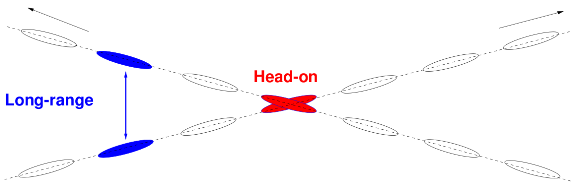

Figure 1.2: Head-on and long-range interactions in a LHC interaction point [2].

that around 30 bunch encounters in one of the four LHC interaction regions can be expected, i.e. in total 120 interactions. Except for the interactions in the IP, the rest are undesirable and they must be avoided to not unnecessarily disturb the beam. The insertion of a crossing angle eliminates all unwanted head-on collisions but leads to the so-called long-range interactions as illustrated in Figure 1.2.

The long-range interactions imply that the bunches still feel the electromagnetic forces from the bunches of the opposite beam. When the separation is large enough, these long-range encounters should be weak. In nominal LHC the bunches collide at a small crossing angle of 285 μrad. The typical separation between the two beams is between 7 and 10 in units of the beam-size of the opposing beam [2]. Therefore, long-range interactions destroy the beam much less than head-on interactions, but due to their large number and some particular properties they require careful studies.

From now on it will be distinguished between these two regimes of beam-beam interactions:

- Head-on interactions (HO), short range electromagnetic interactions.
- Long-range interactions (LR), long-range electromagnetic interactions.

1.2 Fields and Forces

1.2.1 Beam-Beam Force

To calculate the effect one beam has on a particle in the opposite beam the electromagnetic fields ($\vec{E}$, $\vec{B}$) of the beam with a particle density distribution $\rho(x, y, z)$ needs to be known. In the rest frame of the moving beam the fields are electrostatic and they can be calculated via the electrostatic potential.

Any charged particle density distribution ρ generates an electrostatic field ($\vec{E}'$, $\vec{B}' \equiv 0$):

$$\vec{\nabla}\vec{E}' = \frac{\rho}{\epsilon_0} \tag{1.4}$$

The electrostatic field can be calculated from the divergence of a potential

$$\vec{E'} = -\vec{\nabla}\Phi(x, y, z) \tag{1.5}$$

Bringing 1.5 into 1.4 the following expressions are obtained:

$$-\vec{\nabla}(\nabla\vec{\Phi}) = \frac{\rho}{\epsilon_0} \implies \Delta\Phi = -\frac{\rho}{\epsilon_0} \tag{1.6}$$

where $\vec{\nabla} \cdot \vec{\nabla} = \Delta$ is used. Equation 1.6 is known as the Poisson equation. Knowing the charged density distribution ρ, the potential can be obtained and from the potential the electrostatic fields from 1.5.

One particular solution of the Poisson equation is [5]

$$\Phi(x, y, z) = \frac{1}{4\pi\epsilon_0} \int \frac{\rho(x, y, z)dV}{R} \tag{1.7}$$

In case of beams with (2D) Gaussian charged particle density distributions

$$\rho(x, y) = \frac{NZ_1 e}{2\pi\sigma_x\sigma_y} \exp\left(-\frac{x^2}{2\sigma_x^2} - \frac{y^2}{2\sigma_y^2}\right) \tag{1.8}$$

with N particles of the charge $q = Z_1 e$ the potential becomes [2]

$$U(x, y, \sigma_x, \sigma_y) = \frac{NZ_1 e}{4\pi\epsilon_0} \int_0^\infty \frac{\exp\left(-\frac{x^2}{2\sigma_x^2+q} - \frac{y^2}{2\sigma_y^2+q}\right)}{\sqrt{(2\sigma_x^2 + q)(2\sigma_y^2 + q)}} dq \tag{1.9}$$

As said before, once the potential is known, one can get the electrostatic field $\vec{E'}$. Since the beam is moving the field has to be Lorentz transformed into the moving frame:

$$E_\parallel = E'_\parallel, \quad E_\perp = \gamma \cdot E'_\perp \tag{1.10}$$

The Lorentz force $\vec{F}$ on a particle with charge $q = Z_2 e$ can be calculated with

$$\vec{B} = \vec{\beta} \times \vec{E}/c \tag{1.11}$$

$$\vec{F} = q(\vec{E} + \vec{\beta}c \times \vec{B}) \tag{1.12}$$

where $\gamma = 1/\sqrt{1 - \beta^2}$ is the Lorentz factor and $\vec{\beta} = \vec{v}/c$ is the relativistic beta.

For very relativistic particles ($\beta \approx 1$) and under the assumptions of round beams ($\sigma_x = \sigma_y = \sigma$, which is a good assumption for a hadron collider) and $Z_1 = Z_2 = 1$ the resulting Lorentz force has only a radial component, i.e. depends only on the distance r from the bunch center (where $r^2 = x^2 + y^2$), since only the components E_r and B_Φ

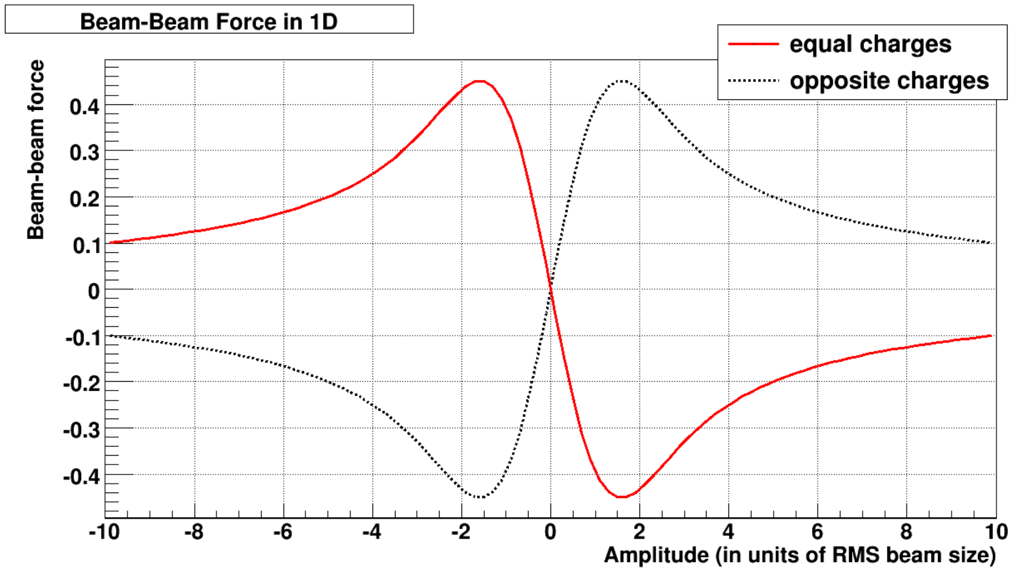

Figure 1.3: Amplitude depending part of the beam-beam force (kick) $F \propto \pm(1 - \exp(-r^2/2))/r$ as a function of the amplitude for equal charges (solid red line) and for opposite charges (dashed black line).

are non-zero [2] :

$$F_r(r) = -\frac{Ne^2(1+\beta^2)}{2\pi\epsilon_0 \cdot r}\left[1 - \exp(-\frac{r^2}{2\sigma^2})\right] \tag{1.13}$$

The resulting force is shown in Figure 1.3 for equal ($Z_1 = Z_2$) and opposite charges ($Z_1 = -Z_2$). Under the use of Newton's law, Equation 1.13 can be integrated over the collision region, i.e. the time of the passage Δt, to calculate the kick $\Delta r'$. This quantity represents the change in angle of a single particle trajectory (with respect to the design orbit) due to the collision in spherical coordinates ($r^2 = x^2+y^2$). The incoming particle is deflected by the beam, which acts on it as a focal lens, see Figure 1.4. This can be described in the coordinates (x, x', y, y'), where x, y are the positions and x', y' are

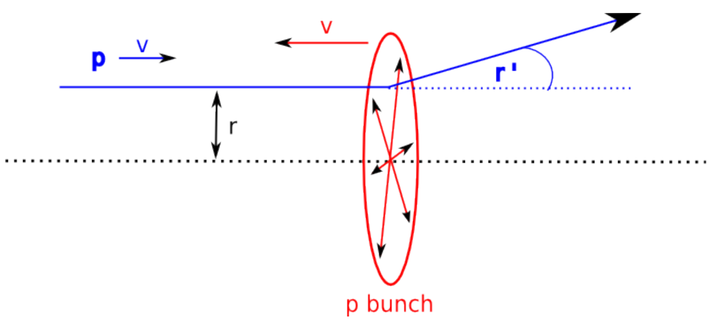

Figure 1.4: Incoming particle is deflected (kicked) by beam-beam force [1].

the angles of the particle with respect to the design orbit. The deflections $\Delta x'$ and $\Delta y'$ give the angles by which the particle is deflected during the passage, i.e. the kick due to the beam-beam force:

$$\Delta r' = -\frac{2Nr_0}{\gamma} \cdot \frac{r}{r^2} \cdot \left[1 - \exp(-\frac{r^2}{2\sigma^2})\right] \tag{1.14}$$

1.2.2 Linear Beam-Beam Tune Shift

In Figure 1.5 the kick (red curve) can be seen as a function of the amplitude (in units of beam-size), where the amplitude is the offset of a single particle with respect to the center of the beam it passes. For very small amplitudes ($< 1\sigma$) the beam-beam force is linear and can be interpreted as having the same effect of a quadrupole (green curve). For bigger amplitudes ($> 1\sigma$) the beam-beam force becomes very non-linear and can no longer be approximated by a simple multipole. Hence, only in the linear regime the beam-beam strength can be quantified.

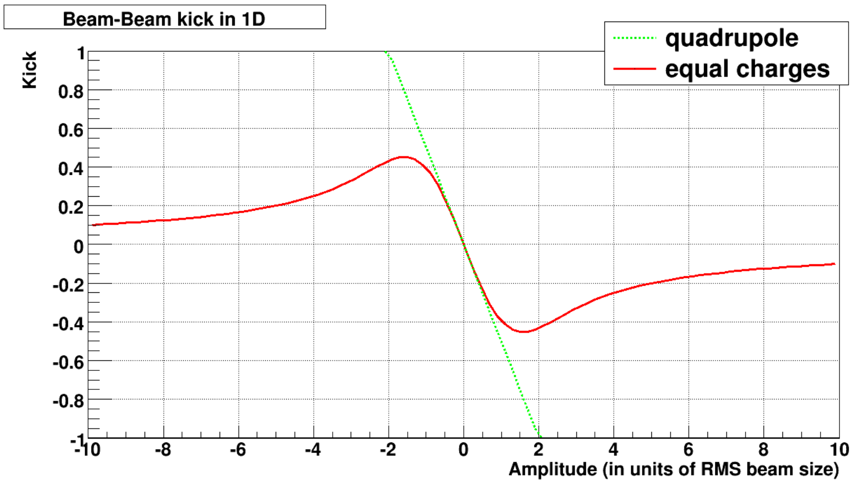

Figure 1.5: Amplitude depending part of the beam-beam force (kick) $F \propto -(1 - \exp(-r^2/2))/r$ as a function of the amplitude for equal charges (solid red line) and in comparison the kick of a quadrupole which has the same strength as the beam-beam kick in the linear regime (green curve).

A Taylor expansion of the exponential part in brackets of the beam-beam kick $\Delta r'$ from Equation 1.14, taken at the limit of zero amplitude, illustrates the quadrupole behaviour in the linear regime. After some simplifications the following expression is obtained:

$$\Delta r' \mid_{r\to 0} = \frac{Nr_0 r}{\gamma\sigma^2} = f \cdot r \tag{1.15}$$

which is linear in r as for the case of a quadrupole, where the proportionality factor f is representing the focal length.

The effect of this behaviour on the beam can be understood by looking at the kick given by a normal quadrupole. The horizontal kick x' of a quadrupole can be seen as a change in angle which can be estimated via

$$x' = \frac{l}{\rho} \tag{1.16}$$

where l is the path length the particle travels in the quadrupole field and ρ is the bending radius of the deviation curve inside the magnet. Multiplying by $1 = B/B$ and replacing $B = gx$ in the numerator, where $g = k \cdot (p/q)$ is the gradient of the quadrupole field, and the beam rigidity $B\rho = p/q$ in the denominator, Equation 1.16 can be rewritten as

$$x' = \frac{B \cdot l}{B \cdot \rho} = \frac{gx \cdot l}{p/q} = \frac{k(p/q) \cdot x \cdot l}{p/q} = kl \cdot x = f \cdot x \tag{1.17}$$

here f is equal to the inverse of the focal length $F = 1/kl$. Thus, the same linear behaviour as for the linear beam-beam force is obtained.

But since no quadrupole can be built with a perfect field, small errors Δk in the field strength k will occur. Such an error leads to a change in tune (tune shift)

$$\Delta Q = \frac{1}{4\pi} \int \Delta k \beta ds \tag{1.18}$$

where the integral has to be carried out over the length of the considered quadrupole and with β as the beta-function at its position. As seen before, the quadrupole strength can be expressed in terms of the field gradient:

$$g = \frac{dB}{dx} \tag{1.19}$$

From this it follows that a change in tune ΔQ is proportional to the derivative of the magnetic field. In conclusion, the focal length of a quadrupole relates to the experienced tune shift which is proportional to the derivative of the applied force.

With this in mind the linear beam-beam parameter ξ for head-on interactions of round beams with $\beta^* = \beta^*_x = \beta^*_y$ can be derived:

$$\xi = \frac{N r_0 \beta^*}{4\pi \gamma_{rel} \sigma^2} \tag{1.20}$$

where N is the bunch intensity, $r_0 = e^2/4\pi\epsilon_0 mc^2$ is the classical particle radius, β^* is the optical amplitude function (β-function) of the particle at the interaction point, $\gamma_{rel} = E/m_0$ is the relativistic γ describing the fraction between the energy and the rest mass of the particle and σ describes the transverse beam size at the interaction point.

The beam-beam parameter can be generalized for the case of non-round beams, but Gaussian particle distributions in both planes:

$$\xi_{x,y} = \frac{N r_0 \beta^*_{x,y}}{2\pi \gamma_{rel} \sigma_{x,y}(\sigma_x + \sigma_y)} \tag{1.21}$$

For small values of ξ and a tune far enough away from linear resonances this parameter is proportional to the linear tune shift ΔQ_{bb} due to beam-beam interactions. The change in tune due to beam-beam interactions is to be added to the unperturbed tune Q set by the main quadrupoles in the machine. This perturbation due to head-on collisions occurs in both planes and can be focusing or defocusing, depending on the charges of the colliding particles. If the beams consist of opposite charged particles (e.g colliding electron-positron or proton-antiproton beams) the effect is focusing, by considering equally charged beams, as the two colliding proton beams in LHC, one obtains a defocusing effect, which leads to a decrease in tune.

One can visualize this defocusing effect by thinking of the repulsion between two equally charged particles. The beams will repulse each other, resulting in a kick which has the same direction as one of a defocusing quadrupole. Vice versa, from the attraction between two opposite charges a focusing effect follows. In the linear regime the beam-beam force is focusing in both planes. However, a quadrupole is focusing in the one and defocusing in the other plane.

Starting from the standard working point (blue X in Figure 1.6) a linear tune-shift (ΔQ_{bb}) would lead to a new tune (red X) after applying a linear force, Figure 1.6 left. Since the beam-beam force is very non-linear and depends on the amplitudes of the particles with respect to the center of the crossed beam, the resulting tune-shift for each particle also depends on its amplitudes in both planes. After a beam-beam interaction the perturbed beam will no longer show a single tune, rather a tune spread like indicated by the red area on the right hand side of Figure 1.6. The tune measurement evolves in a frequency spectra which approximately has the width of the linear beam-beam parameter ξ. As it was mentioned before, ξ is a measure of the linear tune-shift due to beam-beam interactions which was derived from the derivative of the beam-beam force at the limit of zero amplitudes. Thus, it will be an upper limit for the values inside the tune spread caused by the non-linear regime of the force, because the derivative has its only maximum at zero amplitude.

This indicates that the determination of the linear beam-beam parameter ξ is a good measure for the strength of the beam-beam interaction in case of ideal head-on collisions. It can be used for comparison and as a scaling parameter. One of the main analysis done here is the calculation of ξ out of data for the beam-sizes and intensities which is then compared to direct tune measurements. However, it only describes the linear regime of the beam-beam force and can not be compared to the non-linear part. Furthermore, it does not indicate any information about the change to the optical functions (β-beating) which comes together with a change in tune.

The assumptions which have been made to derive this parameter describe the case of

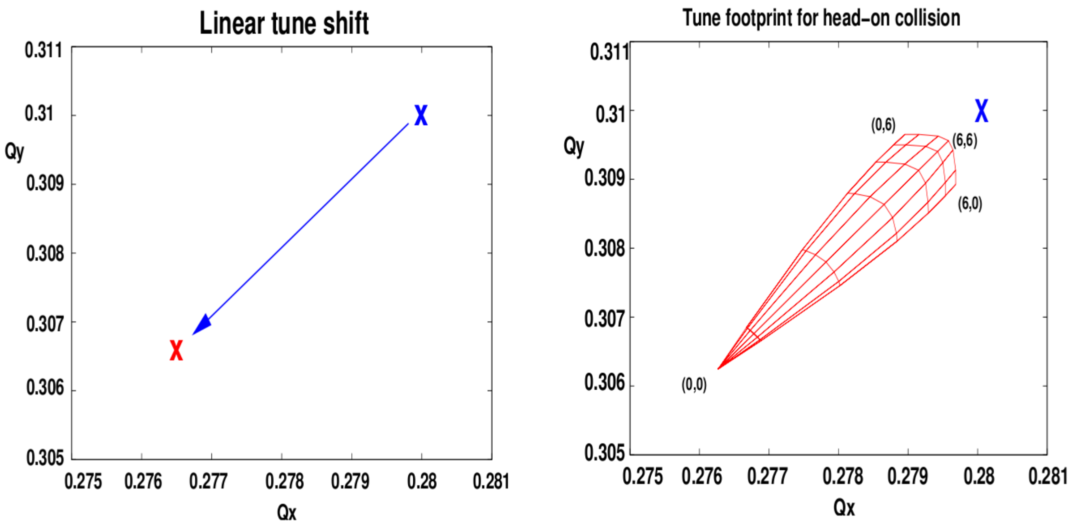

Figure 1.6: Left: linear tune-shift caused by a linear force. Right: footprint of the tune spread caused by a non-linear beam-beam force. The blue X indicates the position of the unperturbed working-point, the red X/bordered region represents the point/area in which the single particle tunes are located after a head-on collision with the opposite beam when a linear/non-linear force is exerted [1].

the LHC very well. The LHC is a high energy hadron collider in which round Gaussian beams are in general a good approximation. On the other hand, the assumptions made above would not describe the conditions for instance in LEP very well. Even if in LEP the particles are accelerated to ultra relativistic energies, the beams are very asymmetric in both transversal planes. The horizontal beam-size is much bigger than the vertical one, because the beams are deviated by the dipole-magnets in the horizontal plane, the beam profile in this plane increases due to synchrotron radiation.

In Table 1.1 all parameters needed to calculate the linear beam-beam parameter for the LHC under nominal conditions are given.

Parameter	LHC(pp)
Energy	7 TeV
Intensity N	$1.15 \cdot 10^{11}$/bunch
Beam size $\sigma_x \cdot \sigma_y$ (in IP1 & 5)	$16.6\,\mu$m $\cdot\, 16.6\,\mu$m
$\beta^*_x \cdot \beta^*_y$ (in IP1 & 5)	0.55 m $\cdot$ 0.55 m
Crossing angle	285 μrad
Beam-beam parameter (ξ)	0.0037

Table 1.1: Nominal LHC parameters to calculate the theoretical linear beam-beam parameter ξ for one collision [8].

1.3 Resulting Effects

In this section, the effects of the fields and forces discussed in Section 1.2 on the beam dynamics are summarized.

1.3.1 Incoherent Effects

Incoherent effects are effects on single particles. They can not be measured directly, but their evaluation is done by simulations to help in the understanding of the data.

However, as discussed above, all single particles in one beam will be affected by the beam-beam force exert by the opposite beam. The beam will act on each single particle of the counter rotating beam as a complex, static electromagnetic lens. It should be clear that the exerted force is very non-linear and highly depending on the amplitude, therefore one has to expect all effects known from non-linear beam dynamics, depending on the complexity of the lens.
As the main effects of beam-beam interactions which will deviate the particles from their linear and stable dynamics one has to expect the following [3]:

- Non-linear detuning and excitation of resonances.
- Transverse phase space modification and beam blow up.
- Unstable and/or irregular motion
- Dynamic aperture reduction, bad lifetime and particle losses.
- Dynamic beta effects.

1.3.2 Coherent Effects

Coherent beam-beam effects are collective and organized motions of many particles or bunches. They arise from the force which an exciting bunch exerts on a whole test bunch during beam-beam collisions. A coherent kick is seen by the entire bunch, which is the difference to the incoherent kick, where only the effect on a single particle is considered. By coherent motion of bunches, the collective behaviour of all particles in a bunch is meant.

The calculation of the coherent force between two charged, Gaussian particle distributions, is done as for the incoherent case in Chapter 1.2. The computation of the coherent kick requires the integration of the individual incoherent kicks of all test particles over the bunch distribution. Analogue to the incoherent case, only by taking the bunch barycentres (X, Y) as the coordinates of the bunches (instead of the positions of the single particles x and y) this leads, in the limit of exact head-on collisions ($\bar{r} \to 0$), to a coherent kick given by the expression:

$$\Delta \bar{r}' \mid_{\bar{r} \to 0} = \frac{N r_0 \bar{r}}{2 \gamma \sigma^2} = F \cdot \bar{r} \tag{1.22}$$

Where the kick can again be represented by a quadrupole with an inverse focal length of $F = f/2$, being only half the value of the incoherent one, f. This quantity again relates to a tune change and, like in the incoherent case, a coherent beam-beam parameter Ξ for $\bar{r} \to 0$ can be defined. For the case of elliptical Gaussian bunches it is of the form

$$\Xi_{X,Y} = \frac{N r_0 \beta^*_{X,Y}}{4\pi\gamma\sigma_{X,Y}(\sigma_X + \sigma_Y)} \tag{1.23}$$

For round beams ($\sigma_X = \sigma_Y$) it simplifies to

$$\Xi_{X,Y} = \frac{N r_0 \beta^*_{X,Y}}{8\pi\gamma\sigma^2} = \frac{1}{2}\xi_{X,Y} \tag{1.24}$$

For small amplitudes ($r << \sigma$) the overall effect on the entire beam is therefore only half the effect on a single particle. At large distances this is no longer true, because the bunches appear to each other as a point like source and the force can be approximated with the effect on a single particle [3].

Due to the beam-beam interactions the beams can couple through the beam-beam force and develop a collective behaviour. Therefore the beam will not only show perturbed single particle dynamics but also new coherent effects, like

- Orbit effects
- Coherent oscillating modes
- Multi Bunch coupling

This thesis will focus on the analysis of coherent effects, and in particular on orbit effects and the coherent tune shift.

1.4 Long-Range Interactions

Long-range interactions break the symmetry between the planes and can lead to stronger excitation of resonances. They mostly affect particles at large amplitudes and they cause effects on the tune and closed orbit, e.g. PACMAN-effect.

In ATLAS (IP1) and ALICE (IP2) the beams are colliding with a crossing angle in the vertical plane and in CMS (IP5) and LHCb (IP8) in the horizontal plane. The orthogonal plane is called separation plane, since here the beams can be separated to reduce or avoid collisions, without touching the crossing angle in the other plane. In IP1 and 5 the beams collide head-on without separation, but in IP2 and 8 a separation is applied in the orthogonal plane to the crossing angle plane, i.e. the beams see long-range interactions in both planes in IP2 and 8, whereas in IP1 and 5 the beams only suffer from long-range encounters in the crossing plane. The alternating crossing scheme is used to compensate for the effect of long-range interactions. The functionality can be easily understood by considering for instance a normal quadrupole focusing in the horizontal plane. It is well known that this quadrupole will act as a defocusing element in the vertical plane, where an analogue behaviour of the long-range interactions can be found.

The tune shift due to long-range interactions has the opposite sign compared to that caused by head-on interactions, see Figure 1.7. For small amplitude particles, represented with a blue spot, the effect can be approximated as a defocusing quadrupole (for equally charged beams). But if particles at larger amplitudes ($r > 2\sigma$, yellow spot) are considered, the local slope of the kick due to the beam-beam interactions changes sign. Thus, the particles are kicked in the opposite direction and are focused instead of defocused.

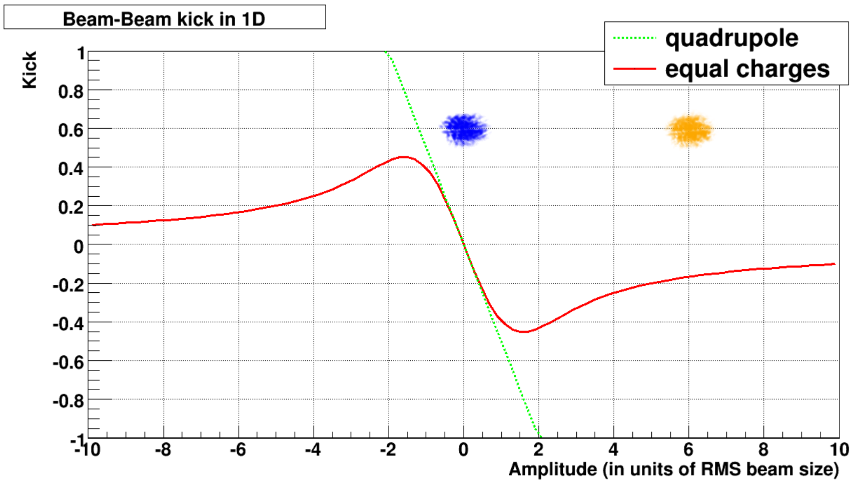

Figure 1.7: The opposite sign of the tune shift due to long-range interactions, arises from the opposite slope of the beam-beam kick at larger amplitudes [1].

If the beams are crossing in the vertical plane in IP1, the long-range effects will focus the beams in the vertical (since here the bunches are separated by the crossing angle) and defocus them in the horizontal plane (since here they collide head-on with zero separation). Arriving at IP5, they cross in the horizontal plane, which leads to a swap of the focusing due to beam-beam interactions with respect to IP1 (focus horizontally and defocus vertically). This entails the same behaviour as a FoDo-cell and results in a compensation of the undesired effects to the tune.

It can easily be seen that the effects caused by the long-range interactions depend on the size of the separation d_{sep}. The closer the bunches are, the stronger the field they feel, thus the kick becomes stronger (Figure 1.8). The number of long-range interactions depends on the spacing between bunches and the length of the common vacuum pipe. However, it can be calculated that the resulting tune shift for one particular interaction follows (for large enough d_{sep}) the proportionality relation [2]

$$\Delta Q_{LR} \propto -\frac{N}{d_{sep}^2} \tag{1.25}$$

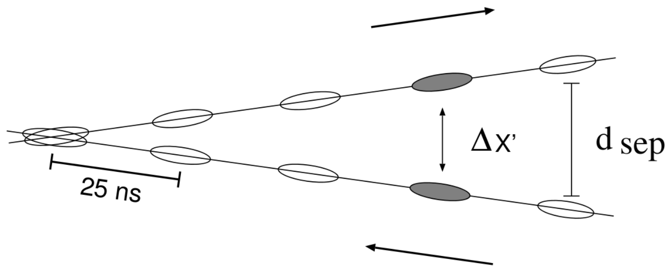

Figure 1.8: Long-range interactions depend on the separation d_{sep} [1].

As mentioned before, the tune shift is proportional to the derivative of the applied force, hence it can be seen from Equation 1.25, that for well separated beams ($d >> \sigma$) the force (kick) has an amplitude independent contribution, which changes the orbit. The whole bunch sees a kick as an entity (coherent kick), which can excite coherent dipole oscillations. Moreover, all bunches couple because each bunch sees many opposing bunches and therefore many coherent modes are possible. In daily operation the separation, due to the crossing angle, between two bunches in LHC is maximal around 10 in units of beam-size, thus it is not unusual to reach the regime where the beam-beam kick changes its sign.

Furthermore, more problems must be expected for small crossing angles. In this cases the interactions become stronger, since the separation decreases. For very small separations particles become unstable and get lost.

PACMAN-Effect

For high luminosity operation, the LHC is filled with 39 batches of 72 bunches with a 25 ns spacing in each batch, this sums up to 2808 bunches. But from the length of the ring one can calculate that for a spacing of 25 ns 3564 bunch positions are possible, i.e. this scheme contains 756 gaps between the batches, see Figure 1.9.

The gaps are unavoidable and necessary to give the SPS (Super Proton Synchrotron) and LHC kickers time to rise to inject the next batches from the PS (Proton Synchrotron) into the SPS and later on into the LHC [7]. These gaps cause the so-called PACMAN-effect. PACMAN-bunches are the bunches which see fewer unwanted long-range interactions in total, because they are located at the head or tail of a bunch train and they do not have an interaction partner from the arriving or leaving counter rotating beam, see Figure 1.10. The result is a left-right asymmetry which leads to a maximum of 120 and a minimum of 40 long-range collisions for different bunches. Bunches at different positions in a bunch train therefore experience different orbit kicks, which results in bunch-by-bunch differences in the offset with respect to the reference orbit. PACMAN-bunches have a different offset than the bunches in the middle of a bunch train which experience all possible long-range interactions.

Due to the orbit changes the lattice properties also change, which can cause particle

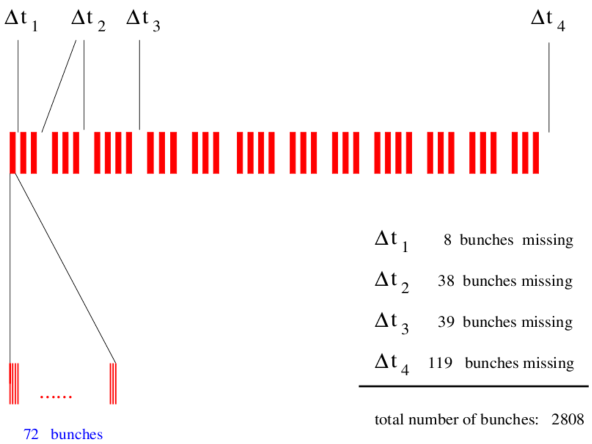

Figure 1.9: Nominal bunch filling scheme for the LHC [6].

losses, thus orbit effects must be corrected. This is done with Closed Orbit Dipoles (COD), but the different bunch-by-bunch offsets arising from the PACMAN-effect make this correction difficult. For a perfect correction the COD would need to apply an individual kick to each bunch depending on its actual offset to bring it back to the reference orbit. But since the bunch spacing in the nominal LHC is so small, no dipole corrector magnet can rise fast enough to produce individual strengths per bunch. This orbit correction can only be done on the whole beam implying that the PACMAN-bunches are over corrected.

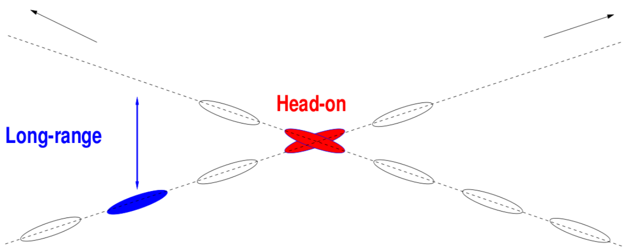

Figure 1.10: Bunches at the head or tail of a train can miss one or more long-range interactions, due to the lack of an interaction partner in the opposite beam, e.g. blue bunch, this bunches are so-called PACMAN-bunches [1].

2 The Large Hadron Collider

The Large Hadron Collider (LHC) is the world's largest and highest-energy particle accelerator. It addresses some of the most fundamental questions in physics and advances the understanding in the deepest laws of nature. In the following chapter this remarkable machine is introduced in some detail according to the topic of this thesis, for more detailed reading [8], [9], [10].

2.1 Physics Motivation

The Standard Model of particles and forces summarizes our current knowledge of particle physics. In various particle physics experiment new particles were discovered which were previously predicted only by the theory of the Standard Model. Moreover, the results of the performed experiments turned out to be in an amazingly good agreement with this Model. Unfortunately, the predictive power of this model is limited and still leaves many unsolved questions. The LHC was built to give help in finding answers to the remaining fundamental questions in physics and to advance the understanding in the deepest laws of nature. The main issues are listed in the following [11]:

- Why do particles have mass? Why are some very heavy while others have no mass at all? The theory of the so-called Higgs mechanism could explain this phenomenon. It relies on the postulation of the Higgs-field which fills the whole space and is produced by the Higgs boson. Particles acquire mass when they couple to the Higgs boson. Heavy particles couple more strongly than light particles. If such a particle exists the LHC is able to find it.
- The Standard Model explains the three fundamental forces (electromagnetic, weak and strong force) very well, but it does not include gravity, therefore it also does not state why gravity is so many orders of magnitude weaker than the other forces (hierarchy problem). The Supersymmetry, an expansion of the Standard Model, which predicts more massive partners to the Standard Model particles, gives the possibility to unify the fundamental forces including gravity. If this theory is right, the lightest supersymmetric particles should be found at LHC.
- Astronomical and cosmological observations have shown that the amount of visible matter (atoms) in the universe is only around 4 %. The other 96 % of the universe can be divided into two categories, the so-called dark matter (23 %) and dark energy (73 %). It is not yet clear what they consist of, but one theory predicts that dark matter is made of supersymmetric particles, which are still

undiscovered until now.

- During the Big Bang matter and antimatter must have been produced in the same amount, but apparently our universe consists of matter. The origin of this antisymmetry between matter and antimatter is still a mystery which is hoped to be solved at the LHC.
- At the LHC not only proton-proton collisions but also heavy-ion collisions are performed. They are used to investigate the so-called quark-gluon-plasma which would have been a stage in the early universe during which the matter present today was evolved. The experiments are aimed to yield a better understanding of the processes taking place at the time of the construction of the universe, which is expected to lead to answers to the open questions left by the Standard Model.

2.2 The Machine

As the name implies, in the Large Hadron Collider two hadron beams are accelerated in two separated rings and brought into collision at four interaction points (IP). Through slightly different pre-accelerator chains, protons are accelerated up to a maximum energy of 7 TeV per particle or, alternatively, lead ions up to 575 TeV per nucleus. Under nominal conditions one proton beam is made of 2808 bunches, each contains about 1.15×10^{11} particles, this means that the overall stored energy in one beam reaches around 360 MJ, which is comparable to the energy of an aircraft carrier at half speed. The LHC will provide its four experiments ATLAS, ALICE, CMS and LHCb (see Figure 2.1) with a luminosity of $10^{34}\,\mathrm{cm}^{-2}\mathrm{s}^{-1}$. To force the particles on their circa 26.7 km long circular obit, over 8000 superconducting magnets are used. From which the main dipole magnets reach a maximum strength of 8.3 T at top energy [8].

Apart from the magnets various other elements are required to obtain a stable and secure operation with storage times of 10 hours and more. Some of them are introduced briefly in the following section.

2.2.1 Injection System

Due to technical reasons it is not possible to inject the particles with a kinetic energy of nearly zero directly form the source into the LHC and accelerate them up to 7 TeV. There is no magnet that can cover a dynamic rage from 0 to 7 TeV. On the other hand, it is difficult to reproduce very small magnetic fields, which would be needed at small kinetic energies, due to the remanence of the iron magnets. Hence, a chain of miscellaneous pre-accelerators is used to increase the energy step by step up to 450 GeV, the injection energy of the LHC.

The pre-accelerator chain starts with a source of protons with a kinetic energy of 90 keV from a duoplasmatron. It is followed by a radiofrequency quadrupole (RQF) which accelerates the particles up to 750 keV. The connected linear accelerator (LINAC2)

LHC nominal parameter

	Injection	Collision	Unit
Beam data			
Proton energy	0.45	7	[TeV]
Relativistic gamma	479.6	7461	
Number of bunches	2808		
Number of particles per nominal bunch	1.15×10^{11}		
Number of particles per pilot bunch	5×10^{9}		
Transverse normalised emittance	3.75		[μm.rad]
Longitudinal emittance (4σ)	1.0	2.5	[μeVs]
Mean circulating current per beam	0.582		[A]
Stored energy per beam	23.3	362	[MJ]
Bunch spacing	25		[ns]
RMS bunch length	11.24	7.55	[cm]
RMS beam size in arc	1.19	0.3	[mm]
RMS beam size at IP1 & IP5 ($\beta = 0.55\,\mathrm{m}$)	375.2	16.7	[μm]
RMS beam size at IP2 & IP8 ($\beta = 10\,\mathrm{m}$)	279.6	70.9	[μm]
Interaction Data			
Number of collision points	4		
Half crossing angle for ATLAS and CMS (IP1/5)	±160	±142.5	[μrad]
Half crossing angle for ALICE (IP2)	±240	±150	[μrad]
Half crossing angle for LHCb (IP8)	±300	±200	[μrad]
Peak luminosity in IP1 & IP5	-	1.0×10^{34}	[$\mathrm{cm}^{-2}\mathrm{s}^{-1}$]
Peak luminosity in IP2 & IP8	-	3.56×10^{30}	[$\mathrm{cm}^{-2}\mathrm{s}^{-1}$]
Geometry			
Circumference	26658.883		[m]
Ring separation in arcs	194		[mm]
Revolution frequency	11.245		[kHz]
Main Dipole			
Number of main dipoles	1232		
Length of main dipoles	14.3		[m]
Magnetic field	0.535	8.33	[T]
Bending radius	2803.95		[m]
Lattice			
Horizontal tune	64.28	64.31	
Vertical tune	59.31	59.32	

Table 2.1: Parameter for nominal LHC [8].

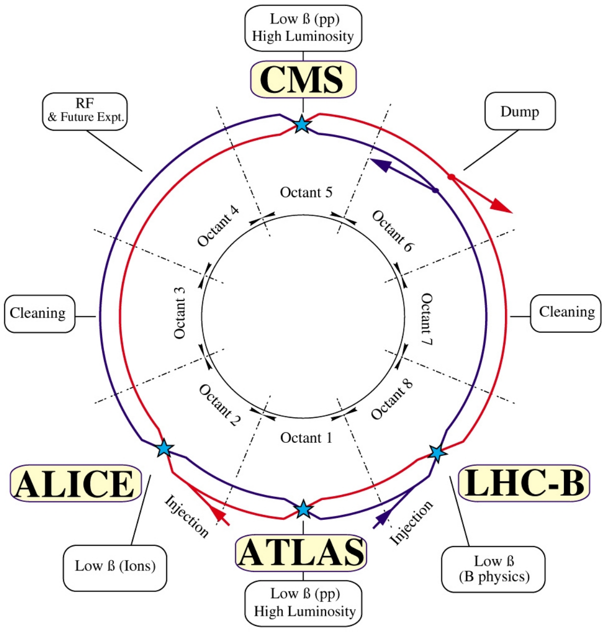

Figure 2.1: Geometrical layout of the LHC [12].

increases the energy further, so that the protons can be injected into the first circular accelerator, the Proton Synchrotron Booster (PSB), with an energy of 50 MeV. The PSB consist of four superposed rings that operate four beams in parallel, i.e. it can accelerate four beams at the same time. Each ring has a circumference of 157 m. The particles leave the PSB with 1.4 GeV energy. Now they are injected into the Proton Synchrotron (PS) with a circumference of 628.3 m ($\sim 4 \times 157$ m, which is the sum of the four PSB rings) and brought to the extraction energy of 25 GeV. Through a transfer-line, the protons are now led to the Super Proton Synchrotron (SPS) which is the last pre-accelerator before injection into the LHC. On a circumference of 6912 m, the SPS brings the protons to the LHC injection energy of 450 GeV. After the extraction from the SPS both proton beams are injected over two transferlines in reverse directions into the LHC, so that two counter rotating beams can be stored and brought into collsions. The LHC itself is able to accelerate the particles now up to a maximum energy of 7 TeV. The full proton accelerator chain is displayed in Figure 2.2.

Due to the different type of particles a slightly different pre-accelerator chain has to be used for the ion mode.

2.2.2 Magnets

To accelerate particles, one of the four fundamental forces needs to be used. Due to the short range of the strong and weak force they can not be used for this purpose and gravity is way to weak. Therefore, only electromagnetic forces are useful for this purpose.

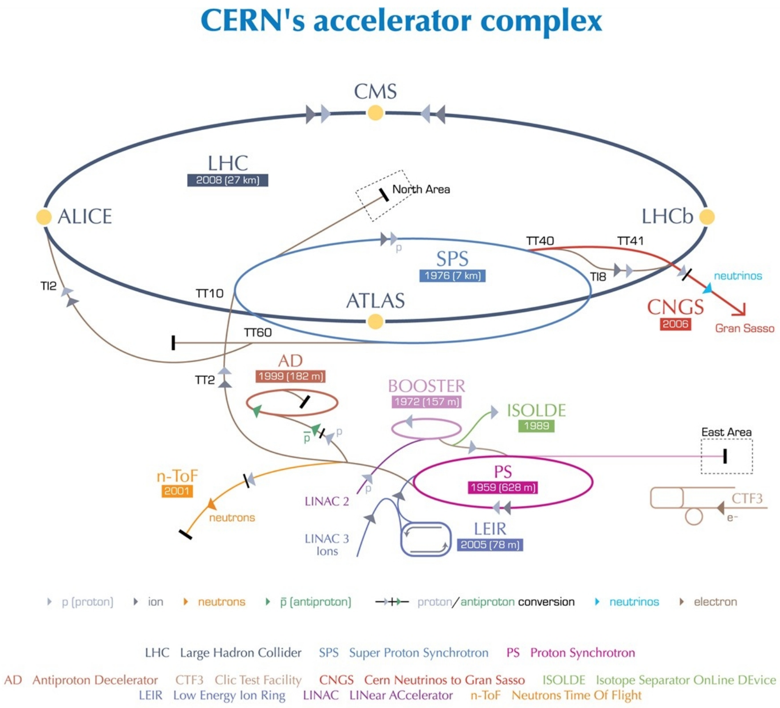

Figure 2.2: CERN accelerator complex to (pre-)accelerate the protons up to their maximum energy of 7 TeV [12].

On a particle with charge q and velocity $\vec{v}$ moving through the space in which a magnetic field $\vec{B}$ and an electric field $\vec{E}$ is present the Lorentz force

$$\vec{F} = q(\vec{v} \times \vec{B} + \vec{E}) \tag{2.1}$$

is exerted. The energy transferred to the particle is the integral over the covered distance:

$$\Delta E = q \int_{r_1}^{r_2} (\vec{v} \times \vec{B} + \vec{E}) d\vec{r} \tag{2.2}$$
$$= q \int_{r_1}^{r_2} \vec{E} d\vec{r} = qU \tag{2.3}$$

Since the velocity vector $\vec{v}$ is parallel to the direction vector $\vec{r}$ the scalar product $(\vec{v} \times \vec{B})d\vec{r}$ is zero. From this it can be concluded that only the electric field is responsible for the increase in energy of a charged particle, magnetic fields are only used for deflection.

If a particle is deflected in a magnetic field, Lorentz and Centripetal force are always equal. This leads to the beam rigidity $B\rho$:

$$F_L = F_C \Longleftrightarrow \frac{mv^2}{\rho} = qvB \Longleftrightarrow B\rho = \frac{mv}{q} = \frac{p}{q} \tag{2.4}$$

where ρ is the bending radius and $p = mv$ the particle momentum. A multipole expansion of the magnetic field $\vec{B}$ and multiplication by e/p gives [13]

$$\frac{e}{p}B_z(x) = \frac{e}{p}B_{z0} + \frac{e}{p}\frac{dB_z}{dx}x + \frac{1}{2!}\frac{e}{p}\frac{d^2B_z}{dx^2}x^2 + \frac{1}{3!}\frac{e}{p}\frac{d^3B_z}{dx^3}x^3 + ... \quad (2.5)$$

$$= \frac{1}{\rho} + kx + \frac{1}{2!}mx^2 + \frac{1}{3!}ox^3 + ... \quad (2.6)$$

where the first term corresponds to a dipole, the second one to a quadrupole, the third one to a sextupole, the forth one to an octupole, etc. The magnetic field may therefore be regarded as a sum of multipoles, each of which have a different effect on the path of the particle. This can be used for different corrections on the beam.

Dipoles are used to bend the particles to a circular orbit to make them pass the same machine elements over and over again.

Quadrupoles are used for the focusing. A particle accelerator is build in a way that an ideal reference particle (i.e. a particle with design energy/momentum, $\frac{\Delta p}{p} = 0$, $x = y = 0$, $x' = y' = 0$) follows the design orbit, which lies in the middle of all machine elements. In absence of field errors and magnet misalignments focussing would not be needed for such a design particle. But since the LHC operates under nominal conditions with 2808 bunches each with 1.15×10^{11} particles, it is unavoidable that some particles have a slightly different momentum, an offset (x- or y-position) and/or an angle (x' or y') to the design orbit. Due to this variations the magnets apply a wrong deflection on the particles which would lead to particle losses without the correction due to the focussing effect of the quadrupoles.

By construction a horizontal focusing quadrupole is defocusing in the vertical plane, therefore one needs to locate a second quadrupole rotated by 90° some distance behind the first one to correct for this behaviour, a so-called FoDo-Cell is built. This alternating focusing-defocusing structure has to be repeated around the whole ring to force the particles on a trajectory around the design orbit. More precisely, the particles are excited to oscillate around the design orbit, the so-called betatron oscillation. The number of oscillations a particle performs during one turn around the machine is called tune. Every accelerator has two tune values, namely Q_x in the horizontal and Q_y in the vertical plane. In general these two values are different. Only the fractional part contains useful information for daily operation, since it can be varied by adjusting the strength of the quadrupoles, whereas it is very unlikely that the number of complete oscillations will be changed. In daily operation when talking about the tune one always refers to the fractional part.

Nevertheless, certain fractional values of the tunes have to be avoided as they lead to resonant excitation and possible loss of the beam. If the condition

$$nQ_x + mQ_y = l \quad (2.7)$$

is fulfilled, with n, m and l integers, the tune catches a resonance of order $|n| + |m|$.

In general, due to the finite mechanical tolerance and the limited pole width of the magnets, all possible multipole fields are present in an accelerator. Hence, higher order

	Magnet	Description
main magnets	MB MQ	dipole: main bending magnet quadrupole: main focusing/defocusing magnet
dipole spool pieces	MCS MCD MCO	sextupole: corrects sextupolar component of the dipole field decapole: corrects decapolar component of the dipole field octupole: corrects octupolar component of the dipole field
correctors attached to main quadrupoles	MCB MQT MQS MSC MO	dipole: corrects closed orbit quadrupole: corrects tune skew quadrupole: rotated by 45°, corrects coupling sextupole: corrects beam chromaticity octupole: Landau damping (damps beam excitations)

Table 2.2: Magnets used in a LHC FoDo-Cell of Figure 2.3.

multipoles are used for even more precise corrections of the particle trajectories. In the LHC correctors up to the tenth order (decapoles) are used to correct for those higher order field errors. The main bending magnets and quadrupoles are equipped with sextupoles, octupoles and decapoles, schematically shown in Figure 2.3 for one LHC FoDo-Cell. In Table 2.2 the magnets shown in Figure 2.3 and their functionality are summarized.

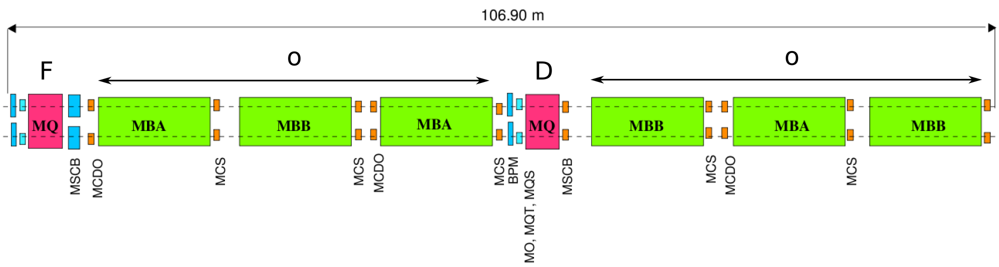

Figure 2.3: LHC FoDo-Cell, showing schematically how the main dipoles are equipped with higher order correctors. For the description of the magnets see Table 2.2 [8].

The chromaticity arises form the false focussing of the quadrupoles due to the momentum deviation of the particles in comparison to the design momentum. The effect is analogue to that one in the optical equivalent of a quadrupole - a lens. Particles with lower momentum are stronger focused than particles with higher momentum. It is convenient to perform the compensation at points where the particles are naturally sorted according to their momentum, namely anywhere where the dispersion is non-zero. Here the particles travel along dispersive trajectories depending on their momenta. Sextupoles are used for the correction, since they have a focusing strength depending on the transverse beam position ($k \propto x$) [13].

For higher order multipole fields the strength in one plane depends on the beam position in the other, which leads to coupling between the betatron oscillations in the two planes and hence to coupled resonances as given in Equation 2.7. Coupling must be avoided, since it is much easier to correct the two planes separately, rather than to take care of the second plane while applying corrections to the first one.

2.2.3 Closed Orbit Correctors

The Closed Orbit Dipoles (COD) are dipole magnets used to correct the closed orbit at LHC. They are individually powered magnets. Each dipole pair consists of a horizontal (vertical dipole field) and a vertical (horizontal dipole field) orbit corrector to apply corrections in both planes separately. The vertical corrector is realised by rotating the horizontal one by 90°.

Taken beam 1 as reference, every horizontal COD is placed at the every focussing main quadrupole. Correspondingly, every vertical COD is placed at every defocussing main quadrupole. Therefore, the horizontal (vertical) correctors are separated by almost 90° phase advance. The reason for this placement can be understood by considering the equation of the closed orbit distortion (x) when a single dipole kick (x') is performed:

$$x(s) = x'(s_0)\frac{\sqrt{\beta(s_0)\beta(s)}}{2\sin(\pi Q)}\cos(|\phi(s)-\phi(s_0)|-\pi Q) \tag{2.8}$$

This equation depends on the β-function at the location of the kick, $\beta(s_0)$. The β-function has a maximum at the focussing quadrupoles, hence the effect of the kick is enhanced at this position and, consequently, the strenght of the dipoles can be relax. The dipole correctors in LHC work at a maximum current of 60 A.

Figure 2.4 shows a difference orbit (top) of beam 1 with respect to a reference, as it is monitored in the control room. It was measured by the beam position monitors (see Chapter 2.3.2) directly after the injection of a pilot bunch. The used reference orbit is optimized for the current collimator settings in the machine and can be loaded from the database. The middle plot indicates a possible correction to achieve the reference, calculated with ten corrector magnet. The bottom plot displays how the orbit would look like after this correction is applied. The correction algorithm tries to obtain the reference orbit, therefore the bottom plot should be a zero orbit for a perfect correction.

2.2.4 Cryogenics and Superconductivity

Under nominal conditions the LHC stores protons with an energy of 7 TeV. By considering Equation 2.4 again, one can easily determine that the strength of the magnetic field necessary to keep this protons on a circular orbit with a bending radius of around 2800 m is $B \approx 8.3\,\mathrm{T}$. With normal conducting magnets only a maximum field strength of around 2 T can be reached. It poses a great challenge to techniques and material to reach such high field strengths. Superconducting magnets are required, since the magnetic field strength B is proportional to the current I in the coils. Hence, the energy is limited by the magnetic field strength or rather by the intensity of current

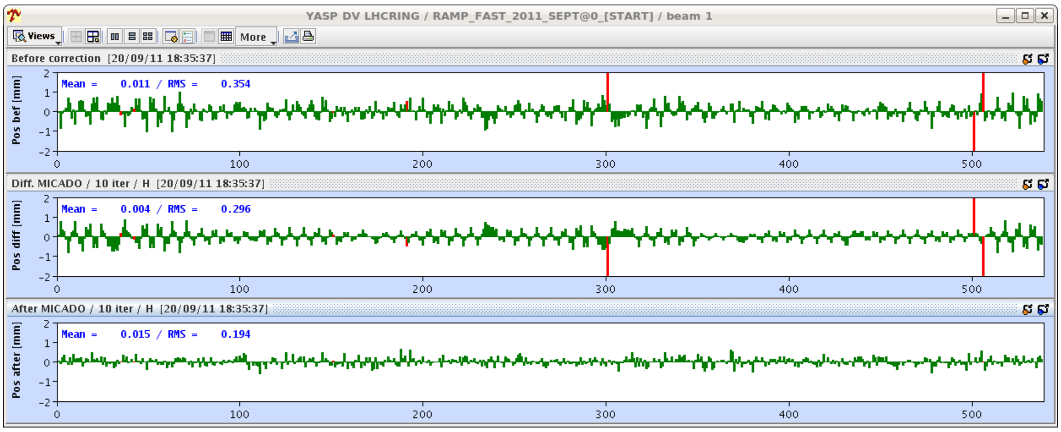

Figure 2.4: A beam 1 horizontal orbit in LHC (top) with respect to a standard reference orbit. The middle plot gives a correction calculated with ten orbit corrector dipoles. The bottom plot shows the orbit after applying the correction in the middle.

the material can tolerate.

Due to the high requirements of the LHC magnets, e.g. absolute homogeneous dipole fields and withstand extreme high currents in the coils, special techniques are used to build the superconducting cables installed in the coils of the magnets and in the connections between them. They are comprised of many fine filaments of niobium-titanium (NbTi) alloy embedded in a copper matrix. NbTi was chosen, because it becomes superconducting, i.e. its electrical resistance becomes practically zero, under a critical temperature of 9.2 K. The copper has two functions: In the superconducting stage it acts as an insulator, since now its resistance is much higher than that of NbTi. However, if it comes to a quench, i.e. the material leaves the superconducting regime, the resistance of NbTi becomes much higher than that of copper and the copper can temporarily bridge the arising resistance.

These conductors show a greater stability and less diamagnetism in comparison to ordinary single filament conductors. Consequently, the linearity of the magnetic field and the magnet current is greatly improved. The magnetic field of magnets built with this technique can also be risen and discharged more rapidly [14].

In general, such kind of magnets can be operated at temperatures above 4.2 K (boiling temperature of liquid helium), but when they are cooled down further higher fields can be achieved. In LHC the operation temperature is set to 1.9 K, since at that temperature also the helium, which is used as cooling material, shows additional properties: it is superfluid and behaves as a Non-Newtonian fluid; it can flow through narrow gaps or capillaries without any viscous dissipation; it also has unusually high thermal conductivity. These properties are very important for the cooling and to maintain the superconductivity of the magnets at all times. A perfect heat exchange between the material and the cooling system is necessary to prevent for undesired quenches, since already small energy deposits of around 10 mW/cm^3 (corresponding to a change in temperature of $\Delta T = 2\,\mathrm{K}$) can lead to one. During a quench, the magnet generates high internal voltages and locally elevated temperatures. These cause electrical and mechanical stresses in the windings. Permanent damage to the magnet can occur.

2.2.5 Radio Frequency Cavities

To accelerate the particles superconducting high frequency cavities are used. Per beam two times four cavities are installed in interaction region 4, see Figure 2.1. A maximal voltage per beam of 8 MV at 450 GeV and of 16 MV at 7 TeV is reached at the RF-frequency of 400 MHz [8]. To maintain an optimal phase focussing this strength is not fully exploited. The energy gain per turn is only 485 keV, since the working point of the cavities is not set to the maximum amplitude of the high-frequency, rather to the trailing edge. In that way high momentum particles gain less energy, because they show a slightly larger orbit radius with respect to the design particle and hence they arrive later at the accelerating cavity. For low momentum particles it happens exactly the other way around. Thus a longitudinal focussing is ensured.

2.2.6 Collimator System

Over the entire length of the accelerator 54 collimators per beam are installed which build a passive security system. The collimators are used to absorb particles which are deflected from the reference orbit and thus protect the beam pipe and the magnets from unwanted impacts of these particles. If those particles would be absorbed by the magnets they could trigger a quench. Two main interaction points are used to reject particles with too large momentum (IP3) and amplitude deviation (IP7). Further collimators are installed in front of the experiments and at the ends of the transfer lines. They are made of special plates consisting of graphite and tungsten. The most important factor in the choice of the material was that the collimators have to be very heat resistant, since they are meant to accumulate mislead particles to protect the other machine elements. The assembly is made of two shoes, each 1.6 m long, in the vacuum chamber which can be synchronously moved closer to the beam. In that way it is possible to absorb 99.9 % of the dangerous particles before they are able to hit the walls and magnets [8].

2.2.7 Beam Dump

After about 10 hours of stable beams the luminosity has decreased so much that the beams need to be renewed. Therefore, a controlled dumping of the beams into the so-called beam dump must be triggered. The beams are deflected out of the beam pipe by extraction kickers in point 6 (Figure 2.1) and lead to a 750 m long drift section which ends in a 7 m long and 70×70 cm width, water cooled and steel coated graphite bloc. This bloc is additionally surrounded by $\sim$ 900 t of radiation shielding blocs. At the moment the proton beam arrives at this structure its kinetic energy is transformed into heat energy while a temperature of 800°C is reached [8].

2.3 Measurement Devices for Beam Dynamics

A save and stable operation of such a huge accelerator implies that the beams are always under control. During a run several beam parameters, like intensity, transverse position, tune and beam size, are under constant review to be able to monitor the beam behaviour and to apply corrections, if necessary. This is important for the optimisation and safety of the machine but also to provide the experiments with the highest luminosity possible.

To obtain the necessary information from the beam, several different devices for beam diagnostics and instrumentation are needed. Due to the complexity of the LHC not all instruments can be discussed in the scope of this thesis, but the ones used to collect the data analysed here will be examined in the following.

2.3.1 Fast Beam Current Transformer (FBCT)

The beam current is one of the most important quantities for the operation of a particle accelerator. It is one of the first parameter to be checked for the accelerator functionality and to prevent for particle losses.

Many different devices can be used for this purpose, but for a continuous measurement of the beam current during operation a non-destructive device is needed. The LHC uses a measurement method based on the detection of the magnetic field carried by the beam, a so-called current transformer.

The Fast Beam Current Transformers (FBCTs) are capable of performing bunch-by-bunch measurements by integrating the charge of each LHC bunch. But they can also provide information about the total turn-by-turn beam intensity. For redundancy, two fast transformers with totally separated acquisition chains are placed in each ring located in IR4. Moreover, each beam dump line is equipped with two redundant FBCTs, using the same acquisition electronics, for monitoring the ejected beams.

The beam consist of N particles with charge qe; these particles travel around the ring, thus they can be regarded as a current

$$I_{beam} = \frac{qeN}{t} \tag{2.9}$$

Like a current-carrying wire, the beam produces a magnetic field B as displayed in Figure 2.5 which can be calculated according to the Bio-Savart law (1820). Due to the cylindrical symmetry of the beam, only the azimuthal component has to be considered. Now the beam current can be determined by monitoring this accompanied magnetic field with a current transformer shown in Figure 2.6.

The beam passes as the "primary winding" ($N_{prim} = 1$) of the transformer through a highly permeable torus. An insulated wire wound around the torus is acting as the "secondary winding" (N_{sec}). For a bunched beam it appears as this first winding

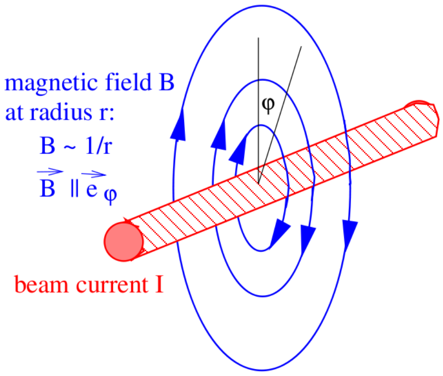

Figure 2.5: Scheme of the magnetic field lines created by a current [15].

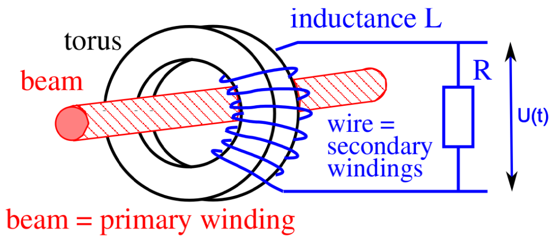

Figure 2.6: Scheme of a current transformer measuring the accompanied magnetic field of the beam [15].

carries a varying current $I_{beam} = I_{prim}$, which creates a varying magnetic flux in the transformer's core (the torus) and thus a varying magnetic field in the secondary winding. This varying magnetic field, on the other hand, produces a varying current in the secondary winding I_{sec}. This effect is called mutual induction.

For an ideal current transformer the relation between the primary current I_{prim} (which is given by the beam current) and the secondary current I_{sec} (which is induced in the secondary winding due to the varying current in the primary one) is given by

$$I_{prim} \cdot N_{prim} = N_{sec} \cdot I_{sec} \implies I_{sec} = \frac{1}{N} \cdot I_{beam} \tag{2.10}$$

since $N_{prim} = 1$ and for reasons of simplification $N_{sec} = N$ is set for the number of windings around the torus. In practice it is preferred to measure a voltage rather than a current, therefore the resistance R is introduced. Now the induced current in the wire around the torus (which builds a coil with the inductance L) is measured by the voltage drop over the resistance R with the usage of Ohm's Law (1827):

$$U = R \cdot I_{sec} = \frac{R}{N} \cdot I_{beam} \tag{2.11}$$

By replacing I_{sec} with Equation 2.10 the beam current (beam intensity) is obtained.

However, the formulas used above only apply to an ideal transformer, in reality one has to take into account several corrections to obtain a good approximation of the beam intensity. For instance the torus, the capacitance between the windings, an additional resistance caused by the windings itself and the cabling need to be considered additionally.

This scheme only works for pulsed beams, since for very small frequencies ($\omega \to 0$) the transformer can not handle the dc-currents. In that case the inductance L acts as a short circuit for the considered low frequencies and no signal can be recorded through the resistor [15].

However, with this technique very low currents and thus very low intensities can be measured. Furthermore, due to the fact that the torus only detects the azimuthal field component the signal is nearly independent of the displacement of the beam from the central orbit.

2.3.2 Beam Position Monitor (BPM)

A Beam Position Monitor (BPM) is a non-destructive diagnostic instrument with which the position of the beam in the beam pipe can be measured. In the daily operation of an accelerator it is very important to know the position of the beam to check and correct for position offsets, since these lead to wrong deflections of the particles by the magnets.

The general idea of such a device is to measure the charges induced by the electric field of the beam particles on an insulated metal plate, as sketched in Figure 2.7.

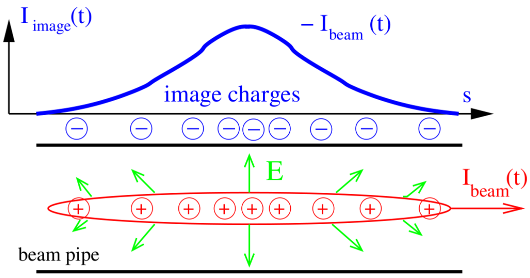

Figure 2.7: Scheme of the beam current inducing a wall current of the same magnitude but opposite sign [15].

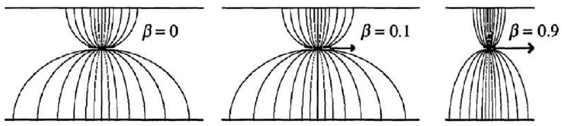

Figure 2.8: Scheme of the transverse components of the electromagnetic field produced by a charged particle in the laboratory frame with increasing velocity up to the relativistic case from left to right [15].

As the Figure shows the beam induces a wall current of the same magnitude but reversed polarity in the walls of the beam pipe. The beam only induces a current in the walls (and hence in the plates of the BPM) at the moment of its passage, therefore an alternating current (AC) signal is seen on the plates. The wall current and the signal has the same time behaviour as the beam passing by, as can be seen by considering the electromagnetic field as generated by the charged particle beam in its rest frame. If one transforms this field $E_{rest}(t')$ at time t' via Lorentz transformation into the laboratory frame $E_{lab}(t)$ at time t, the transverse field component $E_{\perp,lab}(t)$ increases by the Lorentz factor $\gamma = 1/\sqrt{1-\beta^2}$ compared to the value within the beam's rest frame $E_{\perp,rest}(t')$:

$$E_{\perp,lab}(t) = \gamma \cdot E_{\perp,rest}(t') \tag{2.12}$$

as shown in Figure 2.8. The field lines move closer together as the velocity increases, hence for a high relativistic particle beam the electric and magnetic field vectors can be approximated as perpendicular to the propagating direction. This is the behaviour of a so-called Transverse Electric and Magnetic (TEM) field distribution.

A button pick-up is composed of four pick-up plates installed crosswise at the beam pipe wall. If the beam comes closer to one of those plates, the image current in that plate is higher than in the opposite one, this is called the "proximity effect". Hence, opposite plates will give different signals. The LHC BPMs system process the data with a technique called "the wide band normaliser" [16], it makes use of the pick-up signals directly and uses delay lines for the normalisation function.

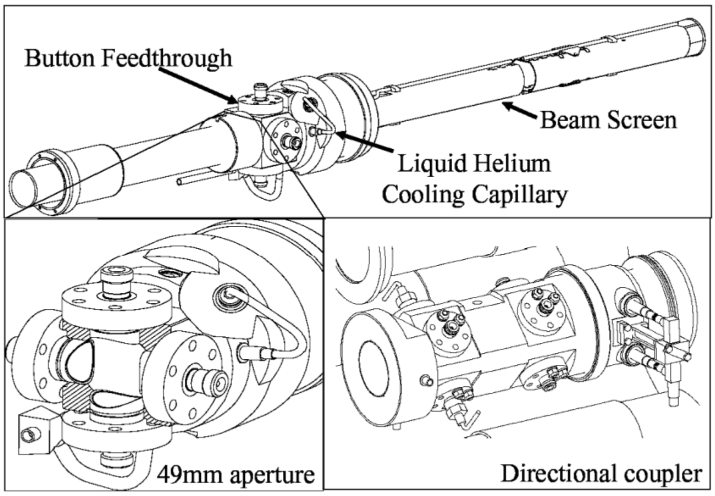

Figure 2.9: Top: BPM body used in the LHC arcs. Bottom left: Zoom of the electrodes. Bottom right: Directional coupler (strip-line BPM) used near the interaction points [18].

In the LHC there are 516 monitors per ring to measure the beam position, all measuring in both horizontal and vertical plane. The majority of the monitors (912) installed in the tunnel are 24 mm diameter button BPMs. They are installed in the arc quadrupoles and mounted orthogonally in a 48 mm inner diameter beam pipe close to the orbit dipole correctors. The electrodes are curved to follow the beam pipe aperture and are retracted by 0.5 mm to protect the buttons from direct synchrotron radiation from the main bending magnets. The remaining BPMs are enlarged (34 mm or 40 mm) button electrode BPMs, mainly for the stand-alone quadrupoles, or strip-line electrode BPMs, used either for their directivity in the common beam pipe regions or for their higher signal level in the large diameter vacuum chambers around the dump lines [17]. Figure 2.9 shows a schematic view of each type. The length of the strip-line coupler has been designed in order to provide the same shape of the signal as that from the button electrodes.

The BPMs have different acquisition modes. The resolution in orbit mode with a single pilot bunch is around 5μm [18]. During 2011 a new acquisition mode was commissioned for the BPM system, the orbit bunch-by-bunch, in order to study the beam-beam orbit effects. Results about the linearity and resolution of this mode are given in Section 4.2.2.

2.3.3 Wire Scanner

A wire scanner is an instrument used to determine the transversal beam size. It consists of a thin wire which is moved across the beam. By doing so, the beam interacts with the wire material and a signal can be obtained, either if the secondary emission current (SEM) is extracted from the wire, or if the flux of high-energy secondary particles downstream of the wire is detected.

If a particle passes through matter its mean energy loss is described by the Bethe-Bloch formula [19]

$$-\left\langle \frac{dE}{dx} \right\rangle = 4\pi N_A r_e^2 m_e c^2 \cdot \frac{Z_t}{A_t}\rho \cdot \frac{Z_p^2}{\beta}\left[ln\frac{2m_e c^2\gamma^2\beta^2}{I} - \beta^2 \right] \tag{2.13}$$

with the constants: N_A the Avogadro number, m_e and r_e the mass and classical radius of an electron and c the velocity of light. The target parameters are: ρ density of the target with nuclear mass A_t and nuclear charge Z_t, I is the mean ionization potential of the target. The projectile parameters are: Z_p nuclear charge of the ion with velocity β and $\gamma = (1-\beta^2)^{-1/2}$. The lost energy will be deposited in the wire material leading to ionization and atomic or collective excitation. The liberated electrons can be measured as a current in the wire. This method of measuring the secondary emission current is mainly used for low energy protons and heavy ions.

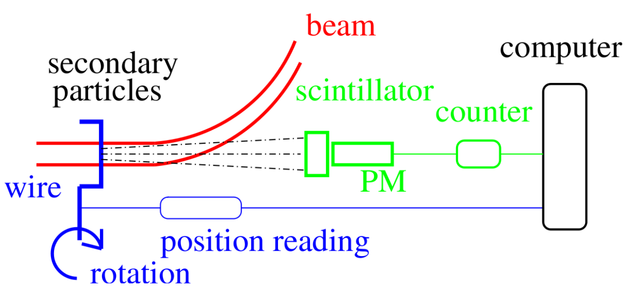

Figure 2.10: Scheme of a wire scanner using the production of secondary particles as a signal source, [15].

In most cases, for beam energies lager than the threshold for π-meson production ($\approx$ 150 MeV) the signal is obtained by monitoring the secondary particles outside of the beam pipe, see Figure 2.10. This secondaries might be hadrons created by the interaction of the projectile particle with the wire material, which have enough kinetic energy to leave the beam pipe. Several meters downstream of the device a detector, e.g.

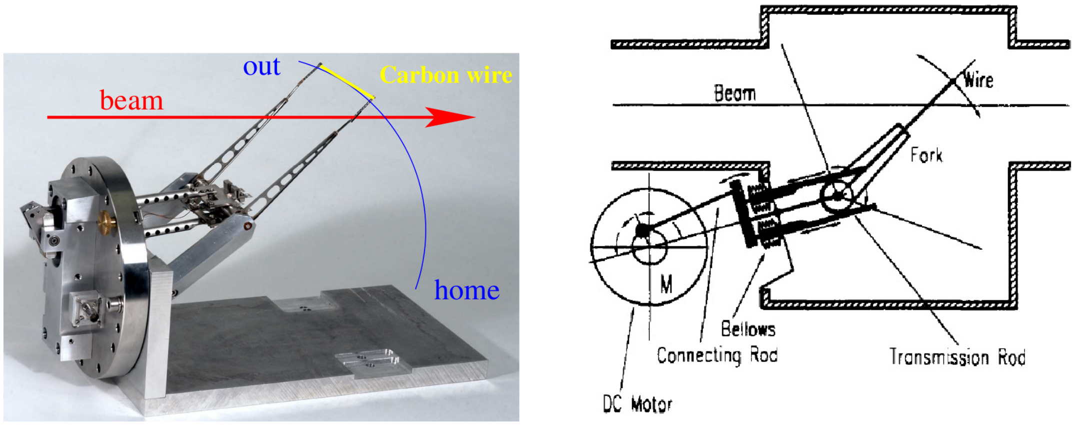

Figure 2.11: Left: Foto of a wire scanner used at CERN [15]. Right: Scheme of the wire scanner position inside the beam pipe [20].

a scintillator, is installed to measure the arriving secondaries. By plotting the count-rate of the detector against the wire position a representation of the beam profile is obtained [15].

In Figure 2.11 such a device is shown. This particular one will measure the vertical beam size, since it is passing the beam from the bottom (its parking position, home) to the top (out position). A scanner measuring the horizontal beam size would be installed at one side of the beam pipe, rotated by 90° compared to this one.

Since a wire has to pass the beam, this is a destructive instrument. However, due the material choice of carbon or SiC, which are light and have a low nuclear charge Z, and the low thickness of the wire, which can be down to 10 μm, the disturbance of the beam is very small. Moreover, the material must be very heat resistant, because high beam intensities are scanned, which can lead to high temperatures in the wire. Its scanning velocity can reach 10 m/s [15]. The wire scanners of LHC have 30 μm carbon wire moving at 1 m/s.

The scanners can not be used in the operation with many bunches and at high energies because of two reasons: the wire material can only withstand a certain amount of energy deposition before it breaks and secondly due to the produced secondary particles the first downstream magnet will reach its quench limit during a scan. The wire scanners can therefore only be used for the cross calibration of other emittance measurement devices, like the beam synchrotron monitor (BSRT, see Chapter 2.3.4) for protons and rest gas ionisation monitor for ions, or for less bunches and at injection energy. Nevertheless, the wire scanners have been extensively used from an early stage to monitor the beam size and calculate its emittance. For more information see [17].

Their ideal position would be at the same location as other emittance monitors. However, the BSRTs are installed directly upstream the D3 magnet (which is one of the magnets used to separate the beams in the interaction region) in IR4 to make use of its deflection of the beam for extracting the synchrotron light. If the wire scanners

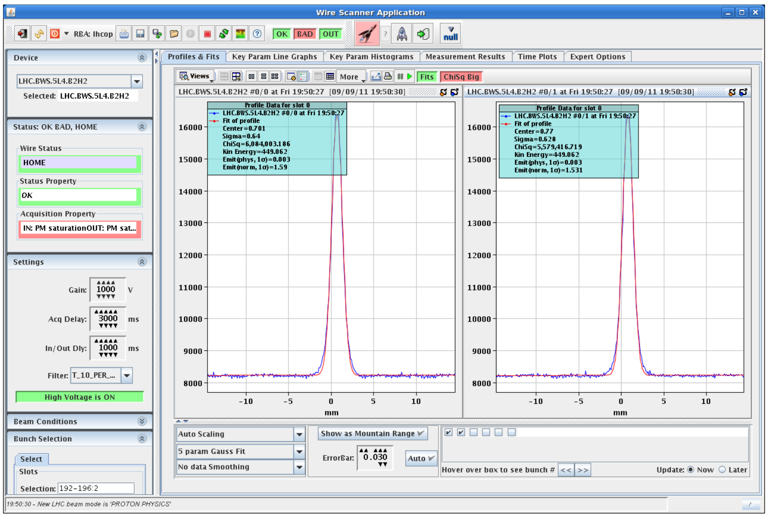

Figure 2.12: Beam profile of beam 2 measured by the wire scanner as it is displayed in the LHC control room. The left graph shows the measurement while moving the wire in; on the right side the measurement while moving out (home) is shown.

would be installed here, the risk of quenching D3 would be non-negligible, thus they have been placed directly downstream this magnet ([8] Chapter 13).

Eight linear wire scanners are installed in the LHC. Each beam is equipped with two wire scanners in both horizontal and vertical planes. One is available for operation and the other one intended as a fully functional back-up. Acquisition is possible in two different modes: the standard mode and the bunch-by-bunch mode. Figure 2.12 shows the LHC beam 2 horizontal profile measured by the wire scanner.

2.3.4 Beam Synchrotron Radiation Telescope (BSRT)

The Beam Synchrotron Radiation Telescope (BSRT) provides a non-destructive and continuous measurement of the beam sizes in the transversal plane using the synchrotron light, which is produced by the beams, when they are bent in a dipole magnet. The photons are emitted in a cone with an opening angle of $2/\gamma$, where $\gamma = E/m$ is the Lorentz factor, in forward direction (in the laboratory frame). As the beam energy increases, the cone becomes more and more narrow. The energy emitted in synchrotron light is proportional to the inverse of the forth power of the particle mass. This means that electron beams radiate $(m_p/m_e)^4 = 10^{13}$ times more than proton beams at the same energy, and in fact this radiation is an issue for electron accelerators [21].

At LHC the protons are injected at 450 GeV, ramped up to 7 TeV and brought into collisions. In principle a normal operating dipole can be used as synchrotron light source, but since the energy range from injection to flat top is very big, the spectrum of the light emitted in superconducting dipoles strongly changes with increasing energy.

The BSRT is built to measure light in the visible range and the radiation emitted

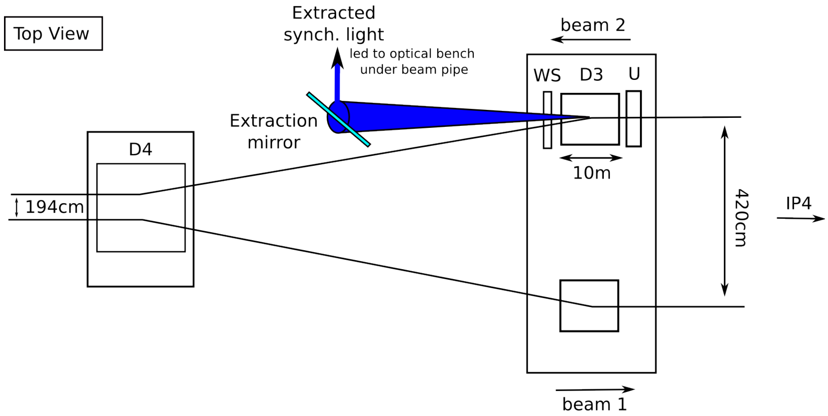

Figure 2.13: BSRT position in the ring and synchrotron light extraction, schematic [22].

in normal superconducting bending magnets is not sufficient to image the beam below 2 TeV [22]. The device is located in IR 4 as shown in Figure 2.13. Therefore, the D3 dipole magnet, one of the four dipoles responsible for widen the separation of the beams at the RF cavities, is used by the BSRT as the main light source above 2 TeV.

In order to measure a beam profile below this energy an additional magnet has been installed just before D3. This magnet is a superconducting undulator (5 T magnetic field) with four alternating magnetic poles that produce alternating regions with upwards and downwards magnetic field. This excite the particles to oscillate in the region of the magnet but has no effect on average, i.e. particles leave the magnet without any change in direction, whether the magnet is switched on or not. The spectrum of the emitted synchrotron light is dominated by the interference effects arising from the periodic structure of the magnet. It is designed in a way that the beam will emit light in the visible range at proton energies at which the emitted radiation from the D3 magnet can not be used.

With this setup the light of the undulator passes into the UV by around 1 TeV, but from this point on the edge radiation of D3 can already be used for imaging the beam. For higher energies up to 7 TeV the center radiation of D3 is used [22], [23], [24].

Since the photons are emitted in the direction of motion of the particles the two beams must be separated to extract the light beam without interfering the protons. This is done by the magnetic field of the D3 magnet, it deflects the protons, but the photons stay on a straight trajectory. Due to the large circumference of the LHC of about 26.7 km the bending angle of one dipole is very small, e.g. for D3 the bending angle is 1.58 mrad. To be able to extract the light from the proton beam the extraction mirror must be located about 30 m behind the magnet to not interfere with the beam, see Figure 2.13.

The extraction mirror leads the light to an optical system below the beam pipe which is installed on a vibration-damped optical bench. The optical system is shown in Figure 2.14. As explained above the light sources change during observation, therefore the

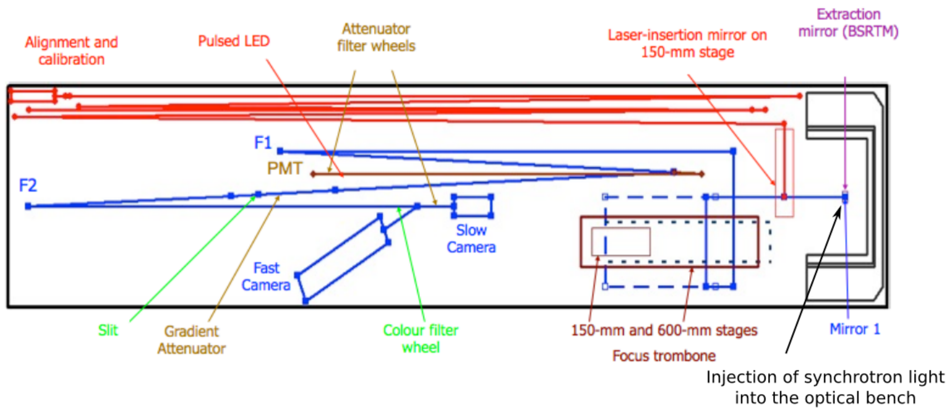

Figure 2.14: BSRT optical system below the LHC beam pipe, schematic [25].

focus must be changed as well when changing the light source. The optical system is equipped with translation stages which allows to vary the focal length remotely, i.e. the focus can be moved from the center of the undulator to some distance inside the D3 magnet in order to obtain a sharp image.

The total amount of radiation is split between the Abort Gap Monitor (PMT in Figure 2.14) and the two camaras attributive to transverse profiles. The device can either measure an average over the whole beam or bunch-by-bunch. However, in the bunch-by-bunch mode it is only possible to measure one bunch after the other, which leads to long periods when measuring all bunches in the beam [25].

For further optimisation of the image optical filters for color and density are applied. The horizontal and vertical beam sizes are obtained by asymmetric Gaussian fits to the image, using a common peak but different widths to either side. The smaller width is used to define the measured beam size [21], [23], [24], [25], [26].

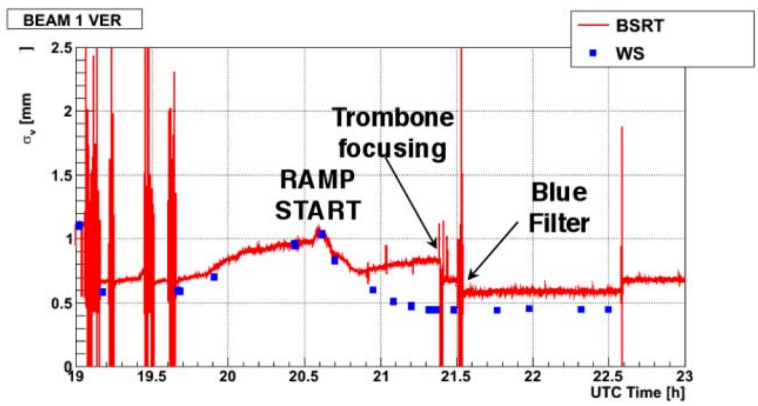

Figure 2.15: A continuous measurement of the beam 1 vertical size throughout the LHC energy ramp to 3.5 TeV. Wire scanner measurements are seen as squares [17].

As already mentioned in the previous section, the BSRT has to be calibrated with the wire scanners. Figure 2.15 shows a comparison of the beam size as measured continuously by the synchrotron light monitor (red) and periodically by the wire scanner (blue) during an LHC energy ramp to 3.5 TeV. There is good agreement between the measurements during the injection plateau and the early part of the ramp, where the focus is on the undulator radiation. As the energy rises, the increase in edge radiation from the separation dipole blurs the image, leading to a measured beam size larger than that given by the wire scanners. Adjusting the focussing trombone recovers some of the image quality, which is further improved by addition of a blue filter. Further fine tuning will be necessary to reach the 3-5% error level predicted by calculations for the vertical plane [17].

The discrepancy of the BSRT measurement in comparison with the wire scanners after the blue filter is applied, has to be corrected with special correction factors. The use of those factors, calculated by a BSRT expert, is explained in Chapter 3.3.2.

2.3.5 Schottky Pick-Up

A Schottky detector system is able to perform a non-destructive and precise measurement of several beam parameters, like revolution frequency, momentum distribution, tune, transverse emittance and chromaticity. Such devices use the so-called Schottky noise to obtain a frequency spectrum from which the mentioned parameter can be calculated. Schottky noise is produced by statistical fluctuations which a current, created by a finite number of charge carriers, always shows.

To understand the origin of Schottky noise and how the measured signal has to be interpreted, a single particle with charge qe travelling in a storage ring with a revolution frequence f_0 is considered first.

This particle will pass a detector once per turn and will therefore only create a signal at the time of its passage, shown in Figure 2.16 top for m turns. The Fourier transformation of this current is a line spectrum with peaks at all harmonics of the revolution frequency f_0, see Figure 2.16 bottom. Since a real detector is only able to measure positive frequencies the negative ones coming out of the Fourier transformation are folded to the positive side of the spectrum. Moreover, all delta-peaks of the transformation have a finite hight for a real beam and real equipment.

A second particle with a slightly different revolution frequency $f_1 = f_0 + \Delta f$ creates a peak in the spectrum at f_1 with a distance Δf to f_0, the frequency of the first particle. With an increasing harmonic number h the distance between the two frequencies will increase as $h \cdot \Delta f$.

For a coasting (debunched) beam with N particles randomly distributed along the storage ring, each with a slightly different revolution frequency, the signal will show current fluctuations ΔI when plotting against time (Schottky noise). In the frequency spectrum the lines for a single particle evolve into frequency bands with a finite width, which corresponds to the spread in the revolution frequency. As seen in the case of

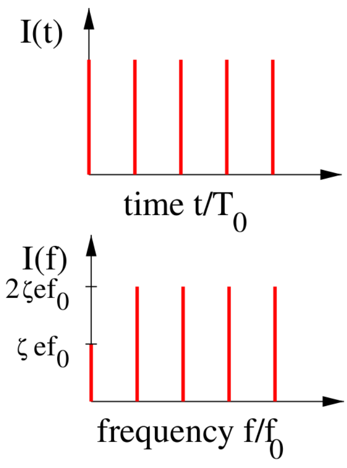

Figure 2.16: Single particle time domain signal and line frequency spectrum in a storage ring [15].

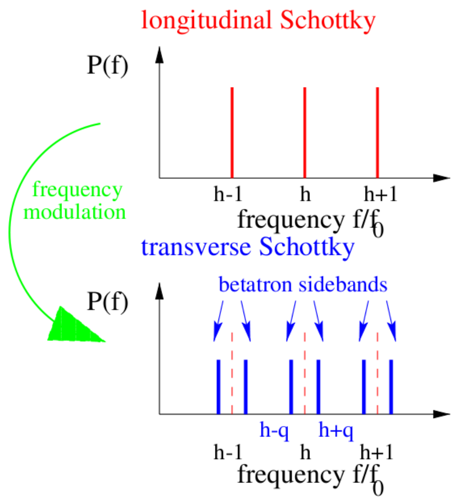

Figure 2.17: Sidebands (blue) appearing around the center longitudinal Schottky signal (red) due to transversal betatron oscillation [15].

only two particles, the width of the bands increases with the harmonic number, but since the total power within a band is constant, the hight must decreases.

Furthermore, the coasting beam also shows a transversal oscillation around the reference orbit, the so-called betatron oscillation. With a position-sensitive pick-up one is able to obtain the transverse position from the difference signal of opposite electrodes, like it is done for a Beam Position Monitor (BPM). The output signal of such a pick-up has two contributions, one corresponds to the already seen longitudinal Schottky signal, the other one appears as a frequency modulation of this signal caused by the transversal betatron oscillation. It can be calculated that this will cause sidebands with the maximum located at

$$\Delta f_h^{\pm} = (h \pm q) \cdot f_0 \tag{2.14}$$

for a fixed harmonic number, see Figure 2.17. From this position the non-integer part of the tune q can be calculated via

$$q = \frac{f_h^{+} - f_h^{-}}{2 f_0} \tag{2.15}$$

The appearance of two mirroring sidebands, again arise from the definition of the frequency range of the Fourier transformation ($-\infty$ to $+\infty$), in a real detector only positive frequencies can be measured.

This gives an easy measurement of the incoherent value of the tune without influencing the beam. However, with this formalism one implies that the non-integer part of the tune is smaller than 0.5. But without any additional information one can not tell if q is above or below 0.5.

From the width of the sidebands the chromaticity can be determined. While the width is given by

$$\Delta f_h^{\pm} = \Delta f_0(h \pm q) \pm \Delta q f_0 \tag{2.16}$$

inserting the formula for the frequency dispersion $\eta = \frac{1}{\gamma_{tr}^2} - \frac{1}{\gamma^2}$ (where $\alpha = \frac{1}{\gamma_{tr}^2}$ is the momentum compaction factor) and the chromaticity $\xi = \frac{\Delta p}{p} / \frac{\Delta Q}{Q}$ (where p is the momentum and Q is the tune of the particles), that leads to

$$\Delta f_h^{+} = \eta \tfrac{\Delta p}{p} \cdot f_0 \left(h + q - \tfrac{\xi}{\eta} Q \right) \quad \text{upper sideband} \tag{2.17}$$

$$\Delta f_h^{-} = \eta \tfrac{\Delta p}{p} \cdot f_0 \left(h - q + \tfrac{\xi}{\eta} Q \right) \quad \text{lower sideband} \tag{2.18}$$

It can be seen, that the widths of the two sidebands are not equal. To obtain the chromaticity the other parameters $\frac{\Delta p}{p}$, η and q has to be measured independently.

As mentioned above the width is also related to the frequency spread and thus to the momentum spread. Equation 2.17 and 2.18 gives

$$\frac{\Delta p}{p} = \frac{1}{\eta} \frac{\Delta f_h^{+} + \Delta f_h^{-}}{2 h f_0} \tag{2.19}$$

When also the amplitude of the sidebands A are taken into account, the emittance can be calculated via

$$\epsilon \propto A_h^{+} f_h^{+} + A_h^{-} f_h^{-} \tag{2.20}$$

For bunched beams each bunch can oscillate longitudinally inside its bucket. This motion is called synchrotron oscillation and causes additional sidebands to each harmonic line $h \cdot f_0$ (center of the Schottky bands), since it modifies the time the particles are passing through the detector. From the distance between the maxima the synchrotron frequency can be determined. If betatron motion is present, the betatron sidebands are modulated due to synchrotron oscillation as well. This causes a quite complex spectrum [15], [21].

In the LHC a 4.8 GHz slotted waveguide structure Schottky pick-up, schematically shown in Figure 2.18, is used. It has an aperture of 60×60 mm and is 1.5 m long. A gated, triple down-mixing scheme is used to baseband the successive filtering from bandwidth of 100 MHz to 11 kHz. This device is capable of bunch-by-bunch measurements [27]. Four pick-ups are installed near point 4 in a normal conducting straight section, one per plane and beam. The transversal sensitivity is designed to peak at 4.8 GHz, since this is a multiple integer number of the 40 MHz revolution frequency of the 25 ns bunch spacing under nominal conditions [28]. Figure 2.19 shows an example of a Schottky spectrum measured with the LHC monitors.

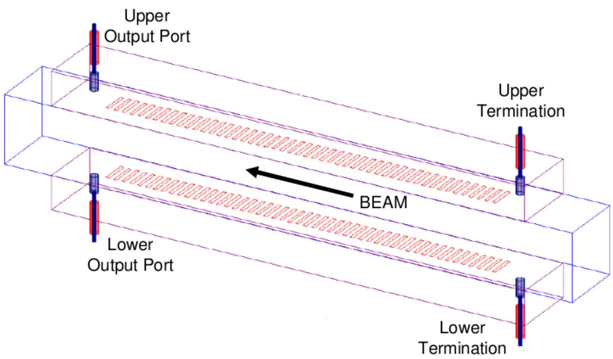

Figure 2.18: Scheme of the slotted waveguide structure for the LHC Schottky pick-up [28].

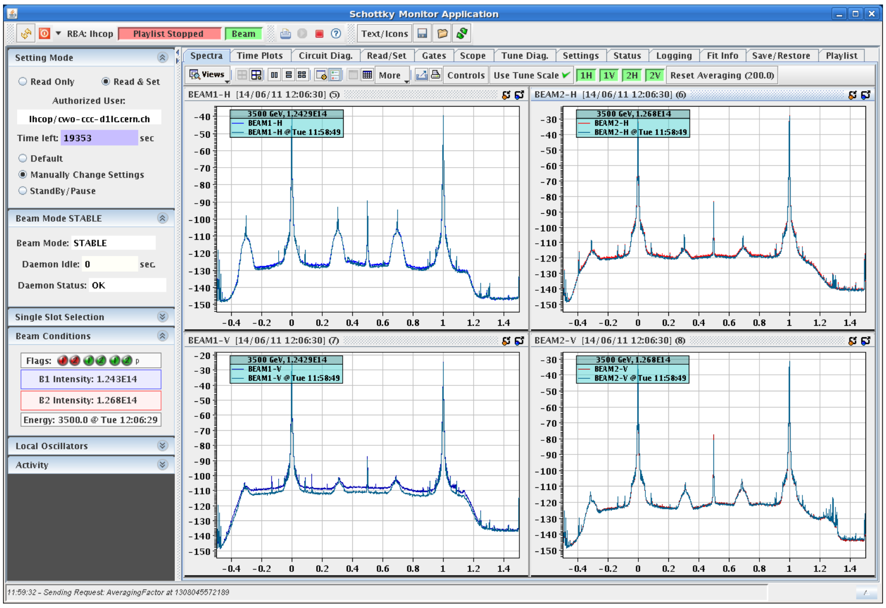

Figure 2.19: Schottky spectrum measured with the LHC Schottky pick-ups. Two small peaks directly to both sides of the revolution frequency peak (middle) are the sidebands used to determine the tune. Left: beam 1, right: beam 2, top: horizontal, bottom: vertical.

2.3.6 Machine Luminosity Monitors (BRAN)

The aim of the machine luminosity monitors [29], namely Beam RAte of Neutrals (BRAN), is to measure the interaction rates for the setup, the optimization and the equalization of the beams at the interaction regions. These instruments are required to measure the interaction rate with a good relative accuracy; the absolute value can be obtained with frequent cross calibrations against the luminosity monitors installed in the experiments. The calibration factor must remain stable over a reasonable amount of time and must not be influenced by the machine parameters (steering, optics etc.) The main error component from the BRAN detectors is expected to be the background. The requirements on the accuracy go from around 10% for the beam finding mode to 0.25% for the luminosity optimization phase. The integration time per scan point is inversely proportional to the luminosity for a given error. In order to detect and correct eventual bunch-by-bunch effects the bunch-by-bunch luminosity measurement is required. The detectors, readout and acquisition systems must thus be capable of operating with a useful bandwidth of 40 MHz.

The machine luminosity monitors are installed in the TAN absorbers 141 m away on either side of IP1 and IP5; and 113 m away on either side of IP2 and IP8. The monitors measure the flux of the showers generated by the neutral particles created in the collisions (neutrons and photons). Neutral particles are chosen in order to suppress the background related to beam losses. An schematic layout of the IP can be seen in Figure 2.20.

The radiation dose to the detectors is very large, 170 MGy/yr, and poses a constraint on the choice of the technology. For the high luminosity experiments (ALTAS and CMS) the monitors are radiation hard ionization chambers developed at LBNL (Lawrence Berkeley National Laboratory). The other interaction points have Cadmium Telluride (CdTe) detectors which are CERN responsibility. The CdTe detectors can easily comply with the 40 MHz bandwith, which is not the case for the ionization chambers, but they can only stand the radiation doses foreseen at ALICE and LHCb [30].

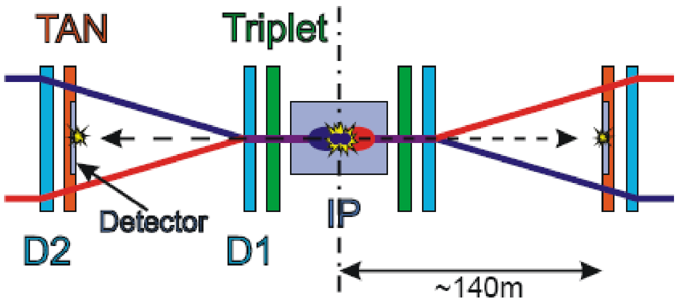

Figure 2.20: Layout of a high luminosity IP in LHC with the BRAN detectors placed at the copper absorber called TAN (orange rectangle) [30].

3 Linear Coherent Beam-Beam Parameter

In a particle collider like the LHC it is desirable to have colliding beams to provide the experiments with a high luminosity. But bringing the beams into collisions leads to additional effects which influences the stability and lifetime of the beam. These beam-beam effects can be one of the most important limiting factors in a collider, therefore they must be studied in detail.

However, a well defined limit like in lepton colliders [2] does not exist for hadron machines like the LHC, but possible indications for a limiting head-on beam-beam effect may be [31]:

- Slow emittance increase
- Beam losses and bad lifetime
- Coherent beam-beam oscillations

To find the optimal strategy for the LHC luminosity upgrade it is important to know, if the limiting factors are the head-on or long-range interactions.

In this chapter the linear coherent beam-beam parameter is calculated from the data of dedicated machine studies which took place during specific machine development (MD) periods.

This parameter is very useful as it is an estimation of the maximum linear coherent tune shift due to beam-beam interactions in the head-on case. It can give and approximation of the strength of the beam-beam interactions in single collisions and can be superimposed to get an estimation if more collisions per turn are present. However, it does not reflect the non-linearity of the beam-beam force and can therefore only be used as a scaling parameter in the linear regime for beam separations smaller than one in terms of beam size σ, which only applies to the head-on case.

The most important effect head-on collisions introduce is a change in tune (see Chapter 1.2). In LHC, with two colliding proton beams, the tune shift is negative. As a result the tune is decreased and moved in the tune diagram, with possible crossing of resonances, which can cause particle losses and lifetime problems. If the effect is too large, a tune scan must be performed to find a more optimal tune on which the beams are stable again.

For the incoherent case this parameter is derived from the kick a beam exerts to a single particle in the opposite beam as shown in Chapter 1.2. However, in daily operation two bunches are colliding, those are an ensemble of about 1.1×10^{11} particles.

In this case each particle is affected by the opposite beam, but they are also acting as an entity and build coherent behaviour which overlays the single particle effects. Thus, it is impossible to measure single particle effects, only coherent effects can be measured and the equation of the linear coherent beam-beam parameter has to be used for the calculations:

$$\Xi_{i,X,Y} = \frac{N_j \cdot r_{0,i} \cdot \beta^*_{i,X,Y}}{4\pi \cdot \gamma_i \cdot \sigma_{j,X,Y}(\sigma_{j,X} + \sigma_{j,Y})} \tag{3.1}$$

where X, Y are the barycentres in the horizontal or vertical plane of beam $i, j = 1, 2$ respectively. In this notation it easy to see which contribution the opposite beam has to the determination of the tune shift, i.e. if the linear tune shift Ξ_i is calculated for beam i, beam j acts as a electromagnetic lens, which is described by its intensity N_j and its transversal beam sizes at the interaction point $\sigma_{j,X,Y}$. Whereas beam i consists of particles with the classical particle radius $r_{0,i}$ with a relativistic gamma γ_i and a β-function at the interaction point of β^*_i. If one transforms the beam size into normalized emittance ϵ_N via

$$\sigma = \sqrt{\epsilon \cdot \beta} = \sqrt{\frac{\epsilon_N}{\gamma}\beta} \tag{3.2}$$

a dependency on the β-function, β^*_j, and energy, γ_j, of the second beam appears. In the special case of LHC both beams consist of the same sort of particles, namely protons, which are stored at the same energy $\gamma_1 = \gamma_2$. Moreover, the β-functions at the interactions points are equal in both planes and for both beams $\beta^*_{1,x} = \beta^*_{1,y} = \beta^*_{2,x} = \beta^*_{2,y}$, therefore Equation 3.1 simplifies to

$$\Xi_{i,X,Y} = \frac{N_j \cdot r_0}{4\pi} \cdot \frac{1}{\sqrt{\epsilon_{N_{j,X,Y}}}(\sqrt{\epsilon_{N_{j,X}}} + \sqrt{\epsilon_{N_{j,Y}}})} \tag{3.3}$$

The dependency on the particle energy cancels in the notation of Equation 3.3, when the beam size is expressed in normalized emittance ϵ_N. Now Ξ only depends on the intensity and emittance of the crossed beam.

3.1 Nominal and Current Operational Situation

For the nominal LHC a filling pattern with 2808 bunches spaced by 25 ns at an energy of 7 TeV is foreseen. The bunches consist of 1.15×10^{11} particles and a transversal normalized emittance of 3.75 μm rad [8].

Currently the LHC is running at 3.5 TeV with twice the distance between bunches (50 ns), which leads to a maximum number of 1380 bunches, this is less than half of the nominal number, because the injection scheme had to be modified to satisfy the required smaller number of collisions in ALICE and LHCb. However, it is possible to get more brilliant beams for normal operation and the nominal values for intensity and emittance are already exceeded by more than 20 %. Bunch-by-bunch emittances of 2.0 μm rad and intensities of 1.3×10^{11} particles can be reached. Consequently, the linear beam-beam parameter is higher than the one expected under nominal conditions. A comparison between parameters used in the current operation and the nominal ones is given in Table 3.1.

Parameter	nominal	operation
Energy	7 TeV	3.5 TeV
Intensity N	1.15×10^{11}/bunch	1.3×10^{11}/bunch
Normalized Emittance	3.75 μm rad	2.0 μm rad
$\beta_x^* \cdot \beta_y^*$ (in IP1 & 5)	0.55 m $\cdot$ 0.55 m	1.5 m $\cdot$ 1.5 m
Crossing angle	285 μrad	240 μrad
Incoh. BB parameter (ξ)	0.0037	0.0079
Coh. BB parameter (Ξ)	0.0018	0.0040

Table 3.1: Nominal [8] and operational LHC parameters. The linear beam-beam parameter Ξ is calculated for one collision.

3.2 Experimental Conditions

To achieve an estimation of the linear coherent tune shift introduced by beam-beam interactions one needs to look at isolated head-on collisions only. If long-range interactions are present they introduce additional effects, e.g. orbit kicks, changing the overlapping cross-section of the colliding bunches, leading to a separation of the barycentres at which the beam-beam force changes according to Equation 1.13 and Figure 1.3 in Chapter 1.2. On the other hand, this leads to a decrease of the direct head-on tune shift, because it is described by the derivative of the beam-beam force, which has its maximum at zero amplitude. Consequently, the maximal effect introduced by head-on interactions would not be measured as desired. Furthermore, the measurement would be mixed up with a tune shift due to long-range interactions, which show a different behaviour.

This means that an experiment must be performed where the machine is filled with very few bunches without any parasitic encounters. In the simplest case this can be done with two single colliding bunches. During the experiment it is important to monitor the emittances, intensities and lifetimes of the bunches. Also the tunes have to be recorded to have a direct measurement of the tune shift.

This was done in two MD sessions where bunches with different intensities and emittances were studied at injection energy (450 GeV) under different collision schemes. As seen before, those are the important parameters to change, since the linear tune shift is only depending on the intensity and the emittance of the crossed beam. Due to energy independence of the effect, it is convenient from an operational point of view to perform the experiment at low energy.

Below a short sketch of the beam specification and experiments in the two MD periods are given.

MD 06/05/2011 - Fill 1765 & 1766

The first MD to study the head-on beam-beam limit was done on the 6^{th} of May 2011 during the fills 1765 and 1766. In each fill several injections were done, from which two per fill were suitable to extract data. The filling and collision patterns can be found in Table 3.2 where also the initial values of the intensity and emittances per bunch are noted. Out of four injections three were done with one bunch per beam and one with two bunches per beam. It was foreseen to go up to four bunches per beam, but due to the high intensities used, the save beam limit for this MD period was exceeded and the fill had to be dumped.

More information also to other issues of this MD can be found in the MD-note [31].

MD 30/06/2011 - Fill 1911

In the second MD it was desired to study bunches with operational emittances around $2\,\mu$m rad, but higher intensities of around 2×10^{11} particles, which is almost twice the nominal value. Only one fill was done in this experiment, details on the filling scheme and initial conditions are as well listed in Table 3.2.

In this fill orbit scans were done to investigate the effect of the kick one beam gives to the opposite one due to beam-beam interactions. The detailed analysis of this data is done in Chapter 4. Two scans were performed in the separation plane of IP1 and 5 respectively, after those a tune scan was accomplished.

The MD-note for this experiment can be found in [32] together with the notes for the long-range MD.

In the following, the data analysis of the second MD session which was done at the 30^{th} June 2011 will be explained. Later on, the results will be compared with other MDs and normal operation.

3.3 Analysis of MD Data from 30/06/2011

In normal operation with several bunches it is necessary to have a pilot bunch with low intensity in bucket 0 to set up the machine before it is filled with high intensities. In this MD the pilot bunch was over-injected with a high intensity bunch, to have only one bunch per beam circulating in the machine. This eases the interpretation of the data.

		Bucket/slot	Collisions	at IP	initial N	initial $\epsilon_{N,x}$	initial $\epsilon_{N,y}$
Fill 1765a	B1	1001/100	2	1, 5	1.65×10^{11}	$1.2\,\mu$m	$1.0\,\mu$m
	B2	1001/100	2	1, 5	1.50×10^{11}	$1.2\,\mu$m	$1.2\,\mu$m
Fill 1765b	B1	1001/100	3	1, 2, 5	1.85×10^{11}	$1.2\,\mu$m	$1.0\,\mu$m
		18851/1885	1	8	1.80×10^{11}	$1.2\,\mu$m	$1.0\,\mu$m
	B2	1001/100	2	1, 5	1.65×10^{11}	$1.2\,\mu$m	$1.2\,\mu$m
		9911/991	2	2, 8	1.70×10^{11}	$1.2\,\mu$m	$1.2\,\mu$m
Fill 1766a	B1, B2	dumped, due to violation of the save beam limit					
Fill 1766b	B1	1001/100	2	1, 5	1.85×10^{11}	$1.2\,\mu$m	$1.0\,\mu$m
	B2	1001/100	2	1, 5	1.70×10^{11}	$1.2\,\mu$m	$0.9\,\mu$m
Fill 1766c	B1	1001/100	2	1, 5	1.85×10^{11}	$1.1\,\mu$m	$1.0\,\mu$m
	B2	1001/100	2	1, 5	1.65×10^{11}	$1.2\,\mu$m	$1.2\,\mu$m
Fill 1911	B1	0/0	2	1, 5	2.20×10^{11}	$1.8\,\mu$m	$1.9\,\mu$m
	B2	0/0	2	1, 5	2.45×10^{11}	$1.8\,\mu$m	$1.8\,\mu$m

Table 3.2: Filling and collision schemes of the two beam-beam head-on limit MDs, additionally the initial intensities N and normalised emittances ϵ_N of all bunches are noted. The statistical uncertainty on the emittance measurement is $0.08\,\mu$m rad and on the intensity measurement 10^9 protons per bunch.

3.3.1 Observations

As mentioned above, to calculate the linear coherent beam-beam parameter Ξ the bunch-by-bunch intensities and emittances are required. An evolution in time over the whole fill can be found in Figure 3.1, here only the losses in intensity are displayed. In Figure 3.1 every experiment done with the beams is marked in order to understand why the emittance is blowing up or the losses are rising. The lifetime is plotted in Figure 3.2. Plots showing the tunes measured by the BBQs and Schottkys can be found in Figure 3.5 and 3.6, respectively.

At $t_0 = 0$ the two bunches were brought into collisions, which affected the emittance of beam 2 only slightly, while a small beam blow up in beam 1 is visible. Nevertheless, the beams started to loose particles and after 20 minutes already 20% of the beams were lost. This can also be seen in the lifetime, it dropped from over 100 hours to only one hour at the moment of the first collisions, after a few minutes the beams stabilised and the lifetime went up again.

The first orbit scan in ATLAS can be followed up by looking at the lifetime and particle losses. At the beginning of the scan the slop of the losses increased, when the beams were brought back to the head-on position it came back to its previous value. Considering the lifetime, a clear minimum is visible for the duration of the scan, but when large separations of around $700\,\mu$m were reached, the lifetime increases again. This could be originated from two effects: due to the separation the beams exert kicks

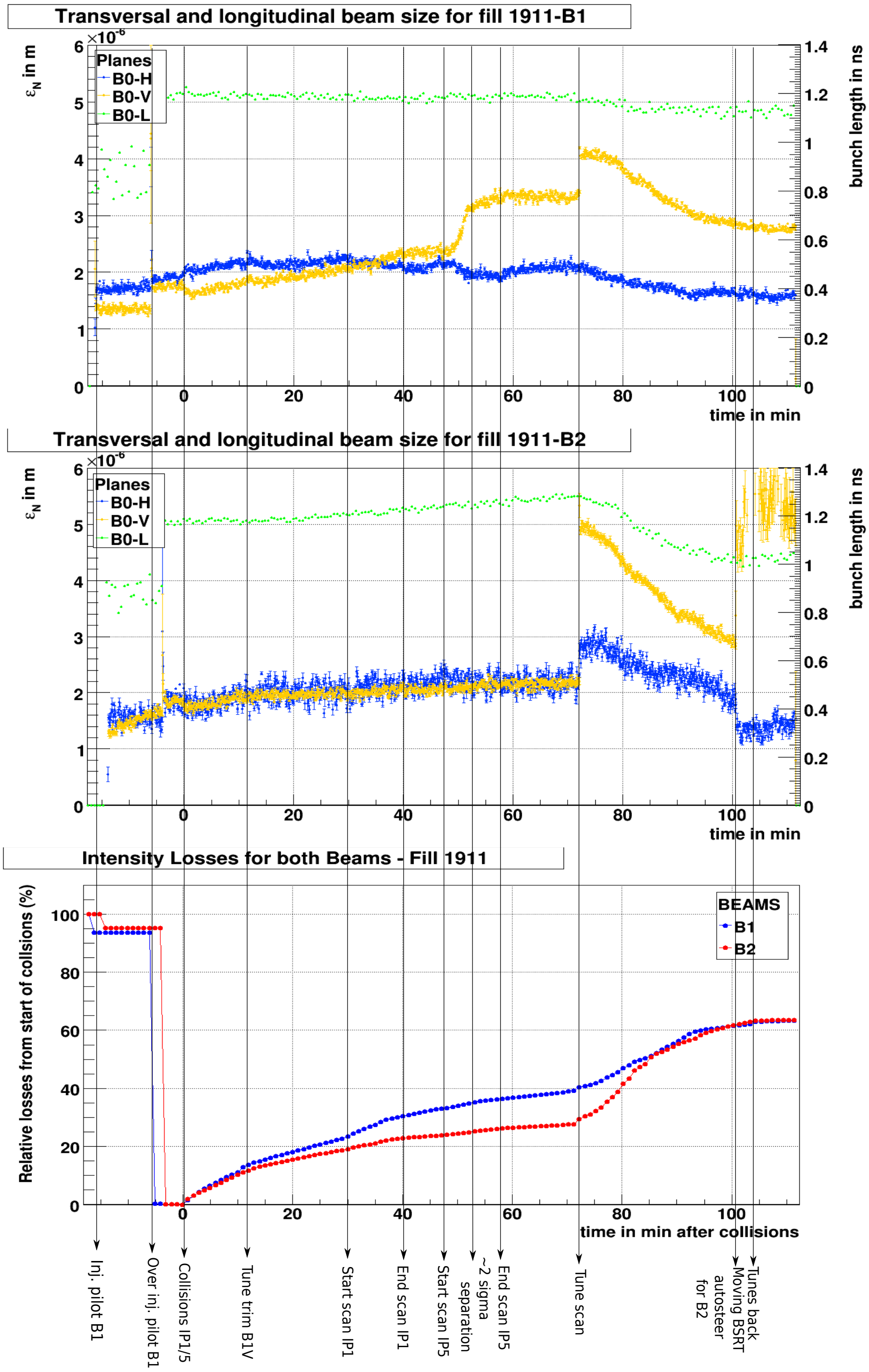

Figure 3.1: Top and middle: Evolution in time of the normalized emittance (horizontal blue, vertical yellow) and the longitudinal bunch length (green) for beam 1 and 2 during Fill 1911. Measurement from the BSRTs corrected with the correction factors given in Table 3.3, error bars show the statistic fluctuations of the BSRTs over 5 seconds. Bottom: Intensity losses during the Fill for both bunches.

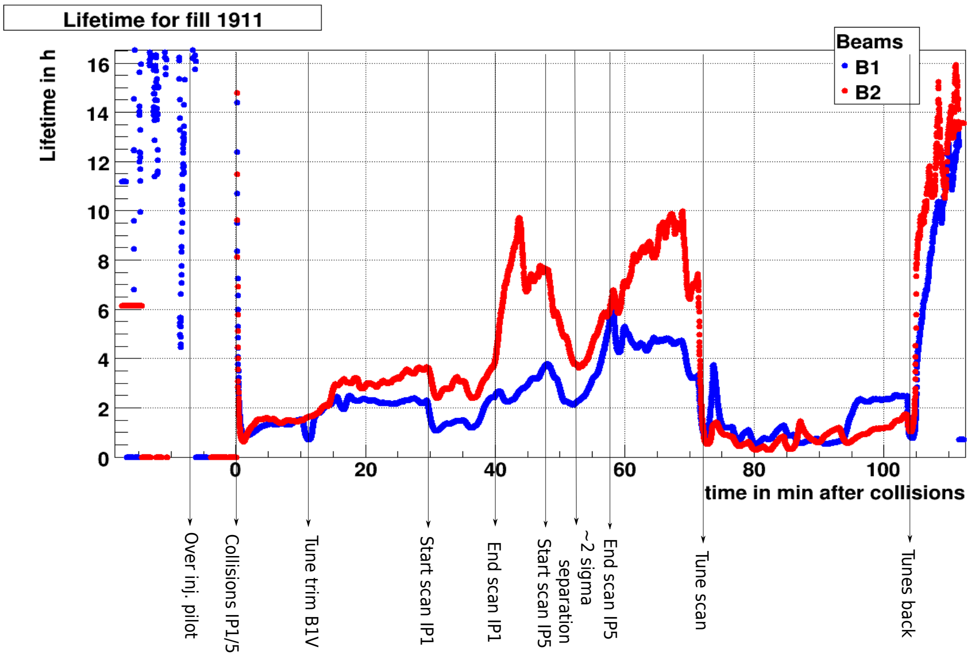

Figure 3.2: Lifetime of the beams as a function of time for beam 1 (blue) and beam 2 (red).

to each other as explained in Chapter 1.2 which vary with the separation, hence, also at a fixed step in the scan, high amplitude particles feel a different force compared to particles at smaller amplitudes. As a result, particles populating the outer regions of the bunch get lost earlier decreasing the intensity at the beginning of the scan and they are already gone in the further course. Furthermore, as shown in Figure 1.3 in Chapter 1.2 the beam-beam force rises until around two in terms of beam size, for larger amplitudes it reduces. This distance corresponds to the stage in the performed scan at which the lifetime improves.

The scan in CMS was done faster and at around 400 μm separation a significant beam blow up in the vertical plane of beam one was observed, which also had a clear effect on the lifetime. The beams stabilised again, but the following tune scan had a major influence on the beam: fast emittance growth and losses were witnessed accompanied by a characteristic decay in lifetime. Putting the tunes back to the original values brought the beams back to their stable conditions.

3.3.2 Absolute Value of the Emittance

The determination of the absolute value of the emittance is difficult, since it is influenced by some errors which are not easy to quantify.

The errors shown in the emittance plot of Figure 3.1 arise from the statistical fluctuations of the BSRTs over a period of 5 seconds.

Due to the assembly of the BSRTs, the measured beam size has a systematic offset which changes with energy. This uncertainty must be cross-calibrated by using the wire scanners as a reference. Out of this calibration the correction factors shown in Table 3.3 are calculated especially for this fill.

	B1H	B1V	B2H	B2V
$\sigma_{correction}$	0.55	0.55	0.71	1.1

Table 3.3: BSRT correction factors for MD2 provided by a BSRT expert.

The corrections must be applied like

$$\sigma_{BSRT} = \sqrt{\sigma^2_{measure} - \sigma^2_{correction}} \tag{3.4}$$

For further information about the performance and sources of uncertainties of the BSRT see [33].

By using Equation 3.2 the corrected beam size σ_{BSRT} is transformed into normalized emittance ϵ_N, which is shown in the plot.

To determine the emittance the value of the β-function at the position of the beam size measurement must be known. For different energies different magnets (undulator and D3) are used to produce the synchrotron light, therefore one needs to apply the β-function for the magnet used at the current energy, since here the measured synchrotron light is produced and the beam size at this location is measured by the BSRTs. The β-functions have been determined by measuring the beta-beating at certain locations in the ring. Those values have been propagated through the lattice to obtain values for each element. On the other hand, the MADX program [34] can be used to model the β-functions for a linear machine. Measurements at the undulator and D3 magnet for 450 GeV and 3.5 TeV are shown in Table 3.4.

	β_x [m]	σ_{β_x} [m]	$\beta_{x,model}$ [m]	β_y [m]	σ_{β_y} [m]	$\beta_{y,model}$ [m]
450 GeV (Undulator)						
B1	162.51	7.43	178.82	173.97	3.33	191.70
B2	130.06	30.46	127.66	417.57	22.11	332.61
3.5 TeV (D3 Magnet)						
B1	173.02	13.30	172.97	194.75	2.02	214.60
B2	129.97	7.32	127.09	371.66	9.65	334.61

Table 3.4: β-functions for the calculation of the emittance from the BSRT beam sizes. For 450 GeV four values for the β-function of the undulator are listed, since the device is split into four magnets, the given value in this table is a mean over those four.

It can be seen that the errors of the β-functions for beam 2 are larger than for beam 1, especially in the horizontal plane of beam 2, here the relative error is about 20 %.

Those errors contribute to the absolute value of the emittance are statistical uncertainties of the beta-beat measurements. Nevertheless, the considered statistical fluctuations of the beam size (and the intensity) arise from the resolution of the measurement device. Consequently, both error contributions have different sources and will be treated separately. It is important to be able to distinguish between them, since the weight of their contributions is not always the same, as it can be seen in Figure 3.3. Here the emittances of fill 1911 is shown again, but the statistical fluctuations of the beam size (error bars) are displayed separately from the error contribution of the β-function measurement (light blue and orange bands). For beam 1 the latter is in the same order of magnitude as the statistical ones, but beam 2 is strongly affected.

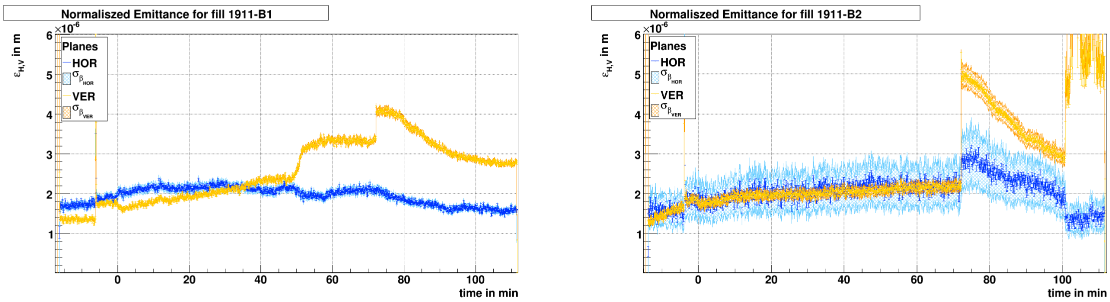

Figure 3.3: Evolution with time of the normalized emittances for fill 1911. The light blue and orange bands mark the uncertainty arising from the measurement error of the β-function at the undulator. Left: beam 1, right: beam 2.

This uncertainty propagates to the determination of the linear beam-beam parameter, since here the absolute value of the emittance is required. As a result the uncertainty on the calculated tune shift generates almost solely from the uncertainties on the measurement of the beam size and β-functions. Whereas, the measurement of the intensity shows small statistical fluctuations.

3.3.3 Linear Coherent Beam-Beam Parameter

Figure 3.4 shows the calculation of the linear coherent beam-beam parameter from Equation 3.3 as a function of time for both planes and both beams separately, where $t = 0$ marks the moment where the beams were brought into collisions in IP1 and 5.

The red band indicates the error contribution of the β-function measurement at the undulator and the black error bars arise from the statistical uncertainty of the beam size and the intensity measured by the BSRT and DCBCT (Direct Current Beam Current Transformer). As said before, the value for beam i is calculated from the properties of beam j $(i, j = 1, 2)$, therefore the contribution of the β-function error is the biggest for

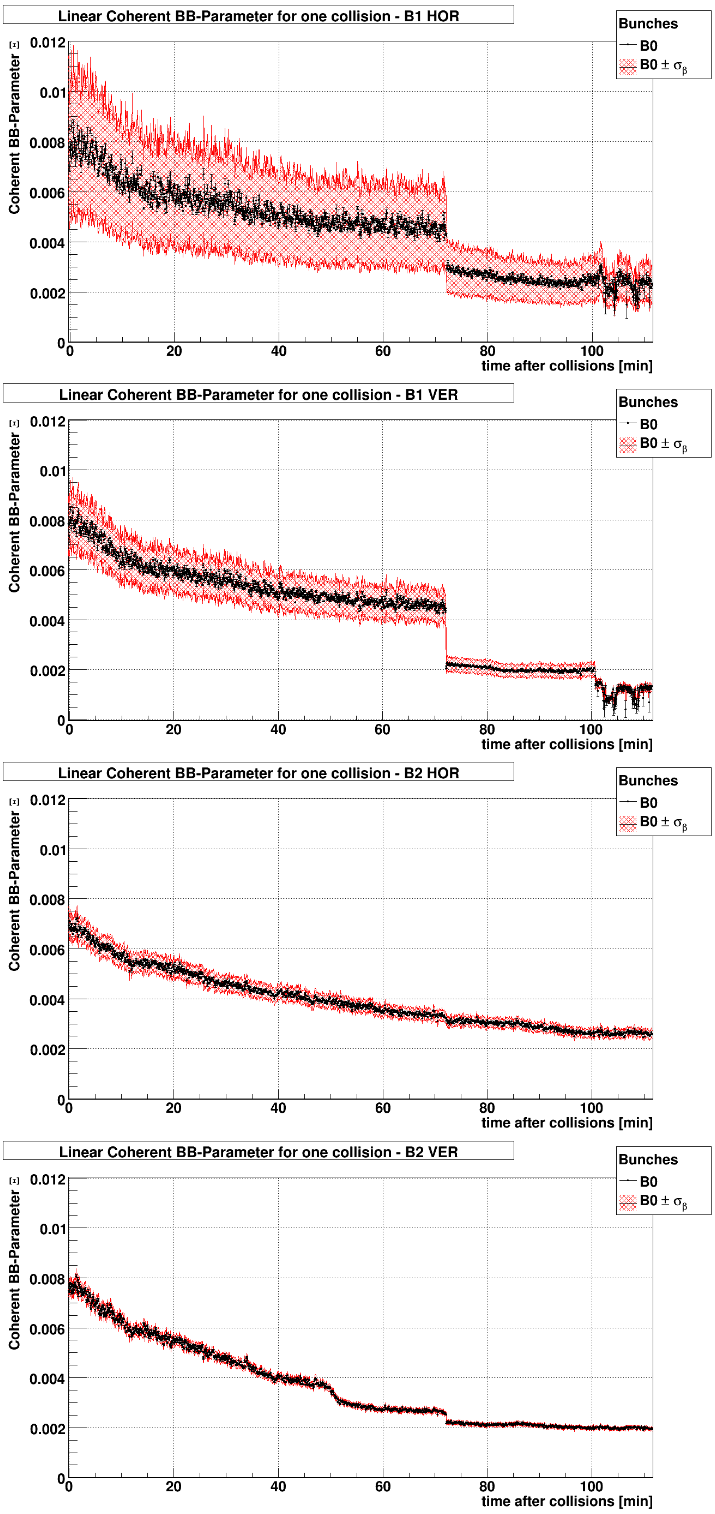

Figure 3.4: Linear coherent beam-beam parameter for a single collision for fill 1911 (second HO limit beam-beam MD) calculated from the data of the DCBCT and BSRT (black), the black error bars have their origin in the statistic fluctuations of the BSRT and DCBCT measurement. The red band indicates the error related to the measurement of the β-functions at the position of the BSRT.

the horizontal plane of beam 1, since the β-error from beam 2 horizontal and vertical is used in the calculation.

Table 3.5 summarizes the maximum values of Ξ which describe the tune shift directly after the beams where brought into collisions. They are obtained by a fit over the first two minutes after collisions.

Beam	Unit	Ξ_{HOR}	$\sigma_{\Xi_{HOR}}$	$\sigma_{\Xi_{HOR,syst}}$	Ξ_{VER}	$\sigma_{\Xi_{VER}}$	$\sigma_{\Xi_{VER,syst}}$
FBCT bunch-by-bunch data							
B1	$[10^{-3}]$	16.89	0.05	4.21	16.91	0.03	1.69
B2	$[10^{-3}]$	13.94	0.01	0.69	15.56	0.02	0.41
DCBCT beam data							
B1	$[10^{-3}]$	15.87	0.05	3.95	15.90	0.03	1.59
B2	$[10^{-3}]$	13.69	0.01	0.68	15.27	0.02	0.40

Table 3.5: Linear coherent beam-beam parameter for all planes and both beams for two collisions in IP1 and 5, obtained by fitting over the first two minutes after collisions.

The calculation was done two times with intensities measured by the FBCT (Fast Beam Current Transformer) and the DCBCT. In general, for all calculations done in this thesis the FBCT values are used, since it is the only device able to perform bunch-by-bunch measurements, which are always required. The DCBCT only measures the current of the whole beam. However, in the special case of the currently considered fill, where only one single bunch was circulating in the machine, the beam current can be seen as bunch-by-bunch current and the DCBCT can be used as well.

Typically the FBCT is calibrated with the DCBCT using the following formula:

$$N_{DCBCT} = \sum_{i=1}^{N_b} N_{FBCT,i} \tag{3.5}$$

where N_{DCBCT} is the beam intensity measured by the DCBCT and $N_{FBCT,i}$ the FBCT intensity for bunch i, N_b is the number of bunches per beam. In the case of one bunch per beam, the DCBCT beam measurement is therefore more reliable than bunch-by-bunch FBCT data. A comparison of both measurements for the current fill shows differences in the absolute value, but relative values are always consistent. And since the determination of the beam-beam parameter requires absolute values, the calculations are done with the data of both devices, as summarized in Table 3.5. The differences have the biggest influence in beam 1, because the variations in intensity of beam 2 (which is used to calculate Ξ_1) are the largest.

The plots show a decay with time which is related to the behaviour of the two initial parameters (emittance and intensity). It can be seen from Figure 3.1 that the emittances are blown up and the losses increase with time, consequently, as can easily be verified from Equation 3.3, Ξ must decrease.

The big jump at around minute 70 corresponds to a step in the performed tune scan, which hit a resonance and caused a huge beam blow up and fast losses in intensity. Beam 2 vertical also suffers from the emittance increase in the vertical plane of beam 1 provoked by the orbit scan in IP5.

The increase in emittance and the reduction of intensity with time implies that the beam-beam force decreases with time as well, i.e. the tune shift with respect to the initial tunes before collisions becomes smaller, what on the other hand shows that the beam-beam effect is maximal for high brilliant beams, small emittances and high intensities.

3.3.4 Tune Shift from Tune Measurements

During the fill the tunes were measured by the Schottkys (Figure 3.6) and the Base-Band Tune measurement system (BBQ, Figure 3.5). Unfortunately the measurements are very noisy.

The data taken by the BBQ is unsuitable for the calculation of the tune shift, as it is illustrated in Figure 3.5. It shows a big spread between single measurements as long as the transverse damper is on. Among other things, the damper is used to prevent for coherent oscillations, thus it excites the beam with a variable frequency which suppresses undesired oscillations. Unfortunately, this frequency is close to the tune and since the BBQ works on a peak finder basis it sometimes just finds the damper frequency instead of the tune.

Later, after the second orbit scan in IP5 the damper was switched off and the data immediately becomes practical. But at the moment were the beams were brought into interaction it is impossible to extract a value for the tune shift.

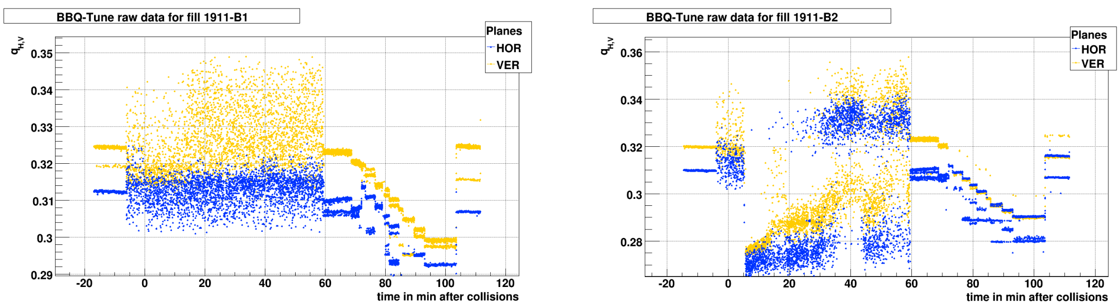

Figure 3.5: Evolution in time of the tunes measured by the BBQs (horizontal blue, vertical yellow) during fill 1911. Left: beam 1, right: beam 2.

In principle the Schottky monitor measures a noise signal arising from the Schottky noise of the moving particles. It uses the difference signal between two pick-ups to filter the coherent signal, which overlies the desired incoherent one. The device is not yet fully commissioned, so that it is sometimes difficult to obtain a clean signal. The biggest problem at the moment is, that if the two signals are phase shifted the weak incoherent spectrum is covered by the remaining parts of the more dominant coherent signal and it is not possible to get a good Schottky spectrum, from which the tunes can be determined. It is foreseen to install a new tool to provide a larger tolerance regime to adjust the signals to get a clear difference signal. To be able to take direct actions, if the measurements are bad, it will be possible to control the phase of the signal directly from the control room.

The data in Figure 3.6 demonstrates that in the current fill only the measurement for the horizontal plane of beam 1 is good enough to extract the desired tune shift at the moment of collisions.

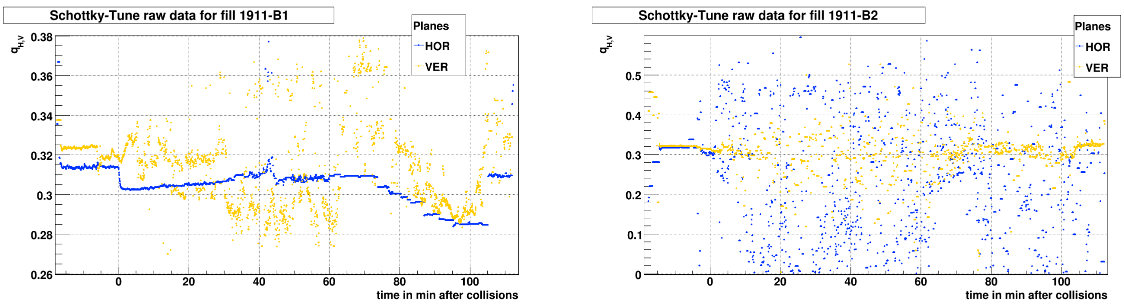

Figure 3.6: Evolution in time of the tunes measured by the Schottky monitors (horizontal blue, vertical yellow) during fill 1911. Only the measurement of beam 1 horizontal can be used for the comparison with the calculated linear beam-beam parameter, all other planes are too noisy to make a precise statement. Left: Beam 1, right: Beam 2.

To determine the tune shift from the Schottky tunes a straight line of the form $f(x) = p_0 \cdot x$ is fitted to the data before and after the beams were brought into collisions. The first fit is used as a reference value, from which the result of the second fit is subtracted to obtain the tune shift, as demonstrated on the left hand side of Figure 3.7. Moreover, the right plot in Figure 3.7 displays the measured tune with respect to the obtained reference value before collisions, as a function of time. The data shows as well the decay after the first maximum value at $t = 0$, observed in Figure 3.4 for the linear beam-beam parameter, as long as the tune is not changed on purpose.

A measured tune shift of 0.0112 is obtained with this method. Where the error to the mean values of the tunes before and in collisions achieved by the fit, are in the order of 10^{-5} (as indicated in the plot) - which is smaller than the resolution of the Schottky pick-ups of 10^{-4}.

However, the tune measured by the Schottkys is the incoherent one. According to Equation 1.24 the coherent tune shift should be half of the incoherent one, therefore, to be able to compare the measurement with the calculated tune shifts in Table 3.5, the Schottky measurement has to be divided by two. The two parameters are not in agreement, even, when taking the error of the β-function measurement into account.

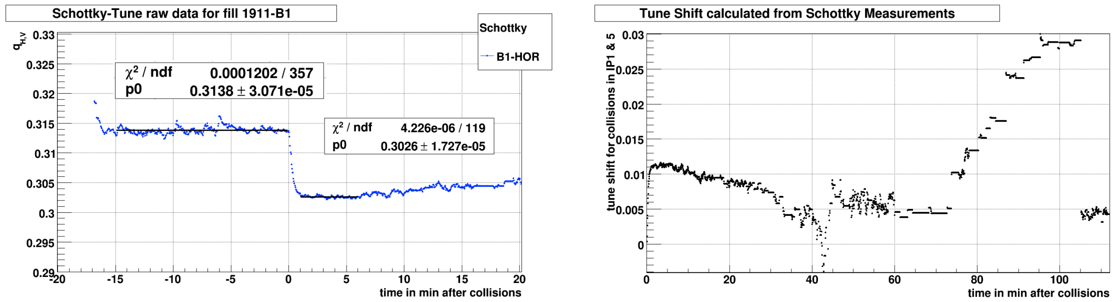

Figure 3.7: Determination of the tune shift for beam 1 horizontal measured by the Schottkys. Left: zoom to $t = 0$ (start collisions), fit for $t < 0$ and $t > 0$. Right: difference between the reference value (fit $t < 0$) and each data point in collisions.

Nevertheless, the tune values are obtained by a fit to the measured Schottky spectrum, whereas this fit is not always perfect and can lead to some fluctuations in the obtained tune. By closer investigation it was found that a slightly wrong scale was applied to the spectrum leading to a wrong determination of the tune. The error to the logged tune values, used in Figure 3.7, due to the wrong scale, is assumed to be in the order of 0.001, which is already in the order of the expected beam-beam effect. Unfortunately, the measured spectra of the MD were lost during the logging process by mistake and can not be reconstructed, only the tune values were saved and can be used for the analysis. Therefore, it is not possible to do any further investigation of the data. More measurements need to be done to compare data with theory. From the performed experiments it is not possible to give a reliable measured value of the tune shift. Nevertheless, a clear tune shift due to collisions is visible in the Schottky tune, just the amount can not be directly compared with the calculations.

3.3.5 Conclusion for Fill 1911

The linear beam-beam parameter is calculated for both beams in the horizontal and vertical plane, respectively, in Table 3.5. For the considered fill the FBCT was not well calibrated and showed discrepancies with respect to the DCBCT. Where the FBCT delivers higher intensities, leading to a higher values in the determination of Ξ. Nevertheless, only for the horizontal plane of beam one tune data was achievable, whereas this measurement is also not totally reliable due to some problems in the determination of the data, either. The tune measurement could not be investigated further, to find an explanation for the discrepancy with respect to the calculation, since the measured spectra were lost during the logging process and only the fitted tune values are saved.

Unfortunately, also for the other MDs the tune measurements were not sufficient to determine the tune shift due to collisions. To be able to compare the calculated tune shift, obtained by the linear beam-beam parameter, with a real tune measurement further studies are necessary. Until now, a comparison is not possible, due to a lack of data.

3.4 Analysis of Further Data

The same experiment as discussed in the previous chapter was done a second time for bunches with different emittances and intensities in fill 1765 and 1766. The obtained values for the linear coherent beam-beam parameter are listed in Table 3.6.

Contrary to fill 1911 in fill 1765a and 1766b/c the beams were brought into collisions in IP1 and 5 with a significant time difference, consequently the linear beam-beam parameter was calculated at two different times per fill. First when IP1 was collapsed ($t_0 = 0$) and secondly when the bumps in IP5 were closed ($t_1 > 0$). In the second case, the value obtained from the data was multiplied by two to reflect the overall tune shift, since now two collisions are present. This is the reason why the value at t_1 is bigger than at t_0, but it is not twice the amount, because in the meantime the bunches lost particles and blew up in emittance.

As it can be seen from Table 3.2 the initial conditions for both beams in fill 1765a, bunch 100 in fill 1765b beam 2 and beam 2 of fill 1766c are comparable, therefore they should exert similar forces to the opposite beam. The small discrepancies in the results arise from different reactions when the bunches were brought into collisions in the different IPs. For fill 1765a a beam blow up to around 2.2 μm was observed when collisions started in ATLAS, whereas the beams were only slightly affected by the collisions in CMS. For bunch 100 of fill 1765b a similar behaviour was observed. In both cases the vertical plane suffered more, consequently the calculated parameter becomes smaller in that plane compared to the horizontal one. But after the first blow up the growth rate of the horizontal plane was faster in all cases, hence the beam-beam effect became less important in the horizontal plane when collisions started in IP5. The effect on fill 1766c is larger, because the bunches were relatively stable in interactions and did not experience a significant blow up nor great losses.

As well bunch 100 of beam 1 in fill 1765b, fill 1766b and beam 1 of fill 1766c had comparable initial parameters. For beam 1 of the first fill a similar behaviour as for beam 2 is observed: beam blow up mainly in the vertical plane and drastic increase in losses due to collisions in IP1, collisions in IP5 bring no significant changes.

In case of fill 1766b, the vertical emittance was the smallest when the bunches were brought into collisions in the first IP, which also does not seem to affect the emittance growth and intensity losses significantly. Nevertheless during luminosity optimization a great emittance blow up was seen in the vertical plane. In the horizontal plane the increase was smaller. It was suggested that this blow up was caused by small amplitude (core) particles of the beam being close to the 10th order resonances. Significant losses have not been observed. Due to the large emittances when collisions started in IP5, the beam-beam tune shift is smaller for two collisions than for one.

Fill 1766c shows a stable behaviour when the beams are brought into collisions, while the horizontal plane growth faster than the vertical one and beam 1 experience losses of about 10% when it starts to collide in IP5.

	Beam	Slot	IP	Ξ_H	σ_{Ξ_H}	$\sigma_{\Xi_{H,syst}}$	Ξ_V	σ_{Ξ_V}	$\sigma_{\Xi_{V,syst}}$	Unit
nominal	B1/B2	-	1‖5	1.8	-	-	1.8	-	-	[10^{-3}]
operation	B1/B2	-	1‖5	4.0	-	-	4.0	-	-	[10^{-3}]
Fill 1765a	B1	100	1	4.37	0.01	1.53	4.19	0.01	0.58	[10^{-3}]
			1&5	7.83	0.01	1.96	8.15	0.01	0.83	[10^{-3}]
	B2	100	1	4.94	0.01	0.34	4.78	0.01	0.18	[10^{-3}]
			1&5	8.70	0.01	0.43	9.15	0.01	0.24	[10^{-3}]
Fill 1765b	B1	100	1	5.97	0.02	2.06	5.16	0.02	0.70	[10^{-3}]
			1&5	9.04	0.02	2.28	10.01	0.02	1.03	[10^{-3}]
		1885	8	3.74	0.01	1.29	3.21	0.01	0.44	[10^{-3}]
	B2	100	1	6.95	0.02	0.48	6.50	0.02	0.24	[10^{-3}]
			1&5	10.59	0.02	0.53	11.88	0.02	0.31	[10^{-3}]
		991	8	3.59	0.01	0.24	2.71	0.01	0.09	[10^{-3}]
Fill 1766a	B1 B2	dumped, due to violation of the save beam limit								
Fill 1766b	B1	100	1	8.87	0.03	3.28	12.13	0.04	1.88	[10^{-3}]
			1&5	10.37	0.02	2.62	11.41	0.02	1.17	[10^{-3}]
	B2	100	1	9.15	0.02	0.65	10.36	0.02	0.38	[10^{-3}]
			1&5	8.33	0.01	0.39	6.37	0.01	0.16	[10^{-3}]
Fill 1766c	B1	100	1	7.83	0.03	2.82	8.95	0.03	1.32	[10^{-3}]
			1&5	14.46	0.02	3.67	16.37	0.03	1.69	[10^{-3}]
	B2	100	1	8.84	0.02	0.63	10.30	0.02	0.38	[10^{-3}]
			1&5	16.17	0.02	0.81	19.12	0.02	0.50	[10^{-3}]
Fill 1911	B1	0	1&5	16.89	0.05	4.21	16.91	0.03	1.69	[10^{-3}]
	B2	0	1&5	13.94	0.01	0.69	15.56	0.02	0.41	[10^{-3}]

Table 3.6: Summary of the determination of the linear coherent beam-beam parameter for all MDs.

3.5 Conclusion

Comparing the tune shifts calculated for fill 1911 and 1766c, one finds similar values for both, even if the initial parameters were quite different. Fill 1766c had intensities around 1.8×10^{11} particles but very small emittances around $1.2\,\mu$m. On the other hand, fill 1911 had even higher intensities around 2.3×10^{11} but emittances of $1.8\,\mu$m, just slightly below the operational value. From this it is convenient to see, that the same tune shift can be obtained under diverging conditions. High intensities but moderate emittances lead to the same result as small emittances with low intensities.

By investigating Equation 1.3 in Chapter 1.1, one can see that this is exactly what is important to reach the optimal luminosity. Pushing the pre-accelerators to produce bunches with the highest intensity and smallest emittance reachable, of course leads to the maximum luminosity possible. But how does those ultra hight brightness bunches react, when they are interacting with each other? Will they behave stable, or will they blow up, loose particles and decrease in lifetime? This is one of the most important questions to be clarified for the luminosity upgrade of LHC to be able to reach the optimum in luminosity.

As well for the daily operation it is important to know what conditions are the easiest ones to handle in the LHC and if the one or the other is more convenient to be produced by the pre-accelerators.

The aim of the experiments discussed in this chapter was to see how far one can push the brightness of the beams without getting into trouble in terms of blow up, losses and lifetime problems. In fill 1911 we already saw related beam blow up and particle losses, but a final limit is not yet been found. Moreover, those experiments discussed where only done at injection energy. It is important to do further analysis at high energies to confirm a stable behaviour under normal running conditions, as well.

However, the tune shifts achieved in the experiments exceed the nominal value by almost a factor of 5 and the value reached in normal operation already by a factor of 2. This is an unexpected but desired result of which nobody had ever thought during the construction of LHC.

4 Orbit Effects

In LHC the beams circulate in two separated beam pipes, they only see each other in the interaction regions (IR) around the interaction points (IP). Here they are brought together into a common beam pipe to prepare for the collisions in the IPs. Therefore, as it is illustrated in Figure 1.1 in Chapter 1.1, a crossing angle must be introduced. Using MADX and the dipole magnets used in IP5 (CMS) to create a horizontal crossing-angel, the corresponding orbit around the interaction point is illustrated in Figure 4.1. The geometry of the crossing angle in Figure 4.1 implies that the beams will be separated everywhere, resulting in long-range interactions, except at the IP where they collide quasi head-on. In the separation plane they collide head-on everywhere, once the separation bumps are collapsed. The separation bump in the vertical plane of IP5 is displayed in Figure 4.2. While the beams are at head-on position in the crossing angle plane directly after injection, they are kept separated in the separation plane to avoid collisions until the beams are fully set up and ready for collisions (ramp to top energy, change from injection to collision optics (squeeze)). To bring the beams into collision the separation bumps (four orbit correctors per plane and per beam at every IP) are collapsed. Those bumps influence the orbit only locally, the optic in the arcs is not affected.

In Chapter 1.2 the beam-beam force was derived from the electromagnetic fields of the beams. Due to this force the beams will exert a kick to each other, which coherent dipole component leads to orbit changes, when the beams are separated. The change in angle (kick) can be computed with

$$\Delta r' = -\frac{2Nr_0}{\gamma} \cdot \frac{1}{r} \cdot \left[1 - \exp(-\frac{r^2}{4\sigma^2})\right] \tag{4.1}$$

where r is the beam separation, σ the beam size at the interaction point, N the intensity, r_0 the classical particle radius and γ is the relativistic Lorentz factor.

In this chapter the long-range beam-beam kick will be investigated in detail. First the results of a dedicated machine study period are presented, where the effect of the separation between the beams was measured on single bunches without long-range interactions during an orbit scan, i.e. the isolated long-range kick for one interaction as a function of the separation is studied. Followed by an analysis of data taken during normal physics runs with a high number of bunches. The effect from bunch-to-bunch is studied to examine differences arising from missing long-range interactions at the head and tail of bunch trains, the so-called PACMAN-effect, see Chapter 1.4. The results are compared with simulations done in previous studies [6].

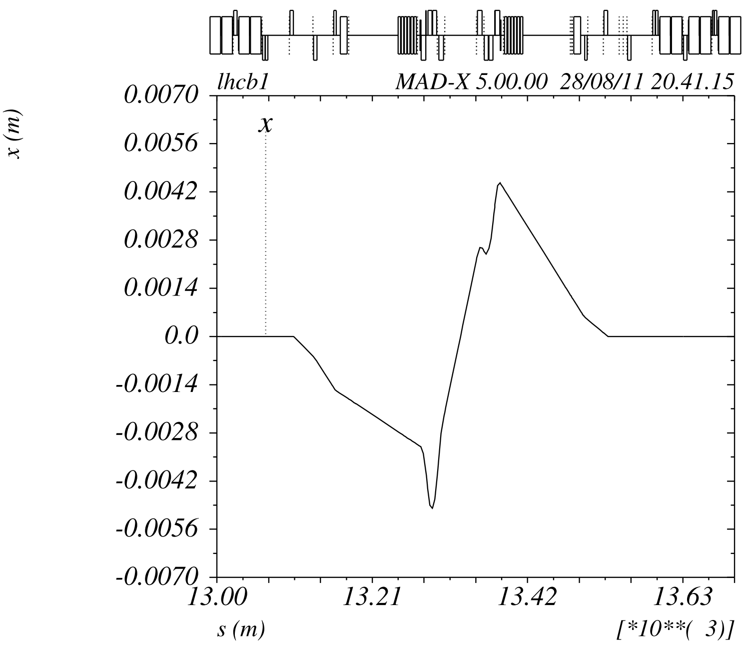

Figure 4.1: Orbit of beam 1 around CMS. Four corrector magnets are used for the creation of a horizontal crossing-angle. At 3.5 TeV the corresponding angle is 240 μrad. The top row shows the lattice in the considered sector: centred squares indicate bending magnets, lowered (upper) ones defocusing (focusing) quadrupoles. This is a MADX simulation.

4.1 Long-Range Beam-Beam Kick

In the same MD as mentioned in the previous chapter (fill 1911), with only one bunch circulating per beam, a horizontal orbit scan was performed in ATLAS (IP1) and a vertical one in CMS (IP5).

When only one bunch is present per beam, influence arising from parasitic encounters with other bunches (long-range) are avoided. Moreover, the scans were done in the separation plane to separate the barycentres of the bunches and not just shift the centre of the interaction away from the IP, as it would be the case for a separation in the crossing plane. To avoid additional effects arising from the trim of the separation bumps (e.g. the non-closure effect: due to magnet errors the bumps does not close perfectly, leaving an offset or angle which causes an additional oscillation around the ring), only beam one was moved and beam two was untouched. In this way beam two is only perturbed by the beam-beam kick. This set up provides the cleanest signal available to measure the orbit kick due to the beam-beam force when the beams are separated.

After a luminosity optimization, where the beams were brought to their total overlap position in the IPs, the scans were done in steps of 100 μm, which corresponds

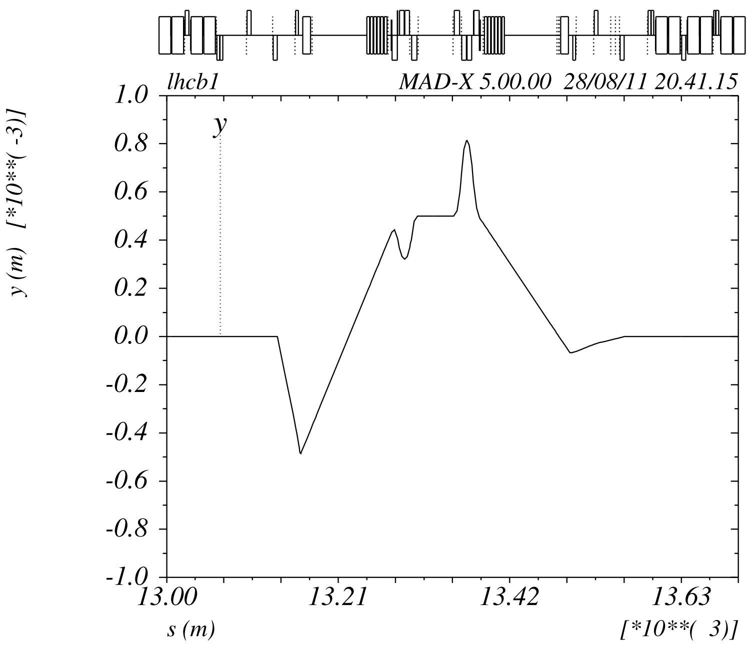

Figure 4.2: The orbit of beam 1 around CMS, when the separation bump is active in the vertical plane. This bump is included in the injection optics and is collapsed when the beams are brought into collisions. Simulation done with MADX at 3.5 TeV.

to approximately $0.5\,\sigma$, until a maximum separation of $800\,\mu$m ($\sim 4\,\sigma$). The beams remained at each separation step for about one or two minutes. The separation went far enough to reach the non-linear regime of the beam-beam force (Figure 1.3).

The results are presented in Figure 4.3, where in the top plot the scan in IP1 and in the bottom plot the scan in IP5 are shown. The red line indicates the measurement, to which the black curve was fitted using Equation 1.14, the box gives the obtained fit parameters. For comparison, Equation 1.14 was also used to predict the effect based on the measured beam size and intensity, blue function. The green dashed line approximates a self-consistent treatment of the effect.

During the scan the orbit was measured by the LHC BPM system (Chapter 2.3.2) as an average of the beam position over 225 turns. 516 Beam Position Monitors per beam are placed around the ring and each of them gives a position with respect to the design orbit turn-by-turn.

The measured orbits include the betatron oscillation and other effects which are much larger than the oscillation caused by the beam-beam kick. However, those offsets will be identical for colliding and separated beams, therefore, they can be filtered by taking the difference of each orbit with respect to a reference before the scan was started. An average over 10 measured orbits directly before the scan in each IP began was taken for that purpose. In this why, the filtered orbits before the scan was stared are flat (only with statistical fluctuations of the devices). The filtered orbits, after a step of

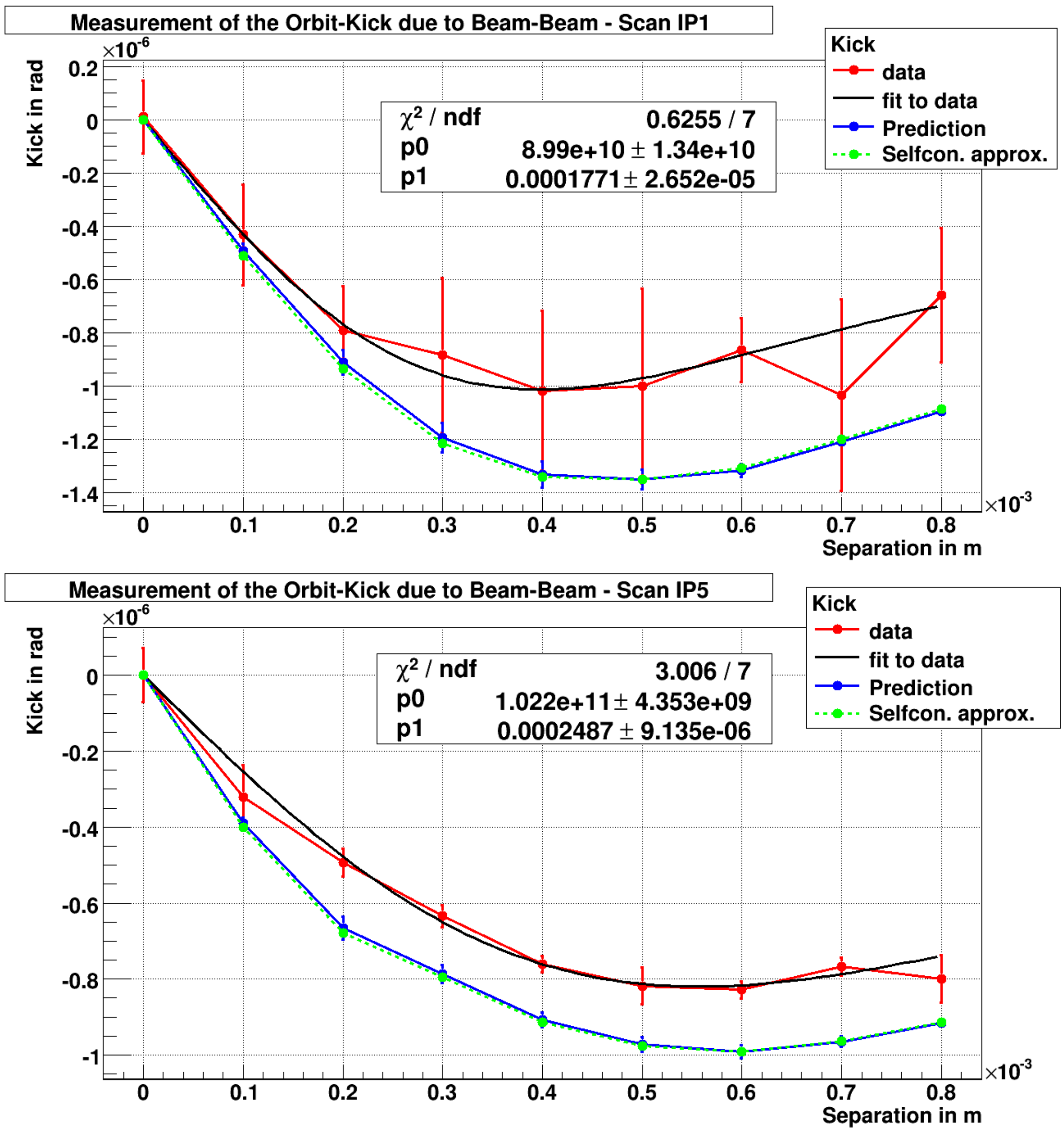

Figure 4.3: Measurement and prediction of the orbit kick due to beam-beam force during a horizontal orbit scan in IP1 (top) and a vertical one in IP5 (bottom). The vertical axis is given in units of 10^{-6} rad and the horizontal axis in units of 10^{-3} m.

separation is performed, show small deflections arising from beam-beam interaction.

The filling pattern implies that the beams only interact in IP1 and 5 and only head-on (zero separation), which should not influence the orbit, when a luminosity optimization was done and the beams are perfectly overlapping at the collision points.

A virtual orbit corrector magnet (Closed Orbit Dipole, COD) was placed directly at the IP, where the perturbation acts. Like during an operational orbit correction, this corrector was told to apply a kick of the strength which would give the best correction, i.e. to bring the orbit as close to the reference as possible. The applied kick of the corrector was then taken as the measurement of the inverse beam-beam kick. It is assumed that the deflection of the orbit only comes from the beam-beam interaction at the IP due to the induced separation, thus, the virtual corrector at the IP should give the best correction possible. This procedure was done for each orbit measurement taken during the scan. The kicks obtained for each step were averaged and shown with their standard deviation as the red curve in Figure 4.3.

The beam size measured by the BSRT and the intensity delivered by the DCBCT for beam 1 were used to calculate the expected kick beam 1 exerts to beam 2. Since the intensity and emittance changes during the scan, an average of the beam size at the IP and the intensity was taken over the duration of each separation step to better reproduce the actual situation, shown as the blue curve in the Figure.

A gap between the measurement and the prediction is clearly visible. To investigate the origin of the gap a fit (black curve) was done to the measurement (red) using Equation 1.14, while leaving σ and N as free but constant parameters. The results are indicated in the box in the plot where $p_0 = N$ and $p_1 = \sigma$ and in Table 4.1. Comparing those with the initial parameters before the scan was started, given in Table 4.1, it can be seen that the beam sizes are in agreement with the measured ones but the intensities are too small in both cases. Since the intensity measurement is trusted well within errors, the origin of the discrepancy must be different.

	N (DCBCT)	N (Fit)	σ at IP (BSRT)	σ at IP (Fit)
IP1	$(1.67 \pm 0.01)\times 10^{11}$	$(0.90 \pm 0.13)\times 10^{11}$	$(227 \pm 6)\,\mu$m	$(177 \pm 27)\,\mu$m
IP5	$(1.42 \pm 0.01)\times 10^{11}$	$(1.02 \pm 0.04)\times 10^{11}$	$(233 \pm 5)\,\mu$m	$(249 \pm 9)\,\mu$m

Table 4.1: Initial beam parameters at the beginning of the orbit scans in comparison with the ones obtained by the fit in Figure 4.3.

Therefore, the green dashed line tries to approximate the self-consistent effect of the interaction itself. If the orbit is changed due to a bunch crossing, the position of the beams will be different after one turn, which implies a variation of the force, leading again to a different orbit until an equilibrium is found. The approximation was done with MADX: the expected kick was again calculated with Equation 1.14 as for the blue curve and applied at the position of the interaction, afterwards the beam position at the IP was taken and added twice to the value of the separation, since both beams experience the same kick but in opposite directions. With the new separation the kick

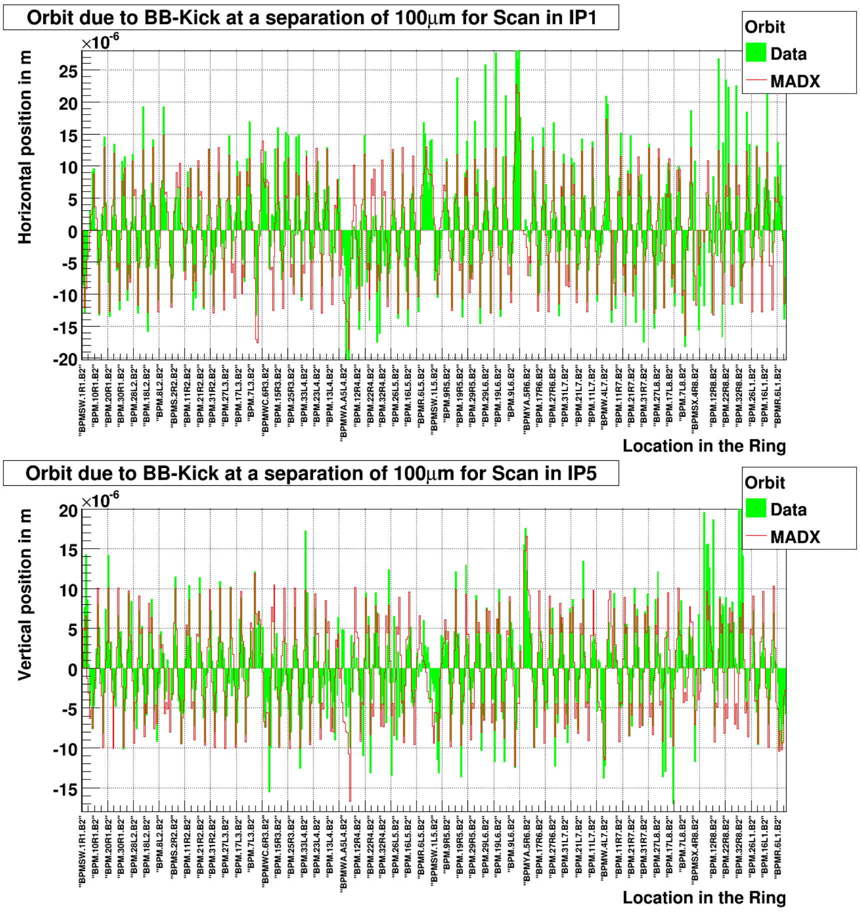

Figure 4.4: Orbit as measured by the BPMs (green) and as obtained by MADX while applying the calculated kick (with Equation 1.14) in the IP corresponding to a beam separation of 100 μm. Top: scan in IP1, bottom: scan in IP5.

is calculated again until the change in the position saturates. The dashed line shows that this effect is quite small and not able to explain the gap.

In Figure 4.4 and 4.5 (left) the orbit at a beam separation of 100 μm is shown as measured by the BPMs (green) and as obtained by MADX (red), when applying the calculated kick for the given separation, for the whole ring and a zoom to the first sector after the scanned IP, respectively, i.e. for the scan in IP1 sector 12 between IP1 and 2 and for the scan in IP5 sector 56 between IP5 und 6 is shown in Figure 4.5. Only the separation plane of both IPs is plotted, since only here the effect will be visible.

Both orbits show a similar oscillation, while the quality of the agreement can be investigated easily by looking at the difference orbit between the measurement and MADX, which shows the remaining part of the orbit after the prediction is subtracted, the right hand side of Figure 4.5 shows this for the zoomed areas on the left. For the first sector the orbits overlap relatively good, only small discrepancies can be seen,

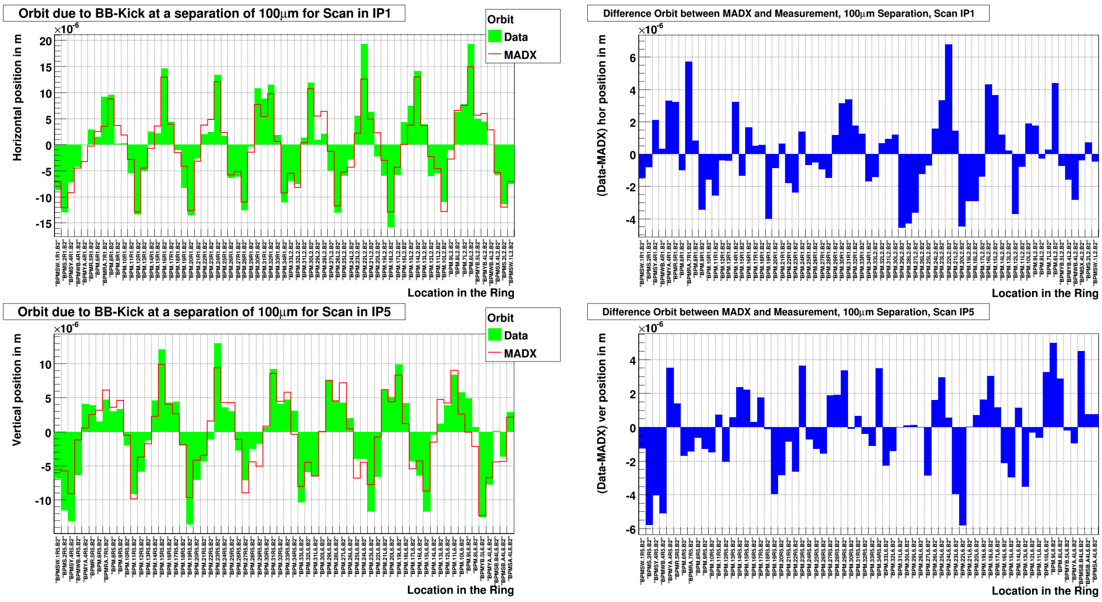

Figure 4.5: Left: Orbit as measured by the BPMs (green) and as obtained by MADX while applying the calculated kick (with Equation 1.14) in the IP corresponding to a beam separation of 100 μm. On the right a difference of both orbits is illustrated. All plots show a zoom to the first sector after the scanned IP. Top row: horizontal separation in IP1, bottom: vertical separation in IP5.

which, as the difference orbit indicates, are in the order of ± 5 to 6 μm, corresponding to the noise level of the BPMs (see Chapter 4.2.2). However, as the oscillation propagates through the ring some BPMs show bigger differences and going to larger separations (above 500 μm) some sectors become very bad and give differences of more than 15 μm. Moreover, sometimes it seems that an oscillation remains in the difference orbit. The corresponding separation, where those additional perturbations become stronger, appears to be around the maximum of the beam-beam kick, after which the kick becomes smaller with increasing distance between the beams.

Nevertheless, it is known that the signal of the BPMs depend on the intensity of the beam, that's why they are operated in a low or high sensitivity mode depending on the bunch intensity, but also the position of the beam is important for the quality of the signal. Only in the center of the beam pipe the real position is proportional to the signal, in the outer regions it becomes non-linear. For linear optics the amplitude of the oscillation is proportional to the provoking perturbation (kick), i.e. the offsets at the BPMs increase with increasing kick. Taking those non-linearities in the read-out of the BPMs into account and that the orbits shown are already the difference with respect to a reference orbit before the scan was started, it is possible that the beam position at some BPMs is outside the linear regime and therefore gives a wrong signal. Since all BPMs where used for the analysis, already some wrong signals will influence the result and lead to a discrepancy with the prediction. This could be an explanation for the discrepancies between the measurement and the expectation.

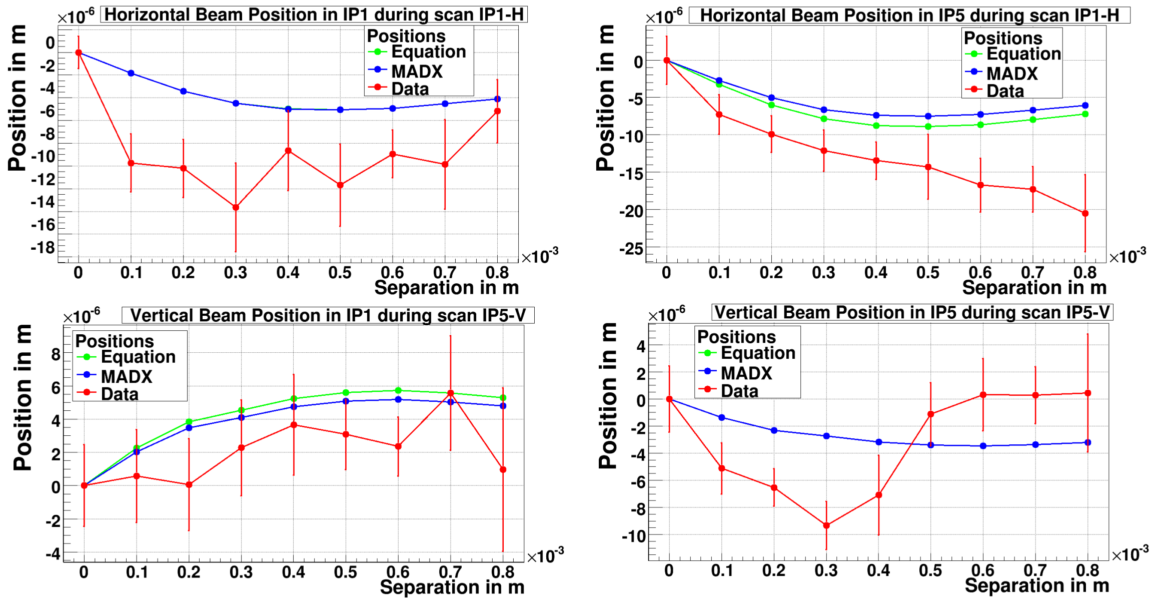

Figure 4.6: Measurement and prediction of the position at IP1 and IP5 due to beam-beam force during the orbit scans. The vertical axis is given in units of 10^{-6} m and the horizontal one in units of 10^{-3} m.

To complete the analysis of the long-range beam-beam kick measured in a separation scan, Figure 4.6 shows the measured offset in IP1 and IP5 with its standard deviation (red) and the predicted positions (MADX: blue, Equation 4.2: green) in the separation plane of IP1 (left) and IP5 (right) when the scan was performed in IP1 (top) and IP5 (bottom) as a function of the separation.

The blue expectation from MADX is given by the first iteration of the self-consistent approximation. The propagation of a kick $x'(t)$ at point t through the lattice can be determined using

$$x(s) = \frac{\sqrt{\beta(s)\beta(t)}}{2\sin(\pi Q)} x'(t) \cos(|\psi(t) - \psi(s)| - \pi Q) \tag{4.2}$$

to get the offset $x(s)$ at point s due to this kick. Where Q is the tune, $\beta(a)$ the β-function at point a and $\Delta\psi = |\psi(t) - \psi(s)|$ the phase advance between the considered locations. This was done for the expected kicks in both IPs, and is shown as the green line. Both predictions give the same values in the case of zero phase advance, i.e. if the position in the scanned IP is calculated, while they differ when $\Delta\psi \neq 0$ and the position in the opposite IP is considered. Equation 4.2 is based only on linear optics (dipoles and quadrupoles) while MADX includes all magnets contained in the LHC sequence, which goes up to decapoles, i.e. non-linear elements are considered. When MADX propagates a kick from one place to another it takes all elements in between and calculates their influence on the beam. Therefore, if the position in a higher order element is non zero, non-linearities are introduced to the orbit which is not considered in the equation, modifying the result.

Also here a discrepancy between prediction and measurement is found. Nevertheless, the position at the IPs were interpolated from the data of the two closest BPMs on the left and right hand side of the IP only. Those BPMs are strip line BPMs and have a resolution of around $\pm 5\,\mu$m (see Chapter 4.2.2), which is not taken into account, but is already larger than the standard deviation and the observed discrepancy. As expected, the shape of the curves agree with the prediction (except for the beam position in IP5 during the scan of IP5, which needs further investigation). However, the source of the gap will be explained, when the gap in Figure 4.3 is understood.

4.2 Orbit Effects due to Bunch-by-Bunch Differences

The beam-beam kicks from the parasitic interactions distort the orbits of the individual bunches, due to the coherent dipolar component of the kick. Since the collision pattern is different for different bunches, the orbits of all bunches are slightly different (PACMAN-effect, see Chapter 1.4). As a consequence, the orbits at the interaction points are different and the bunches collide with small offsets.

In the following observations of the bunch-by-bunch differences for the orbit position in IP1 (ATLAS) will be presented, using different measurement methods to be able to address the effect in the two planes. Simulations were done in a previous study [6], which will be used to understand the observations.

4.2.1 Simulations

Figure 4.7 and 4.8 show simulations [6] of the offsets at the interaction point of ATLAS in the vertical-crossing plane and in the horizontal-separation plane, respectively. For CMS the same structure appears, but in inverted planes, since the the beams cross horizontally. The top picture shows the positions for a perfect beam (all bunches are identical) and the bottom one includes intensity variations between bunches of 20%. In daily operation the bunch-by-bunch intensity fluctuations are of the order of 10% to 20% [35], hence, 20% is a good approximation of the real conditions.

The simulations were done for the nominal filling scheme of LHC (see Figure 1.9) which exhibits a fourfold symmetry, therefore only one forth of the whole beam is shown. The red points represent beam 1 while the green ones show the positions of beam 2. Since the biggest contribution comes from IP1 and IP5, only those IPs were simulated.

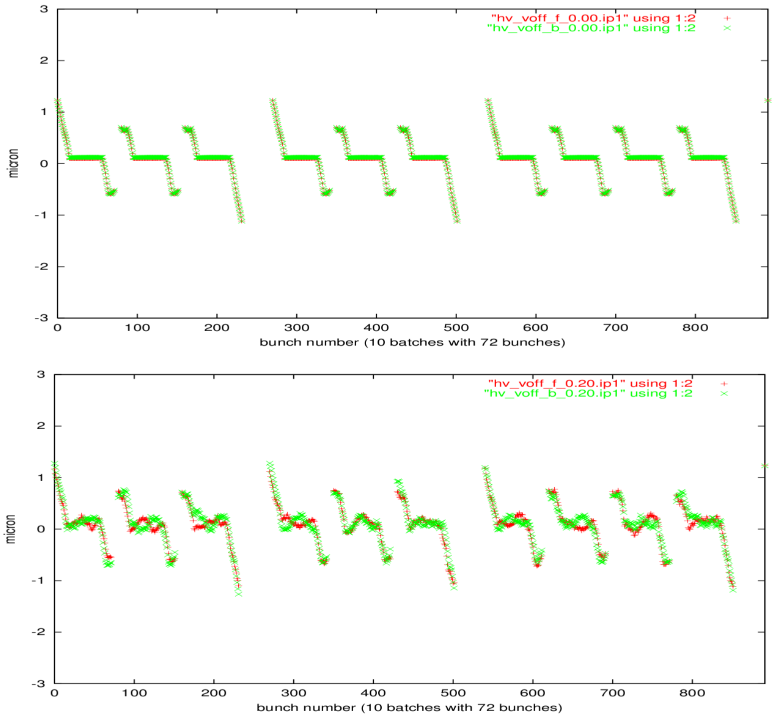

Figure 4.7: Vertical offset in IP1 with identical bunches (top), intensity variations of 20% included in the bottom plot [6]. Red: beam 1, green: beam 2.

Crossing Plane

In the vertical plane (Figure 4.7) an asymmetric structure with respect to the center of the train is found. Both beams show identical orbits, therefore the bunches collide head-on, although not on the central orbit. On the other hand, in the horizontal plane both beams are separated, and the PACMAN-bunches show a smaller offset with respect to the central orbit as the core of the train. Moreover, the offsets for head and tail appear symmetrically. This can be understood by symmetry considerations:

Close to the IP, before the inner triplets, the β-function can be calculated as in a drift space through the equation [13]

$$\beta(s) = \beta^* + \frac{s^2}{\beta^*} \tag{4.3}$$

where β^* is the β-function at the IP (point of symmetry), which grows quadratically with the distance s from the symmetry point. The phase advance over a distance s is given by [13]

$$\psi(s) = \int_0^s \frac{d\sigma}{\beta(\sigma)} \tag{4.4}$$

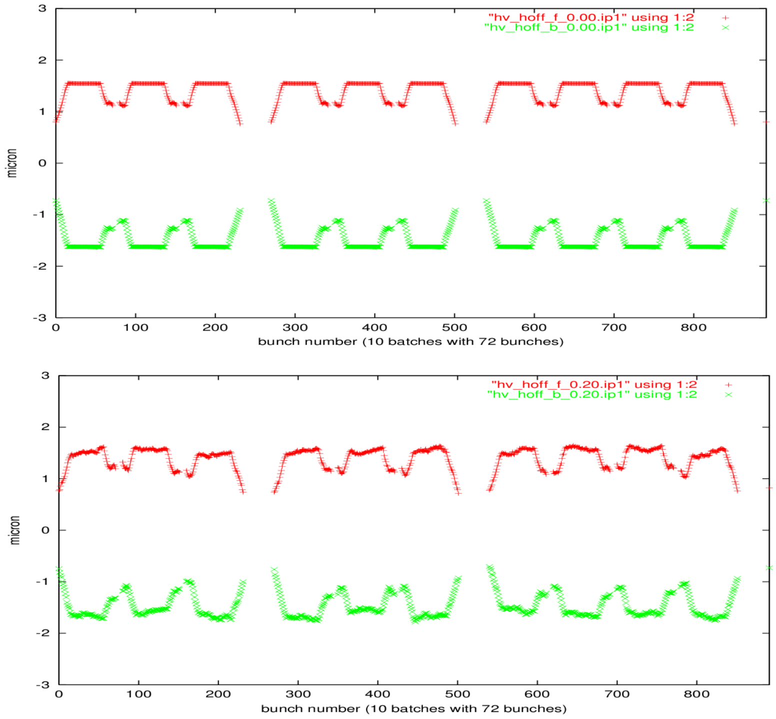

Figure 4.8: Horizontal offset in IP1 with identical bunches (top), intensity variations of 20% included in the bottom plot [6].

Inserting Equation 4.3 into 4.4 leads to

$$\psi(s) = \int_0^s \frac{d\sigma}{\beta^* + \frac{\sigma^2}{\beta^*}} = \frac{1}{\beta^*}\int_0^s \frac{d\sigma}{1+\frac{\sigma^2}{\beta^2}} = \frac{1}{\beta^*}\arctan(\frac{s}{\beta^*}) \tag{4.5}$$

For small β^* ($\ll s$) the phase advance, $\psi(s)$, calculated from the IP to both sides, reaches $\pm 90°$ very fast and stays at this value until the first magnet of the inner triplet is reached. From here on, ψ changes its values quite fast due to the lattice elements. Thus, all long-range interactions, in the drift space between the left and right inner triplet, happen at a phase advance of about $\psi = 90°$ with respect to the IP.

Two kicker magnets with a phase advance of 180° will produce a closed orbit bump, if they exert opposite kicks to the beam. In the center of this bump the angle is zero. Consequently, if those kickers exert identical kicks, the bump will no longer be closed, instead an oscillation is introduced, which propagates through the whole ring.

Thinking of the long-range interactions as kickers (as indicated in Figure 4.9), it is easy to see how the patterns develop. In the vertical plane the history of long-range interactions for leading and tailing bunches when they arrive at the IP is different. On the way to the IP the head collides with empty buckets and thus misses long-range kicks, while the tail sees the opposite beam, but misses parasitic encounters when it leaves the IP. Consequently, the kicks exerted to the head have the opposite sign than

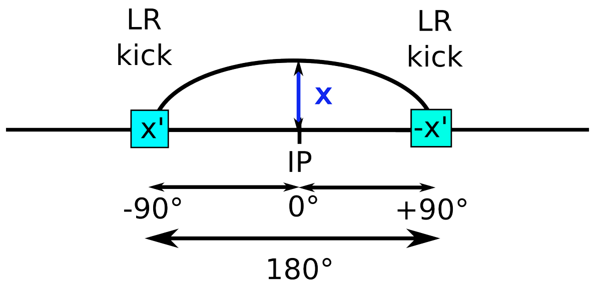

Figure 4.9: Visualization of the effect of the phase advance between two identical long-range kicks to the left and right hand-side of the IP.

the ones for the tail, leading to a left-right asymmetry. Bunches in the core of the train accumulate the same number of kicks to both sides of the IP with opposite signs and the effect cancels. It is convenient to see that these interactions are the same for both beams, which produces identical orbits, therefore all bunches collide head-on in this plane, although not all of them on the central orbit.

Separation Plane

For the horizontal plane, however, no long-range interactions take place in IP1, thus the effect must arise from the horizontal plane in IP5, which here is the crossing plane where long-range effects are introduced. Nevertheless, the effect of the long-range encounters in IP5 has to propagate through the ring until they arrive at IP1. The propagation of a kick $x'(t)$, at the location t, through the lattice, resulting in an offset $x(s)$ at the considered position s can be calculated with Equation 4.2. As explained above, equal long-range interactions to both sides of the IP ($s = 0$) has a phase advance of $\Delta\psi = 180° = \pi$, but opposite sign ($x'(s) = -x'(-s)$). Due to the phase advance between IP1 and IP5, both effects cancel when arriving at IP1, because $\cos(\Delta\psi + \pi - \pi Q) = -\cos(\Delta\psi - \pi Q)$. Thus, symmetric offsets for head and tail bunches are observed.

The effect on PACMAN-bunches is smaller, since they experience less long-range interactions and thus they accumulate a smaller integrated kick than core bunches.

Influence of Intensity Variations

As it can be seen from Equation 1.14, the exerted kick from one bunch to the opposite depends on the intensity. If intensity variations between bunches are included (bottom plots of Figure 4.7 and 4.8), a bunch from the core of the train is kicked differently at the left and right side of the IP, since it interacts with different bunches with different intensities. Hence, the kicks from both sides do not cancel exactly any more and the core bunches are left with small offset variations.

Details of the orbit effects

The unexpected bump feature for the first bunches of a batch, which is surrounded by batches of the same train, is a combination of two effects: first those batches in the middle of a train only have a distance of 8 missing bunches (225 ns) to the batch in the front and back, therefore the first bunches will still see the tail of the leaving batch and the last bunches will interact already with the head of the next. Thus, the linear behaviour as a function of the number of long-ranges, visible for PACMAN-bunches before and after a larger gap (38 or 39 missing bunches) between trains is perturbed. Secondly, a gap of 8 bunches is enough to miss out long-range encounters in the drift space, but not those in the triplet. Therefore, the last and first 8 bunches will have the same number of long-range interactions but at different positions in the triplet magnets where the strength of the interaction differs.

For large amplitudes ($r > 2\,\sigma$) the strength of the long-range kick decreases with the separation. But since Equation 1.14 is depending on the separation and the beam size, one has to take into account that the beam size changes with the β-function. In the drift space around the IP, between the left and right inner triplet, the β-function can be calculated with Equation 4.3. Hence, the beam size $\sigma = \sqrt{\beta\epsilon} \propto s$ is approximately proportional to the distance from the IP, for small β^*. Consequently, all long-range interactions between the inner triplets to both sides of the IP can be approximated to have the same strength, since the separation due to the crossing angle increases linearly in this region, as well. Nevertheless, a closer investigation of Figure 4.1 shows that this linearity with s stops at the first magnet next to the IP. From here, it is not straight forward to see which is the strongest long-range interaction, since separation and beam size change differently due to the lattice properties.

4.2.2 Beam Position Monitors

The LHC Beam Position Monitors (BPM) have an acquisition mode that allows to acquire the orbit data bunch-by-bunch using an average over 225 turns to cancel the 50 Hz noise. An exhaustive analysis of these data during a typical luminosity run has been performed in order to assess the feasibility of those instruments to measure closed orbit deviations of the order of few micrometers, as they are expected from beam-beam interactions. In the following the observations are summarized:

- The BPM noise on a bunch-by-bunch basis is consistent with what can be expected from the current filtering algorithm applied to the data, and scales as expected with BPM aperture: BPMSY ($\pm 7\,\mu$m) > BPMSW ($\pm 5\,\mu$m) > BPM ($\pm 3\,\mu$m). The first two BPMs are strip line monitors and the last one is a button pick up. The left plot in Figure 4.10 shows an example of the residual noise for a button BPM.
- Most of the BPMs show pretty stable bunch-by-bunch orbits for a given orbit, even though the electronics reacts differently to different bunches in the train. In some cases, however, e.g. BPM16L4 (Figure 4.10, right) some structure is still

visible (at the $10\,\mu$m level) which probably still comes from the electronics.

- The difference between the mean position over several measurements before and after the beams are brought into collisions gives, for some BPMs, offsets of the order of 100 μm. A possible explanation could be that at the end of the squeeze certain orbit corrections are incorporated into the collision process in order to guarantee the reproducibility from fill to fill, and these orbit corrections could be the source of the offset. Temperature effects cannot explain those offsets since they are of the order of few micrometers.
- Another systematic behaviour of the bunch-by-bunch data is that when the position before and after collision are very similar, the result of the subtraction of both orbits becomes fairly flat (Figure 4.11, top). However, when the positions are significantly different bunch-by-bunch structure becomes visible (Figure 4.11, bottom). A possible explanation could be the existence of a non-linearity in the bunch-by-bunch response of the electronics which depends upon the position.

The conclusion from the observations is that the LHC BPM system has a bunch-by-bunch orbit measurement which can give a relative bunch-to-bunch resolution in the $5\,\mu$m range. However, the non-linearity in the bunch-by-bunch measurement for different global positions limits this resolution to $\pm 50\,\mu$m when comparing along the train for different mean positions. The current LHC BPM system therefore does not have sufficient linearity or resolution to resolve the bunch-by-bunch orbit variations at the few micrometer level expected from beam-beam interaction orbit effects.

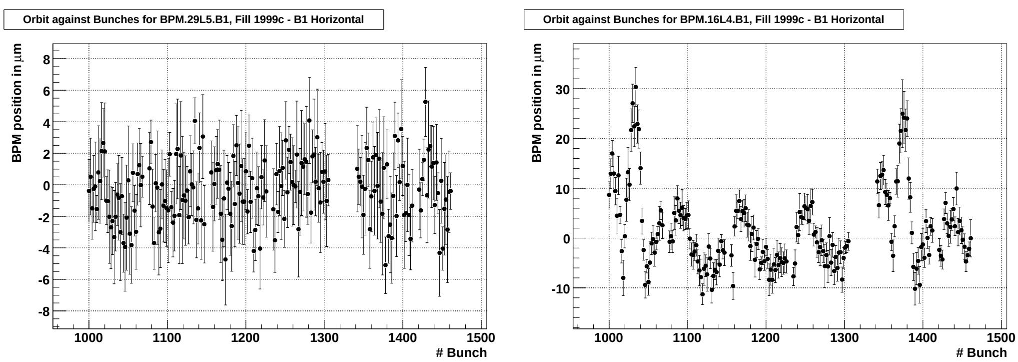

Figure 4.10: Example of the bunch-by-bunch signal before collisions after filtering for the electronics effect. Left: a well behaving bottom BPM in the arc left to IP5, right: a bottom BPM with structures left in the arc to the left of IP4. A physics fill with 1380 bunches spaced by 50 ns was analysed.

4.2.3 ATLAS Luminous Region Reconstruction

Ideally the position of the two beams should be measured separately. Unfortunately, the BPM system is the only device existing in the LHC able to measure the beam position

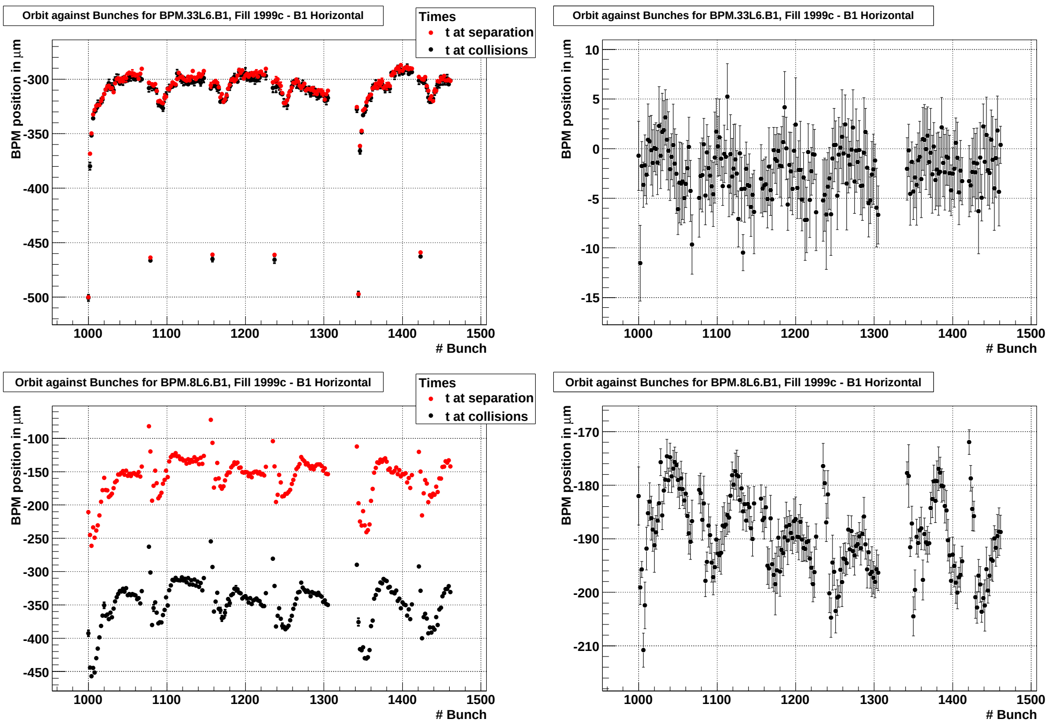

Figure 4.11: Example of the bunch-by-bunch signal before and in collisions where the global positions for both orbits are similar (top) and different (bottom), the raw measurement is plotted on the left, on the right a difference between the orbit before and in collisions is shown.

of one beam independently from the other, but as shown in the previous section, its resolution is not enough to resolve effects arising from beam-beam interactions.

With the LHC experiments' vertex detectors it is possible to measure the position of the so-called luminous centroid, which is a convolution of both beams showing the center of the collision, where the highest luminosity was produced. Nevertheless, since this detectors can only provide an average over both beams, bunch-by-bunch differences in the position can only be seen where the two beams have nearly identical orbits. In that case, the position of the luminous centroid can be interpreted as the beam position of a single beam. Moreover, those detectors have the required resolution to study the beam-beam induced orbit differences between bunches. The analysis presented in the following uses the microvertex detector of the ATLAS experiment.

In Figure 4.12 the reconstructed position of the luminous centroid measured by the primary vertex detector of ATLAS is shown as a function of the bunch crossing identifier, which is equivalent to the slot number. A normal luminosity fill with 1380 bunches spaced by 50 ns (1 missing bunch) was analysed. In the top picture the vertical plane is displayed, which is the crossing plane in IP1, the bottom one illustrates the

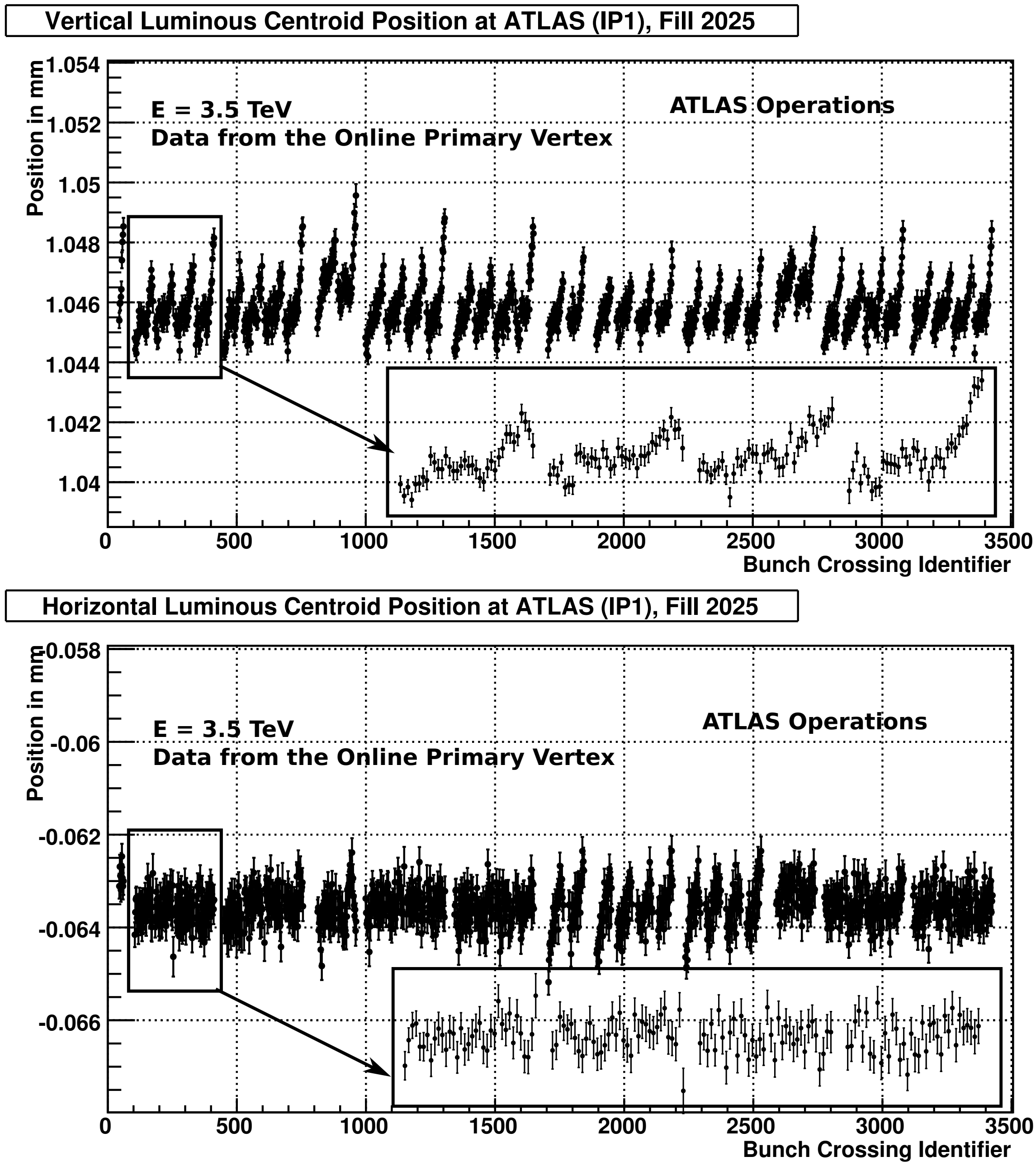

Figure 4.12: Luminous centroid position in ATLAS. Top (bottom) Figure shows the vertical (horizontal) luminous region position and a zoom over the first train of 4 PS batches consisting of 36 bunches.

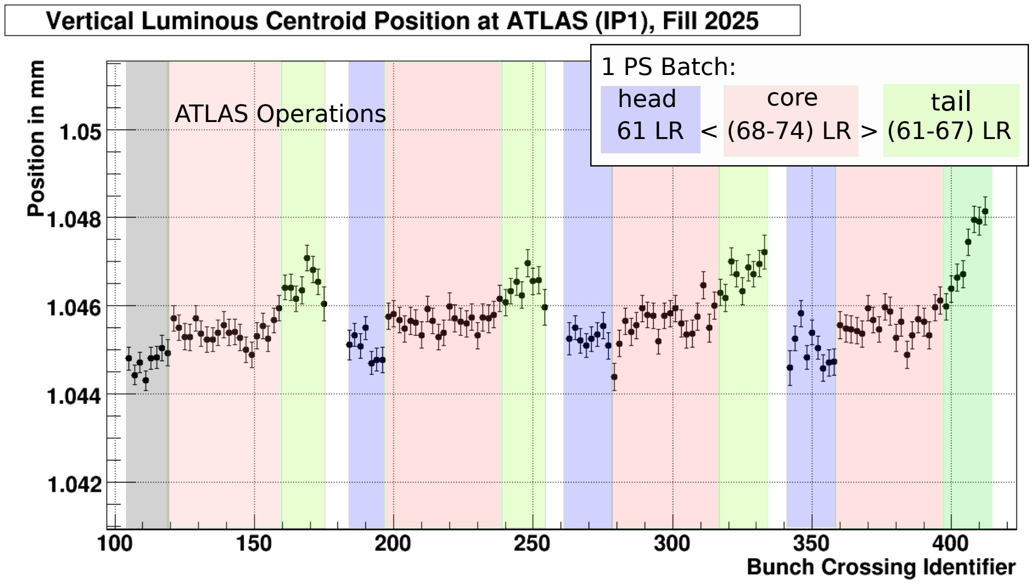

Figure 4.13: Luminous centroid position in ATLAS. Zoom to the first train of 4×36 bunches. Red lines indicate the gaps between trains of 36 bunches, 8 missing bunches. To the left and right of the group bigger gaps of 56 bunches follow. Blue lines group bunches in head, core and tail due to their number of long-range interactions (LR, black numbers).

horizontal (separation) plane.

In the vertical plane a clear effect is visible, which implies that the orbit of both beams must be very similar, as the simulations in Figure 4.7 predict as well. On the other hand, in the horizontal plane no structure shows up, because the orbits of the two beams are symmetrically separated, thus the average of both will give the position of the central orbit without any significant patterns.

A zoom to the first train of 4 PS batches made of 36 bunches each is illustrated in Figure 4.13. The colors help to distinguish between the head (beginning, blue), the middle (core, red) and the tail (end, green) of the batch, while the boundaries are not strictly set. A rough overview over the range of the number of the experienced long-range interactions, summed over the whole ring, is given, to be able to compare the dependency of the observed effect.

The structures found in the simulations in Figure 4.7 can nicely be recognised: the core bunches all have a relatively similar orbit, where the variation is due to intensity fluctuations bunch-by-bunch, which have been around 15% for the considered fill. As well, the asymmetry with respect to the middle of the train, arising from the different sign of the long-range kicks to the left and right of the IP, can be seen. It shows up mirrored in comparison to the simulations, which is just because of a sign convention in the simulation program and does not arise from a physical effect. Nevertheless, the differences in particular for the PACMAN-bunches are obvious, even the detailed bump feature coming from the different size of the gaps between the batches is visible. The bunches next to a large gap of 38 missing bunches at the boundaries of the train (very left and right side of the plot, grey and dark green coloring in Figure 4.13, respectively) show a linear behaviour as a function of the number of long-range encounters, this structure is perturbed for the middle of the train, where the batches are closer together. Here they are only spaced by 8 missing bunches, therefore the last bunches of a batch will see the first bunches of the next batch, leading to additional kicks at different positions in the triplet.

Orbit differences up to 5 μm from bunch-to-bunch are found, which is more than obtained in the simulations, they only show 2 μm difference from bunch-to-bunch. The simulations, however, where done for a different filling pattern (nominal filling: 2808 bunches, 25 ns spacing) and assuming nominal beam parameters (1.15×10^{11} particles per bunch, 3.75 μm rad normalised emittance, 7 TeV energy). In the analysed fill 1380 bunches, spaced by 50 ns were present in the machine and as well the beam properties differ from the nominal ones: the average emittance and bunch-by-bunch intensity are around 2 μm rad and 1.2×10^{11} particles, respectively, while the machine is running at 3.5 TeV. Therefore, it is not surprising that the amount of the effect observed does not agree with the simulations. While remembering Equation 1.14 this becomes even more clear, since the kick depends on the beam size and intensity.

Nevertheless, the shape of the measurement is found to be in very good agreement with the prediction.

Several luminosity fills with different filling schemes have been analysed to investigate the dependence on the number of bunches. But as long as the spacing and the number of bunches per train is keep the same, no dependence is found, since the number of long-range interactions, which are responsible for the effect, is constant as well.

4.2.4 Luminosity Optimization

During every luminosity run, once the beams are brought into collisions, ATLAS and CMS undergo a luminosity scan in the horizontal and vertical plane to find the full beam overlap and therefore the maximum luminosity. This process is done integrating the luminosity over the whole beam, and assuming an average position over all bunches. However, since it was demonstrated that there are bunch-by-bunch orbit differences, it is interesting to look at the variation in the maximum of the luminosity as a function of the bunch number.

In such a scan the two beams are moved synchronously in the opposite direction in steps of $0.5\,\sigma$, where the nominal emittance $\epsilon = 3.75\,\mu$m rad is used to assume the beam size σ at the IP. Three measurement points are taken, while zero indicates the starting position. To perform an analysis bunch-by-bunch the luminosity data of the LHC BRANs (Beam RAte of Neutrals), the machine luminosity monitors, to the left and right side of the IP are taken for each bunch and plotted as a function of the scanned

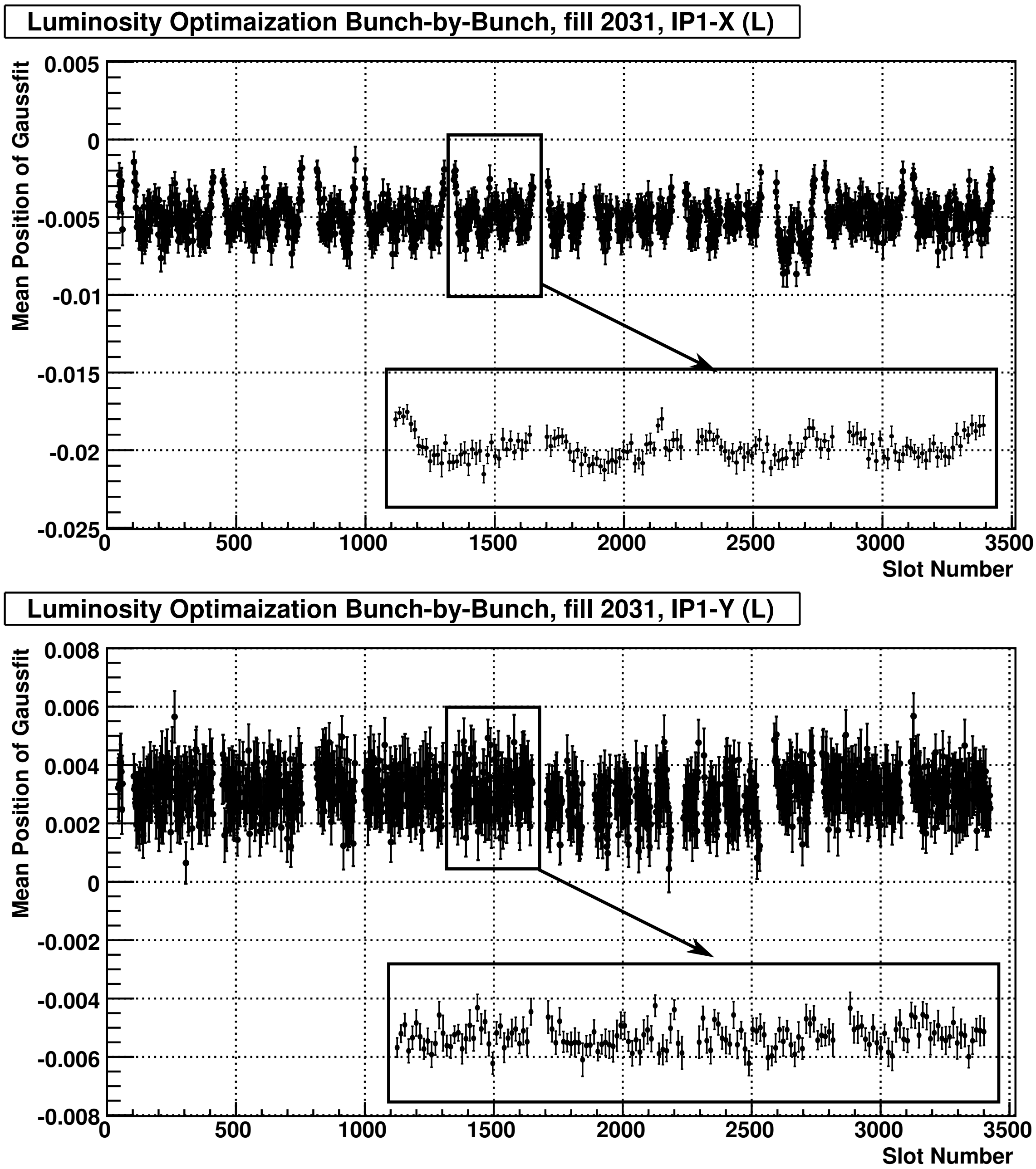

Figure 4.14: Position of the maximal luminosity (total bunch overlap) as a function of the bunch number. Top (bottom) Figure shows the horizontal (vertical) mean position of the luminosity maximum in units of mm w.r.t. the beam position before the scan.

position (in mm). The luminosity data of every bunch is fitted to a Gaussian, where its mean position gives the total beam overlap for the specific bunch. The obtained positions of the maximum luminosity are shown as a function of the slot number in Figure 4.14. The top picture contains the observations in the horizontal plane and on the bottom the vertical plane is illustrated, the data were taken by the BRAN on the left side of ATLAS.

In the horizontal plane bunch-by-bunch differences in the order of 5 μm are clearly visible, while the effect washes out in the vertical plane. This is easy to understand by reconsidering the orbit for both beams observed in the simulations in Figure 4.8. Figure 4.15 tries to visualise the luminosity scan in the vertical (top) and horizontal (bottom) plane considering the orbit differences bunch-to-bunch. A scheme of the scan in three steps is shown for one pair of colliding batches.

The vertical orbits for both beams are nearly identical for position zero, when the scan is started both are separated, but the distance between the bunches is the same for all colliding pairs for a given step (see position 1 and 2), therefore the mean positions of the Gaussian fit will all have the same value within fluctuations. For the horizontal plane the situation is different. When the two beams are moved together, the PACMAN-bunches at the head and tail of the train will hit the total beam overlap (position 1) earlier than the bunches in the core (position 2), which leads to different positions of the maximum luminosity.

Thus the orbit effect introduced by beam-beam interactions can be observed in the horizontal plane but not in the vertical plane. Nevertheless, the effect in the horizontal plane is in qualitative agreement with the simulations. A discrepancy in the amount of the effect is found here, as well. The data shows a bunch-by-bunch difference of 5 μm but the simulations only have 1 μm. The reason could be explained by the different beam properties of the analysed data compared to the simulated data.

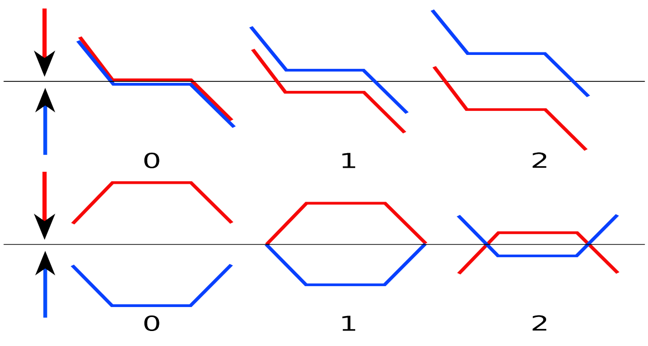

Figure 4.15: A luminosity scan in the crossing (top) and separation (bottom) plane in three steps. The pattern of the orbit as a function of the bunches along a train is schematically shown, the red train is moved downwards, while the blue one is moved upwards. All bunches have the same separation at all times in the crossing plane, but the PACMAN-bunches hit the total beam overlap earlier (middle) than the bunches in the core (right) in the separation plane (bottom).

5 Conclusion

Beam-beam observations at LHC are presented for the first time in this thesis. Data from dedicated machine study periods as well as data from normal luminosity runs have been analysed focusing on head-on or long-range interaction effects.

An important effect of the head-on interactions is the introduced tune shift. In dedicated experiments with a few bunches and by absence of long-range encounters the maximum coherent beam-beam parameter achievable was probed at injection energy. Linear tune shifts almost 5 times higher as the expected value under nominal conditions were obtained without obvious emittance growth and lifetime problems. Whereas, bunch intensities as high as $2{\times}10^{11}$ protons and small emittances of $1.2\,\mu$m rad were reached.

Unfortunately, this could only be calculated from the measured beam sizes and intensities. A direct tune measurement was not available. Due to the transverse damper the BBQ data was unusable at the important moment the beams were brought into collisions. Moreover, the Schottky monitors are still under commissioning and were as well not able to provide adequate data.

Nevertheless, the stability of the beam at the achieved high brightnesses and the calculations show the success of the experiment: no head-on beam-beam limits could be found yet. The experiment will be repeated at top energy (3.5 TeV) in one of the next machine development periods to probe the operational conditions of the machine and investigate if this has any influence on the results.

Orbit effects due to beam-beam interactions could clearly be measured. In a dedicated experiment it was possible to measure the long-range beam-beam kick with single colliding bunches during a separation scan. The shape of this measurement nicely follows the expectation, though, a small gap between the data and the prediction is present, which could not be explained yet. Further investigations and a second measurement are necessary to understand the discrepancy. However, this was the first time such a study was done at LHC and the agreement is already good.

Coming from optimized and dedicated experiments, where the theory is tested, to real operational conditions, the expected bunch-by-bunch differences due to the different collision patterns between bunches are seen. The long-range effect was demonstrated in both planes of IP1 with the aid of two different measurement methods (luminous region reconstruction and luminosity scan), since each method is only able to resolve one plane. The LHC BPM system, as it measures the two beams separately in each plane, could not be used for the analysis, because the effects are to small to be resolved by the devices.

The differences for the so-called PACMAN-bunches were investigated and they are in qualitative agreement with the simulations performed for the nominal injection scheme. Since the analysed data was taken at 3.5 TeV, with a bunch spacing of 50 ns and non-nominal beam parameters they do not fully agree quantitatively. New simulations are foreseen with the actual filling pattern and parameters to confirm the amount of the effect, as well. Moreover, the analysis must be repeated for IP5 to verify the same behaviour, as expected.

All in all, it can be concluded from the observations that perturbations of the beams from beam-beam interactions are clearly present and observable, but machine operation in the presence of them is still possible and no limits could be found yet. Therefore, beam-beam effects should allow to operate at nominal luminosity at 7 TeV.

6 Acknowledgement

This thesis would not have been possible without the guidance and the help of several individuals who in one way or another contributed and extended their valuable assistance in the preparation and completion of this study.

First I would like to express my gratitude to my thesis advisor Prof. Dr. Achim Stahl, for the possibility of writing this thesis. I am thankful for the revealing discussions and for the freedom he gave me during the whole process of preparing this work.

I am heartily thankful to my supervisor, Dr. Reyes Alemany Fernandez, whose encouragement, supervision and support from the preliminary to the concluding level enabled me to develop an understanding of the subject.

It is a pleasure to thank Dr. Bernhard Holzer for his support in the decision of the topic and especially for the many coffee talks we had to solve problems of all kind, they were always very interesting and helpful.

I would like to thank the LHC Operations Group and the Beam-Beam Working Group for their support during the machine development studies. Moreover, I am indebted to Dr. Werner Herr, Dr. Tatiana Pieloni, Dr. Jorg Wenniger, Dr. Mathilde Favier, Dr. Rhodri Jones, Dr. Eva Calvo, Dipl.-Phys. Tobias Bär and Dipl.-Phys. Gabriel Müller for their fruitful discussions during the analysis of the data.

I would also like to acknowledge the ATLAS Collaboration for providing the beam spot information from their data. In particular I am grateful to Dr. Rainer Bartoldus, Dr. Josh Cogan, Dr. Carl Gwilliam, Dr. Emanuel Strauss and Dr. Christoph Rembser for their help.

Many thanks to all of you, it was a nice time and a great experience to work with you.

Bibliography

[1] W. Herr, *Beam-Beam Effects,* Cockcroft Institute Lectures (2009), http://zwe.home.cern.ch/zwe/talks/cockcroft_beambeam.pdf.

[2] W. Herr, *Beam-Beam Interactions,* CAS - CERN Accelerator School: Intermediate Course on Accelerator Physics, Zeuthen, Germany (2003).

[3] T. Pieloni, *A Study of Beam-Beam Effects in Hadron Colliders with a Large Number of Bunches,* Thèse no 4211 (2008).

[4] W. Herr and B. Muratori, *Concept of luminosity,* CAS - CERN Accelerator School: Intermediate Course on Accelerator Physics, Zeuthen, Germany, pp. 361-378, (2003).

[5] J. D. Jackson, *Classical Electrodynamics,* John Wiley & Sons, ISBN 978-0471309321.

[6] W. Herr, *Features and implications of different LHC crossing schemes,* LHC Project Report 628, Geneva, Switzerland, 2003

[7] R. Bailey, P. Collier, *Standard Filling Schemes for Various LHC Operation Modes (Revised),* LHC-Project Note 323_Revised (2003).

[8] *LHC Design Report Volume I - The LHC main ring,* CERN, Geneva, CERN-2004-003-V-1.

[9] *LHC Design Report Volume II - The LHC Infrastructure and General Services,* CERN, Geneva, CERN-2004-003-V-2.

[10] *LHC Design Report Volume III - The LHC Injector Chain,* CERN, Geneva, CERN-2004-003-V-3.

[11] *CERN faq - LHC the guide,* CERN-Brochure-2009-003-Eng.

[12] *www.cern.ch.*

[13] K. Wille, *The Physics of Particle Accelerators - an introduction* Oxford University Press, ISBN 0-19-850549-3.

[14] *http://www.americanmagnetics.com/charactr.php.*

[15] P. Forck, *Lecture Notes on Beam Instrumenteation and Diagnostics,* JUAS 2011, www-bd.gsi.de/conf/juas/juas.html.

[16] D. Cocq, *The wide band normaliser - a new circuit to measure transverse bunch position in accelerators and colliders,* Nuclear Instruments and Methods in Physics Research A 416 (1998) p.1-8.

[17] O.R. Jones, *Commissioning and First Performance of the LHC Beam Instrumentation,* CERN, Geneva, Switzerland (2010), CERN-BE-2010-007 BI.

[18] E. Calvo et al., *The LHC Orbit and Trajectory System,* Proceedings DIPAC 2003, Mainz, Germany, CERN-AB-2003-057 BDI.

[19] Particle Data Group, *Particle Data Booklet,* http://pdg.lbl.gov/, 2010.

[20] Ch. Steinbach, *Wire Scanner,* Collaboration website for the edition of the report on 50 years of the Proton Synchrotron, https://project-ps50.web.cern.ch/project-PS50/.

[21] CAS - CERN Accelerator School, *Beam Diagnostics,* Dourdan, France (2008), CERN-2009-005.

[22] R. Jung, P. Komorowski, L. Ponce, D. Tommasini, *The LHC 450 GeV to 7 TeV Synchrotron Radiation Profile Monitor using a Superconducting Undulator,* CERN-SL-2002-015 BI.

[23] A. S. Fisher et al., *First Beam Measurements with the LHC Synchrotron Light Monitor,* CERN-BE-2010-019 BI.

[24] A. Jeff et al., *Spatial and Temporal Beam Profiles for the LHC using Synchrotron Light,* Proc. of SPIE Vol. 7726, 77261J.

[25] F. Roncarolo, *Can we get a reliable on-line measurement of the transverse beam size?,* LHC Evian Workshop (2010).

[26] L. Ponce, R. Jung and F. Méot, *LHC Proton Beam Diagnostics using Synchrotron Radiation,* CERN-2004-007.

[27] *http://emetral.web.cern.ch/emetral/ICEsection/2011-02-09/Presentation1.pdf.*

[28] F. Caspers et al., *The 4.8 GHz LHC Schottky Pick-Up System,* Proceedings of PAC07, Albuquerque, New Mexico, USA, FRPMN068.

[29] *http://ab-dep-bi-pm.web.cern.ch/ab-dep-bi-pm/?n=Activities.BRAN.*

[30] R. Alemany, M. Lamont, S. M. White, *Separation Scan Application Requirements,* LHC Project Document, Geneva, Switzerland (2008), LHC-OP-ES-0010.

[31] W. Herr et al., *Head-On beam-beam tune shift with high brightness beams in the LHC,* CERN-ATS-Note-2011-029 MD, 2011.

[32] W. Herr et al., *Head-on beam-beam collisions with high intensities and long range beam-beam studies in the LHC,* CERN-ATS-Note-2011-058 MD, 2011.

[33] A. S. Fisher, *Expected Performance of the LHC Synchrotron-Light Telescope (BSRT) and Abort-Gap Monitor (BSRA),* LHC Performance Note-014, 2009.

[34] http://wwwslap.cern.ch/mad/.

[35] R. Garoby, *Multiple splitting in the PS: results and alternative filling schemes,* Proc. LHC workshop, CHARMONIX XI, Charmonix 2001, CERN-SL-2001-003 (DI).